Nanostructures for investigating gap plasmon and sensing change in refractive index

by

Asif Imran Khan Choudhury
B.Sc., Bangladesh University of Engineering and Technology, 2004

A Thesis Submitted in Partial Fulfillment of the
Requirements for the Degree of

MASTER OF APPLIED SCIENCE

in the Department of Electrical and Computer Engineering

Nanostructures for investigating gap plasmon and sensing change in refractive index

by

Asif Imran Khan Choudhury
B.Sc., Bangladesh University of Engineering and Technology, 2004

Supervisory Committee

Dr. Reuven Gordon, Department of Electrical and Computer Engineering
(Supervisor)

Dr. Tao Lu, Department of Electrical and Computer Engineering
(Departmental Member)

Dr. Alex Brolo, Department of Chemistry
(Outside Member)

Supervisory Committee

Dr. Reuven Gordon, Department of Electrical and Computer Engineering
(Supervisor)

Dr. Tao Lu, Department of Electrical and Computer Engineering
(Departmental Member)

Dr. Alex Brolo, Department of Chemistry
(Outside Member)

ABSTRACT

I have investigated gap plasmon mode of an eccentric coaxial waveguide structure using effective index method. The results found good agreement with fully-vectorial numerical calculation. In the eccentric structure, a strong field localization has been noticed at and around the smallest gap. Analysis showed the increase of effective index of lowest-order waveguide mode to 3.7 in the structure considered with a 2 nm minimum gap for a wavelength of 4 μm. In the visible regime, the effective index increases to over 10 for the same structure.

Nanohole arrays, both flowover and flow-through formats, have been fabricated using focused ion beam (FIB). A 2-color LED-based nanohole sensor has been presented. The objective of the sensing platform was to register mutually opposite intensity change of transmitted light when the dielectric medium of metal-dielectric interface of the nanohole sensor undergoes a change. A number of tests with microfluidics setup demonstrated the proof-of-concept.

Contents

List of Figures

Acknowledgments

I like to sincerely thank my supervisor, Dr. Reuven Gordon, for his unwavering support and guidance throughout the length of my endeavor.

I would also like to convey my appreciation to Dr. David Sinton and Dr. Alex Brolo, for their valuable suggestions and giving me the opportunity to work in the LOC-Nano group.

Thanks to my friends and colleagues in University of Victoria for all the lively conversations and support.

Finally, without continual encouragement of my father and relentless support of my wife, this work would not be possible. Mother, no matter wherever you are in the heaven, I know you are smiling.

Dedication

To my family

Chapter 1

Introduction

Nanotechnology is the branch of science which deals with the control of behavior of matters **in the scale of several atoms**. In general, the response of a structure having size between 1 to 100 nanometer, that is on the order of one-billionth of a meter in at least one dimension falls in the purview of nanotechnology. If a material is built with such a small dimension, its behavior changes significantly compared to its bulk counterpart, which, if harnessed properly, has the potential to revolutionize many aspects of current technology. The field of nanotechnology is extremely vast and currently witnessing an unprecedented multidisciplinary research collaboration worldwide.

The study of plasmonics involves primarily the interaction between light and metals which focuses on how electromagnetic wave in the visible and near-infrared regime can be guided, enhanced and manipulated in the minuscule structure. When the oscillation of mobile electrons at the surface of a metal in the metal-dielectric interface match that of an interacting electromagnetic field, a wave of hybrid excitation is created called surface plasmon (SP). This propagating density wave have identical frequency of but shorter wavelength than the incident electromagnetic wave. Surface plasmon has a number of unique characteristics, which made it a topic of extensive research in last two decades. For example, due to its propagating nature and proximity to surface, SP has the potential to carry information from one part of a microprocessor to another. This kind of plasmonic interconnections has the promise to increase transistor speed manifold. Again SP's non-radiative nature greatly facilitate field enhancement and localization which find immense application in nonlinear optical processes like second harmonic generation (SHG), optical trapping and surface-enhanced Raman scattering (SERS).

Top-down method of nanofabrication like focused ion beam (FIB) can be used to create array of symmetric and asymmetric nanostructures. Surface plasmon mediated transmission through metallic array of subwavelength holes, known as extraordinary optical transmission (EOT), can be used to sense change in the refractive index in the metal-dielectric interface. This makes the array a sensing element which can be used to detect chemical and biological substances.

The present research work mainly focuses on two areas. One objective is to propose an asymmetric nanostructure which effectively localizes and enhances electric field. Such a structure has been analyzed theoretically and fabricated using FIB. Transmission measurements using the nanostructure will accompany to characterize it. The next goal is to introduce a sensing platform to register change in the refractive index of the dielectric medium in the metal-dielectric interface using array of subwavelength holes and appropriate choice of dual-wavelength LED. Details of fabricating nanohole arrays using FIB will also be provided.

1.1 Organization of the thesis

Chapter 2 provides a brief account of the physics behind surface plasmons, localized surface plasmons and surface plasmon mediated enhanced light transmission through nanohole arrays. This chapter also provides a comparative study between reflection mode geometry and transmission mode geometry in context of using EOT for sensing purpose.

Chapter 3 analyzes gap plasmon mode in the eccentric structure which uses effective index approximation. It will be shown analytically that the localized field enhancement in the smallest gap can be attributed to the increase in the effective index of the lowest order waveguide mode. The computed value of effective index will be compared with that of a commercially available finite difference mode (FDMS) solver. The analysis will be extended for extremely small gap using a finite element method (FEM) solver.

Chapter 4 gives a description of milling subwavelength arrays using FIB. Various milling parameters of both flowover and flow through arrays, issues faced during fabrication and results of fabrication will be discussed in detail.

Chapter 5 describes the development of a nanohole sensor using bi-color LED for registering change in refractive index of dielectric material of a metal-dielectric interface. Various parts of the sensor are described with operating procedure. Test

results supports the concept on which the sensor is built. Evaluation of test results and various issues with the system will be discussed.

Chapter 6 gives an account of measurements done with fabricated eccentric coaxial structure. A Number of test results showing the influence of asymmetry in nanostructure will be discussed in detail.

Chapter 7 summarizes the work done and outlines the future initiatives that can be undertaken.

Chapter 2

Literature Review

2.1 Introduction

This chapter provides a brief overview of two fundamental excitation of plasmonics - surface plasmons (SP) and localized surface plasmons (LSP). The chapter also discusses how nanostructures can be used to harness them. SP and LSP are generated when conduction electrons of metal in a metal-dielectric interface couple suitably with electromagnetic waves, with a central difference that SP are propagating and LSP are non-propagating in nature. A type of strongly localized plasmons arising in the narrow metallic gaps filled with dielectric, known as gap plasmons, will be analyzed in relation to a proposed asymmetric nanostructure in the next chapter.

My research work involves an investigation of aforementioned gap plasmon mode in an eccentric coaxial structure and to implement surface plasmon mediated transmission, known as extraordinary optical transmission (EOT), to build a sensing platform. The following sections will review past literature on propagating and non-propagating surface plasmons, their role in enhanced transmission through array of nanostructures, the influence of geometrical variations of nanostructures on EOT and finally integrating them in a sensing environment.

2.1.1 Surface plasmons

Surface plasmons are the collective oscillations of electrons in response to electromagnetic excitations at the interface between vacuum or a material with positive dielectric constant (like air) and a negative dielectric constant (like metal). This electromagnetic surface wave arises via the coupling of the electromagnetic fields to

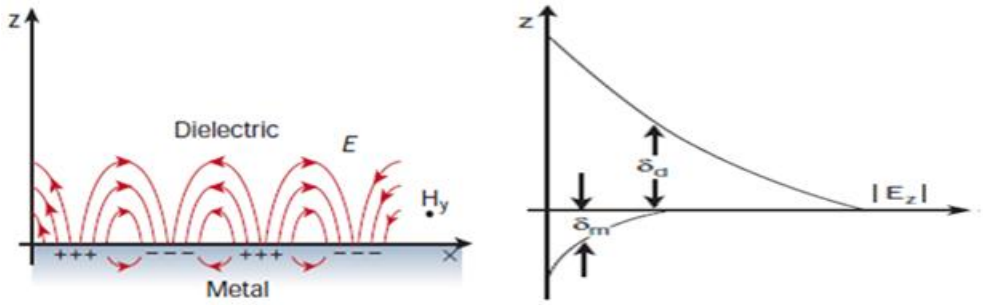

Figure 2.1: (a) Schematic representation of SPP as charge oscillations at the interface between a metal and a dielectric. (b) The exponential dependence of the electromagnetic field intensity on the distance away from the interface reflects its waveguide mode nature which propagates along the interface [7].

oscillations of conductor's electron plasma which propagate along the metal-dielectric interface and decays exponentially in the perpendicular direction on both sides of the interface.

Alternatively, SP can be viewed as a propagating transverse magnetic wave (having no components of magnetic field in the direction of propagation), which requires only one interface to exist. Figure 2.1(a) shows the TM nature of the SP (magnetic field in the y-direction). Figure 2.1(b) shows the evanescent electric field of SP which underscores it bound, non-radiative nature. The decay length of the field in the dielectric (like glass or air), δ_d, is of the order of the half the wavelength of the wavelength involved. Surface plasmons propagating in the x-direction at metal-dielectric interface (Figure 2.1) can be described in terms of electric field by the following wave equation:

$$\nabla^2 \vec{E}_{d,m} = \mu_0 \mu_{d,m} \epsilon_0 \epsilon_{d,m} \frac{\partial^2 \vec{E}_{d,m}}{\partial t^2} \tag{2.1}$$

where $\vec{E}_{d,m}, \mu_0, \mu_{d,m}, \epsilon_0$ and $\epsilon_{d,m}$ are electric field of SP in the metal-dielectric interface, permeability of space, permeability of metal-dielectric interface, permittivity of the space and permittivity of metal-dielectric interface, respectively. The solution of the equation are as follows:

$$\vec{E}_d(x, z, t) = \vec{E}_{d,0} e^{i(k_x x + k_z z - \omega t)} \tag{2.2}$$

$$\vec{E}_m(x, z, t) = \vec{E}_{m,0} e^{i(k_x x - k_z z - \omega t)} \tag{2.3}$$

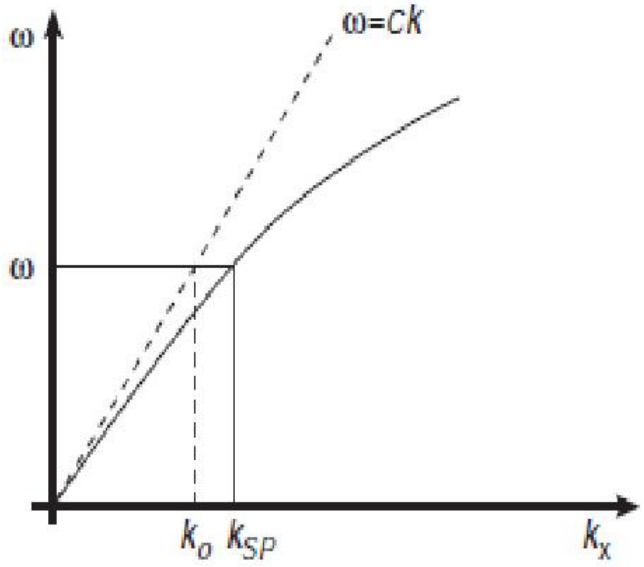

Figure 2.2: Dispersion curve of SP (solid line) lies to the right of light line (dashed line) [7]. At any given frequency ω, SP has greater momentum ($\hbar k_{SP}$) than a photon in the dielectric ($\hbar k$).

where equation 2.2 and 2.3 describes electric field distribution of SP in dielectric and metal parts of the interface, respectively. k_x and k_z are wave function of the SP in x- and z-direction, respectively. They are given as follows:

$$k_x = \frac{\omega}{c}\sqrt{\frac{\epsilon_m \epsilon_d}{\epsilon_m + \epsilon_d}} \tag{2.4}$$

$$k_z = \frac{\omega}{c}\sqrt{\frac{\epsilon_m^2}{\epsilon_m + \epsilon_d}} \tag{2.5}$$

where $\omega, c, \epsilon_m, \epsilon_d$ are the angular frequency of light, speed of light in vacuum, frequency dependent complex relative permittivity of the metal and dielectric constant of the dielectric medium, respectively. To sustain SP in the metal-dielectric interface it is needed to have $\mathrm{Re}[\epsilon_m] < \mathrm{Re}[\epsilon_d]$. It can be seen from equation 2.5 that k_z is imaginary. Equation 2.4 shows that k_x, the wave vector of SP in the direction of propagation is real and greater than the wave vector of light ($k_0 = \omega/c$) in the dielectric. This fact is revealed in the dispersion curve of SP (Figure 2.2) which always lies to the right of the light line of the dielectric. Hence special momentum matching technique needs to be adopted to couple light and SP together.

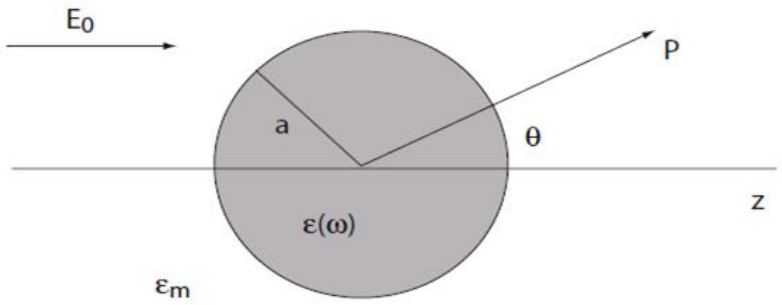

Figure 2.3: Quasi-static approximation, where $d << \lambda$. The external field appears as static to the particle [52].

2.2 Localized surface plasmons

Localized surface plasmons are the non-propagating excitations of the conduction electrons of metallic nanostructures coupled to the electromagnetic field. The interaction of a particle of size d with the electromagnetic field can be analyzed using the quasi-static approximation, where $d << \lambda$, i.e. the particle is much smaller than the wavelength of light in the surrounding medium (Figure 2.3). In this case, we can ignore the time-dependent part of the Maxwell's equations, so the case of the field distribution reduces to that of an electrostatic case. For example, if a metal sphere is situated in a dielectric medium:

$$E_{in} = \frac{3\epsilon_m E_0}{\epsilon + 2\epsilon_m} \tag{2.6}$$

where E_0 is assumed to be the field outside the particle, which is, in this case, an electrostatic field. If we ignore the imaginary part of the relative permittivity of metallic particle in the above equation then it is obvious that the field inside the metal particle undergoes resonant enhancement when Re[ϵ]=-2ϵ_m [37]. At the boundary, this condition increases the electric field intensity which is again dictated by imaginary part of the relative permittivity of the metal, ϵ. Inspection of the equation will reveal the fact that the resonance is independent of the particle's dimension. The size of the particle also influences the resonance, for example, the above mentioned approximation does not hold for large particles. If we bring such small particles in close proximity, the summation of local field enhancement from individual particle can be huge. Electric field enhancement of over $1,000$ have been reported for identical-sized spherical particles in a row [51].

2.3 Gap plasmon mode

In multilayer structure (metal-insulator-metal or insulator-metal-insulator) each single interface can sustain SP and interactions between them give rise to coupled mode. This coupled plasmon excitations in the gap can propagate like a waveguide mode in the structure which not only enhances the local field but also has the potential to be used in the nanometric circuits. The strength of coupling depends on the separation between adjacent interfaces; smaller the gap, stronger the coupling (Figure 2.4).

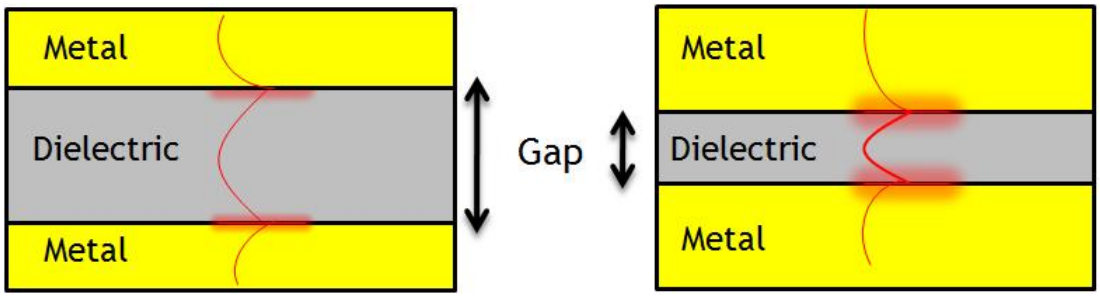

Figure 2.4: The strength of the coupling between SP in the adjacent layers depend on the gap between interfaces.

Figure 2.5 shows the dispersion relation of the lowest order waveguide mode at the silver/air/silver multilayer system. The propagation constant, β, does not go to infinity as the SP frequency is approached, but reverses it direction and eventually crosses the light line, as for SP propagating at single metal-dielectric interface. It is evident that, if the dielectric layer is thin enough, large value of β (hence high value of effective index, $n_{eff} = \beta/k_0$) can be achieved. This means that the group velocity of gap plasmon modes will slow down. Localization of the field is physically the result of the gap mode having an increase in local index. In addition, since higher value of β is achievable for gap plasmon mode at an excitation well below surface plasmon frequency,ω_{SP}, excitation in the infrared region can be used to generate such gap plasmon mode. The surface plasmon is related to plasma frequency, ω_P, by the following relation:

$$\omega_{SP} = \frac{\omega_P}{\sqrt{2+\epsilon_d}} \tag{2.7}$$

where ϵ_d is the dielectric constant of the dielectric medium.

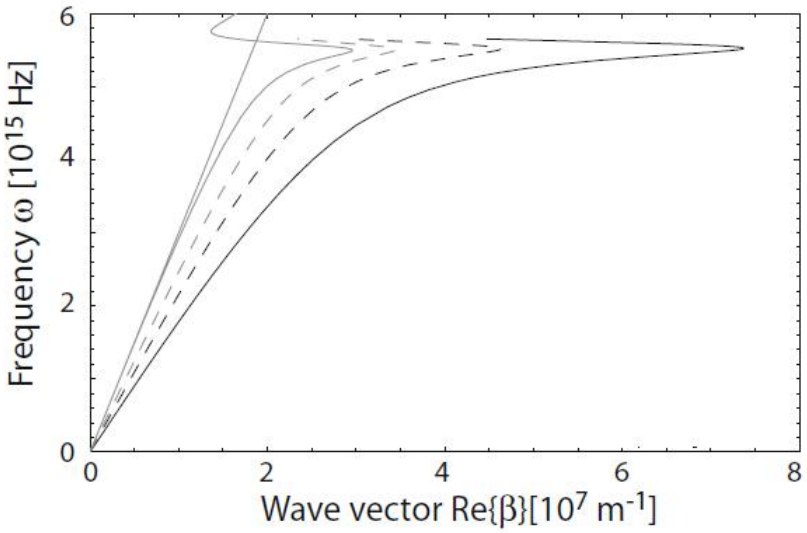

Figure 2.5: Dispersion relation of the lowest order gap plasmon mode of a silver/air/silver multilayer geometry for an air core of size 100 nm (broken gray curve), 50 nm (broken black curve), and 25 nm (continuous black curve). Also shown is the dispersion of a SP at a single silver/air interface (gray curve) and the light line (gray line)[52].

2.4 Extraordinary optical transmission

To analyze the influence of SP on the transmission process, the regime of subwavelength apertures is of much interest. A subwavelength hole is one whose dimensions are smaller than half the wavelength of the incident light. Assuming that the incident light intensity I_0 is constant over the area of the aperture, Bethe arrived at an exact analytical solution for light transmission through a sub-wavelength circular hole in a perfectly conducting, infinitely thin screen [8]. The transmission coefficient for a plane wave for normal incidence is then given by:

$$T = \frac{64}{27\pi^2}(kr)^4 \propto (\frac{r}{\lambda_0})^4 \tag{2.8}$$

where r is the radius of the hole and λ_0 is the wavelength of the incident light. Therefore, it was widely accepted since then that almost no light would emerge from the other side of the the hole. However, it must be emphasized that, Bethe's original theory was for a single small hole in an infinitely thin metal treated as a perfect electric conductor. It was not applicable for metallic nanohole arrays or for hole

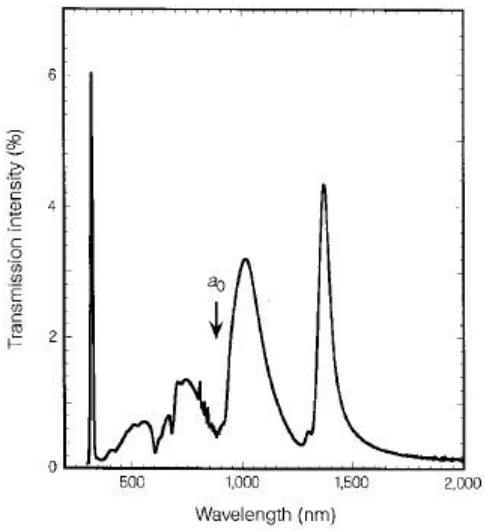

Figure 2.6: Transmission spectrum from the nanohole array in a silver film. The film thickness, hole diameter and periodicity are 200 nm, 150 nm and 900 nm, respectively [22]. The periodicity of the array is indicated as a_0.

size comparable to the wavelength. For subwavelength holes in real metal for finite thickness we must take into consideration the propagation or decay of waveguide modes that leads to resonance.

In 1998 Ebbesen and co-workers reported on the extraordinary optical transmission (EOT) through metallic nanohole arrays of various metals. The subwavelength holes were made by focused-ion beam milling. The transmission was extraordinary in that absolute transmission efficiencies at peak wavelengths were significantly higher than the light that impinged on the holes, and orders of magnitude higher than predicted by earlier theory. Figure 2.6 shows the zero-order transmission spectrum obtained by Ebbesen's group from a square array of cylindrical holes in a silver film with quartz substrate. The peak at 326 nm comes from bulk silver plasmons, the wavelength at which silver is transparent, which disappears as the film thickness increases. The maximum in transmission is seen at a wavelength that corresponds to the periodicity of the array and was shown to vary correspondingly for different periodicities. The minima are a result of Wood's anomalies that arise when a diffracted order, tangent to the grating plane is absent in the transmission spectrum at specific wavelength [30].

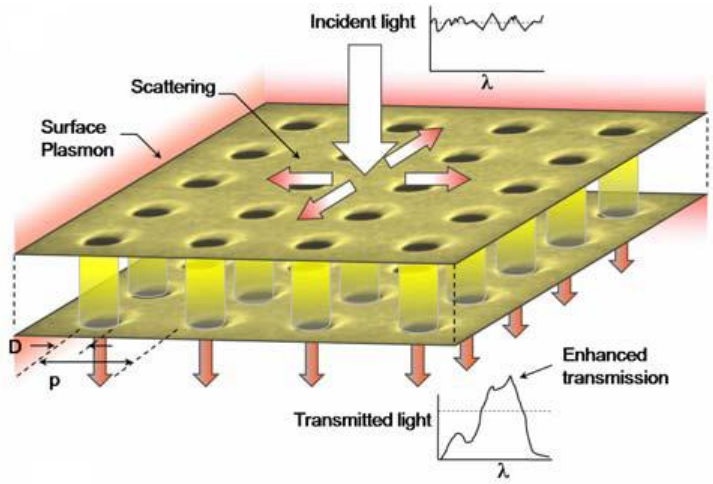

Figure 2.7: A conceptual diagram showing how incident light scatters into SP in a metallic nanohole array and enhanced transmission takes place at select wavelength [64].

The observation of EOT in the visible and near-infrared regime, by Ebbesen and co-workers, was suggested to arise from coupling to propagating surface plasmons [22, 30] or surface plasmon polariton (SPP). The Bragg condition for resonance of the SP with the periodicity of a rectangular array is given by:

$$k_{SP} = 2\pi\sqrt{\frac{i^2}{a^2} + \frac{j^2}{b^2}} \tag{2.9}$$

where a,b are the x and y direction periodicities of the array and i, j are the whole number resonance orders along the x and y directions, respectively [33]. The resonant transmission occurs close to the Bragg resonance for SP. Figure 2.7 is a conceptual diagram which shows how the incident light scatters into SP on the surface of metallic nanohole array, penetrate the hole and scatters again on the other side of the hole. The extent of SP generation and the degree of transmission, depend on number of factors like the wavelength of incident light, geometry of nanostructure and relative permittivity of the metal.

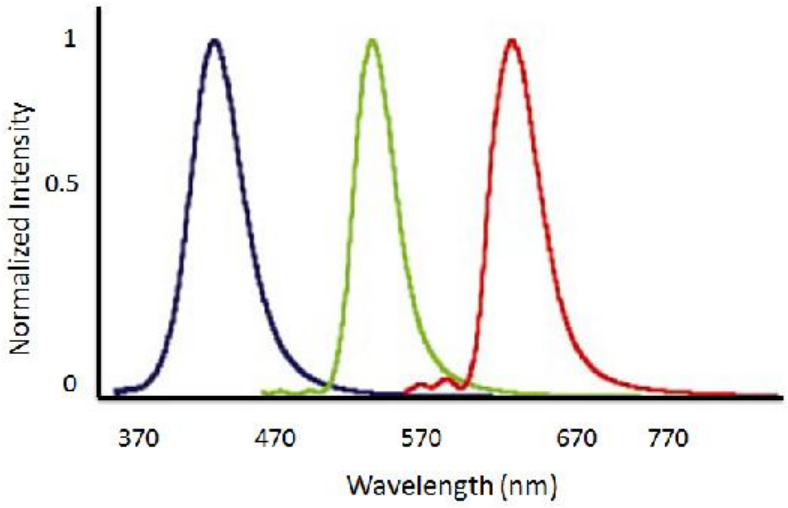

Figure 2.8: Periodicity of square nanohole array can be used to tune the position of lowest order peak $(i, j = 0, 1)$ [7].

2.5 SP and the geometry of nanostructure

2.5.1 Periodicity

The position of the resonant peak in the transmission spectrum can be tuned by adjusting the periodicity of the nanohalo array. For a square array of a_0, the peak λ_{max} in the transmission spectrum for normal incidence can be derived from the dispersion relation, Equation 2.4, which is:

$$\lambda_{max} = \frac{a_0}{\sqrt{i^2 + j^2}} \sqrt{\frac{\epsilon_d \epsilon_m}{\epsilon_d + \epsilon_m}} \tag{2.10}$$

where i, j are the whole number resonance orders along the x and y directions, respectively. Figure 2.8 demonstrates the idea of tuning the position of resonant peak by varying the periodicity. For periods 300, 450 and 550 nm and hole diameters 155, 180 and 225 nm, respectively, the position of the lowest order peak $(i, j = 0, 1)$ were noticed at 436, 538 and 627 nm, respectively. The square nanohole arrays were made in a free standing 300 nm thick silver film.

2.5.2 Film thickness

As the film thickness is increased, the hole becomes a tunnel and the coupling between surface waves on the two sides of the film gets changed. For thick films, it weakens exponentially. The influence of film thickness on the transmission process was studied experimentally for optically thick silver films in the near-infrared regime [20]. For thick films, the transmission resonance was reduced exponentially with film thickness. This was attributed to the exponential decay of the waveguide mode within the hole. It was postulated from those observations that the SP on either side of the film are strongly coupled for film thicknesses less than 200 nm, and become less strongly coupled as the film thickness is increased. Theoretically, the lowest order waveguide mode excited inside the hole, dominates the transmission process for thicker films which was supported by extensive numerical analysis [57]. Propagating modes inside the hole, or even for modes close to cutoff, give Fabry-Perot resonances since there is reflection from impedance and mode-shape mismatch at the ends of the hole. When the reflections between the ends of the hole add up in-phase, the field is enhanced within the hole and increased transmission is observed.

2.5.3 Hole shape

Change in the hole shape influences number of properties of the nanostructure, for example, waveguiding properties of the hole and scattering of the modes on either side of the hole. Even for infinitely thin perfect electric conductors, the magnetic polarizability and electric polarizability of the aperture are influenced by the shape of the aperture. Various hole shapes and change in dimension along the length of the holes have been investigated extensively to study how these dimensional changes affect manipulation of light inside the structure.

For a perfect electric conductor, the lowest-order mode of the coaxial structure does not have any cut-off wavelength. Due to rotational symmetry, a normally incident plane wave does not couple to that mode, hence it does not play a role in the transmission. For real metals, the cutoff of the TE_{11}-like gap-mode is governed by the material response and the gap. This has been referred to as cylindrical surface plasmon (CSP) mode [4, 38, 56]. Experimental works have been conducted on coaxial arrays in the visible [62] and infrared regime [25, 24]. In the infrared regime, coaxial array structures showed both an increase in the peak transmission and a shift of the

peak to longer wavelengths compared to the hole array. Enhanced (5×) mid-infrared (4 μm)transmission through these sub-wavelength coaxial arrays has been observed over the same fractional opening area of the hole arrays [24]. By varying the dimensions of the coaxial geometry, the position of the resonant peak can be tuned. As hinted earlier, this enhanced transmission and red shift of the resonant peak have been attributed to coupling between the coaxial TE_{11} mode and CSP of the metal.

Asymmetric hole shapes like rectangular and elliptical holes show strong polarization dependence[32, 44, 67, 68, 63, 59]. Aspect ratio strongly influences transmission of rectangular holes; in a perfect electric conductor the cut-off wavelength of the lowest order mode is half the longest side. An increase of almost an order of magnitude in the normalized transmission through optically thick Au films is found when the hole shape is changed from circular to rectangular holes, despite the fact that the surface area of the holes decreases. For the elliptical holes the degree of polarization is determined by the ellipticity and orientation of holes.

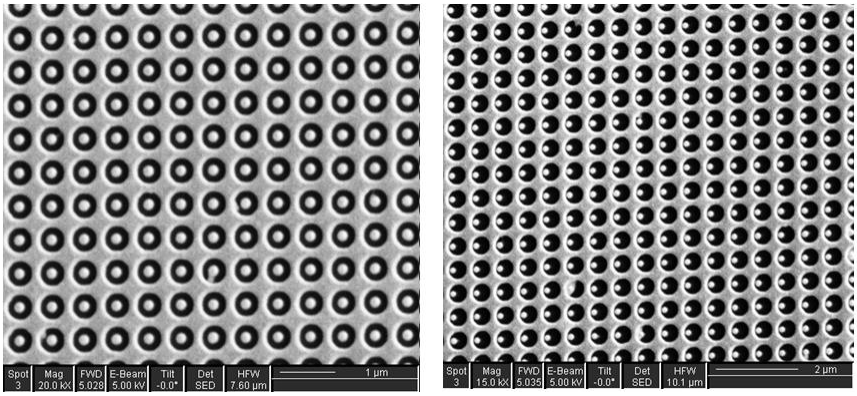

Figure 2.9: SEM pictures of symmetric (left) and asymmetric (right) structure.

If we break the symmetry of the coaxial structure and shift the island close to circumference of the outer circle, we notice a strong field localization at and around the narrowest gap [34]. In the eccentric structure the effective index of the lowest order waveguide mode increases considerably, for example, to 3.7 when the narrowest gap is 2 nm. This means, at the vicinity of the smallest gap, group velocity of the lowest order waveguide mode slows down significantly increasing the electric field intensity. If the loss in the metal is negligible then a strong build-up of energy has been noticed in the vicinity of the smallest gap. In the visible regime, the effective index increases to over 10 for the same structure. As revealed by my calculation using

effective index method, the field localization can be attributed to the gap plasmon mode having an increase in the local index. Future applications utilizing the strong field localization of the eccentric structure can be: non-linear optics, surface enhanced Raman scattering (SERS) and optical trapping.

2.6 Nanohole array as a sensor element

Earlier works on transmission gratings showed the dependence of the resonance wavelength on the refractive index of the dielectric medium of metal-dielectric interface [13]. For metallic nanohole array, the shift of the position of resonance wavelength was first shown for liquid dielectric interface [46]. In that work, the transmission resonance wavelength of SP was shown to undergo redshift as the refractive index of the liquid dielectric medium increased. This specific dependence of EOT on the change of refractive index of the dielectric environment make the nanohole array particularly suitable as a sensor element for the detection of surface-binding events [29]. SPR-based biosensing is conducted by immobilizing a target and monitoring the changes in the resonance upon adsorption of the molecule of interest to the target.

Figure 2.10 shows the relationship of the SPR from the metallic nanohole array of the gold film with the surface adsorption events. At first, the white light transmission through bare gold and air as the dielectric, registered the SPR peak at 645 nm. Then the surface of the array was adsorbed by a monolayer of mercaptoundecanoic acid (MUA). This modification showed a 5 nm redshift in the position of SPR peak. A further adsorption of protein (bovine serum albumin - BSA) on top of the MUA layer provided an additional 4 nm redshift in the SPR peak. After the removal of surface species by a plasma cleaning treatment restored the spectral characteristic of a bare gold surface [10]. The sensitivity obtained from this experiment was 400 nm/RIU (RIU = refractive index unit).

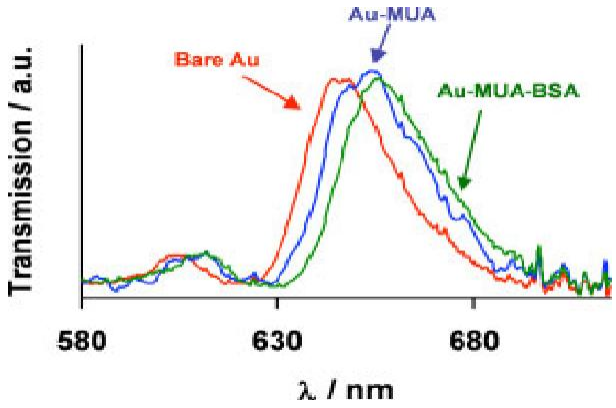

Figure 2.10: Redshift of the SPR peak with the adsorption of monolayer of MUA and BSA protein on the top of MUA [10].

Traditionally SPR-based sensing platform used reflection-mode geometry which employed prism coupling and total internal reflection of incident light proposed by Kretschmann and Raether [45]. A typical sensitivity of prism coupled SPR systems is in the range between 3100 to 8000 nm/RIU [42]. Despite of this higher sensitivity transmission-mode geometry is preferred for several reasons over reflection-mode geometry from the perspective of integrating the sensor in lab-on-chip environment. For example:

- Transmission-mode geometry works at normal incidence, it simplifies alignment and device level miniaturization to a great extent.
- Reflection-mode geometry introduces distortion to the imaging.
- In transmission-mode geometry, the footprint required for a nanohole array is small compared to that required in reflection-mode geometry, which, makes this arrangement particularly suitable for multiplexing.

Beside wavelength-shift based detection process, change in intensity level of the transmitted monochromatic light can also indicate the event of adsorption [50]. The wavelength of the transmitted light must be in close proximity of chosen SPR peak. The steepest edge of the transmission band should provide the best sensitivity. A limitation of this approach is, spurious signals generated from other sources, like scattering by the particles in the solution, are inseparable from the intensity variation. To overcome the limitation, biaxial array with different resonance peaks for the two orthogonal polarizations were proposed [23]. After the surface of such a biaxial array

was modified by molecular adsorption, the shift in the SPR underwent an increase in transmission for one polarization while the other one decreased. The spurious signal variation can be eliminated by analyzing the adsorbate-induced changes in relative intensity from both polarizations.

To date, SPR based bio-chemical sensing only utilized dead-ended holes. Recent experiments showed that flow-through holes offer a host of advantages over its flowover counterparts in SPR-based sensing[3], like smaller foot-print, lower limits of detection, denser integration, multiplexing and collinear detection. The flow-through format enables rapid transport of reactants to the active surface inside the nanoholes, with potential for significantly improved time of analysis and biomarker yield through nanohole sieving. 6-fold improvement in response time has been reported achieved by using flow-through method over conventional flowover system.

2.7 Summary

This chapter started with a brief discussion on surface plasmons, localized surface plasmons and gap plasmon mode. Propagating surface plasmon has been described as a waveguide mode which requires only one interface to sustain. Enhancement of field due to LSP has been explained with quasi-static approximation for particles much smaller than the wavelength. Gap plasmon mode has been introduced as the result of coupling of SP at two adjacent interfaces whose coupling strength depend on gap width among other factors. One of the goal of this thesis is to analyze gap plasmon mode in eccentric coaxial structure. A theoretical investigation of this, is provided in chapter 3 while chapter 6 gives an account of early experimental work on the proposed structure.

EOT has been described as the consequence of SP in the following sections. SPR has been linked with Bragg condition for resonance. Then number of factors in nanohole geometry that influences SPR, have been discussed. How the periods of nanohole array can be used to tune the SPR has been shown with an ensuing discussion on the relation of film thickness and coupling of SP on either side of the metal film for real metal. Influence of hole shape on EOT and localized field enhancement, for both symmetric and asymmetric structure, have been discussed.

The last section of the chapter showed the application of nanohole array as a sensing element. The benefit of transmission-mode geometry over conventional Kretschmann geometry have been discussed in context of lab-on-chip application. Chapter 5 of this thesis is devoted to describe the development of such a transmission based sensor suitable to be used in lab-on-chip environment. Lastly, the use of flow-through holes, a relatively novel sensing element in the field of optofluidics compared to dead-ended hole, have been shown to combine the merits of nanoconfined transport with the SPR-based sensing.

Chapter 3

Investigation of gap plasmon mode in eccentric structure using effective index method

3.1 Introduction

In this chapter, gap plasmon mode will be investigated in relation to an asymmetric nanoscale structure. This structure is obtained by shifting the island of a coaxial structure from its center. The behavior of gap plasmon mode, in this proposed eccentric structure differs considerably from its coaxial counterpart which will be analyzed theoretically in the following sections.

Hole-shape affects the waveguiding properties subwavelength apertures. To ascertain the effect of hole-shape in the propagation and transmission of light a host of different shapes, both symmetric and asymmetric, have been studied previously which include: cylindrical [39], square and rectangular [39, 44, 12, 63, 67, 68, 31, 28, 27, 53, 75], cylindrical coaxial [60, 58, 4, 5, 6, 62, 25, 24] rectangular coaxial [55], rectangle-in- cylinder coaxial [69], eccentric-coaxial [72, 1, 17, 18, 74], elliptical [32, 15, 35, 19, 65, 54], cruciform [16, 61, 14, 71], C-, H-, and E-shaped [40, 49, 66], double-hole (overlapping [48, 47] and separated [35]), triangular [2, 43] and star-shaped [70] holes.

In the study of rectangular hole, it has been noticed that the cut-off wavelength increases dramatically as the height of the hole decreased [31, 27, 36], as has been observed experimentally [21]. This is due to the fact that when parallel edges of the

rectangular aperture were brought closer together, the coupling between SP modes on two adjacent interfaces became increasingly stronger which increased propagation constant as well as effective index of the gap plasmon mode [31]. Exactly the same way, the effective index of the waveguide modes of a cylindrical coaxial structure is dependent on width of the annular region [62, 58, 4]. In the eccentric structure, the width of this annular region is not constant but varies along the circumference of the island. Therefore, effective index of the waveguide modes increases significantly at and around the smallest gap which decreases their group velocity in that region. This, in turn, render to effectively enhance the field intensity in the vicinity of the smallest gap region.

Previously this type of structure has been studied for perfect electric conductor (PEC) using conformal mapping [72, 1, 17, 18, 74] and in those works it has been shown that the cut-off wavelength is offset-dependent. In my investigation I have concentrated on a different aspect of the structure: the influence of gap plasmon. I have used effective index approximation which has been adapted from the study of rectangular holes [31] to the cylindrical geometry. The structure analyzed is comparable to recent structures produced by interference lithography [25, 24], which has the great advantage of allowing for mass production. The analytical results of the effective index model agree well with comprehensive finite-difference mode-solver (FDMS) numerical calculations for a wavelength of 4 μm. In the visible and near-infrared region of the optical spectrum, the FDMS gives spurious results for increasingly smaller gaps; however, my effective index approximation has found good agreement with the result obtained from fully-vectorial finite element method (FEM) in that regime.

3.2 Effective index model eccentric coaxial gap plasmon

Past works on eccentric coaxial structures used conformal mapping to analyze the geometric influence on mode propagation for PECs. Here, the geometric influence is accounted for by the effective index variation from the gap plasmon, which is a good approximation for plasmonic materials when the effective index is determined predominantly by the gap variation. This approximation neglects conformal mapping effects that become important if the tangent angles to the inner and outer cylinders vary significantly the approximation is suitable for relatively large inner island sizes

or small offsets.

The effective index method is an approximation that assumes that separation of variables is allowed. I have considered first the radial dependence of the field to determine an effective index as a function of angle where each angle has a different gap, which contributes to the change in the effective index. These effective index calculations assume that there is no angular dependence, so that the equations of a concentric structure can be used. The next step is to use these values to compute angular dependence of the effective index. Therefore, the overall propagation constant of the mode can be determined from the one dimensional angular calculation.

Figure 3.1 illustrates the application of effective index method in eccentric coaxial structure. Figure 3.1(a) shows the structure under consideration where the metal is gold and dielectric is air. Figure 3.1(b) decomposes the figure in two coaxial structures with two extreme gap width. The left hand coaxial structure has a gap whose width is equal to the maximum gap and the right hand figure has a gap whose width is equal to the minimum gap in the in the eccentric structure of Figure 3.1(a). Figure 3.1(c) shows the equivalent coaxial structure with the exception that the gold has been replaced with perfect electric conductor (PEC) and air with the dielectric whose effective index has been calculated in the preceding step. Figure 3.1(d) combines the two in such a way that the dielectric is modified as a function of angle.

The Helmholtz equation for the axial electric field, $E_z(\theta)$, is used since this field component is present in the gap-plasmon and is continuous at the boundaries:

$$\frac{\partial^2 E_z}{\partial r^2} + \frac{1}{r}\frac{\partial E_z}{\partial r} + \frac{1}{r^2}\frac{\partial^2 E_z}{\partial \theta^2} + \frac{\partial^2 E_z}{\partial z^2} + \frac{\omega^2}{c^2}\epsilon_z E_z = 0 \tag{3.1}$$

where $\epsilon_z(r, \theta)$ is the relative permittivity of the dielectric material in the annular region, ω is the angular frequency and c is the speed of light in vacuum.

For the concentric cylindrical coaxial structure, where the gap is uniform around the circumference, the effective index of the mode is found by equating the tangential electric and magnetic fields at the boundary of island (radius a) and outer circle (radius b) to give the solution [73] :

$$AB - CD = 0$$

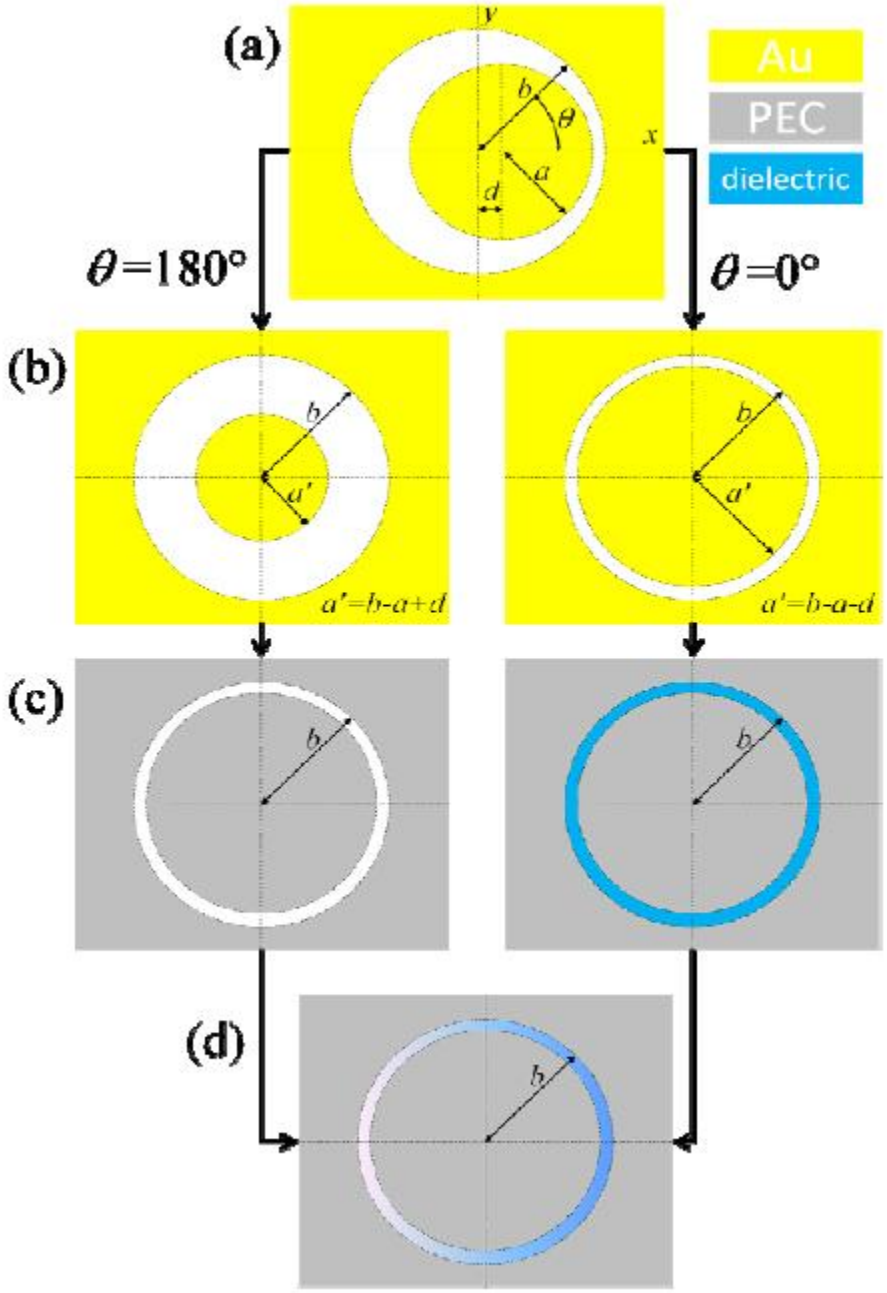

Figure 3.1: (a) Schematic of eccentric cylindrical coaxial waveguide in gold with air gap. (b) Equivalent structures to calculate radial contribution to effective index assuming at each angle that the structure is rotationally symmetric. (c) Effective index of the rotationally symmetric structure is equivalent to a dielectric inside a coaxial perfect electric conductor (PEC). (d) Angular dependence, using effective index values calculated from the radial dependence at each angle [34].

where

$$A = \frac{I_0(p_2 a)}{I_0(p_1 a)} - \frac{\epsilon_2 p_1 I_1(p_2 a)}{\epsilon_1 p_2 I_1(p_1 a)} \tag{3.2}$$

$$B = \frac{\epsilon_2 p_3 K_1(p_2 b)}{\epsilon_3 p_2 K_1(p_3 b)} - \frac{K_0(p_2 b)}{K_0(p_3 b)} \tag{3.3}$$

$$C = \frac{K_0(p_2 a)}{I_0(p_1 a)} - \frac{\epsilon_2 p_1 K_1(p_2 a)}{\epsilon_1 p_2 I_1(p_1 a)} \tag{3.4}$$

$$D = \frac{\epsilon_2 p_3 I_1(p_2 b)}{\epsilon_3 p_2 K_1(p_3 b)} - \frac{I_0(p_2 b)}{K_0(p_3 b)} \tag{3.5}$$

where I_0, K_0, I_1, K_1 are modified Bessel functions of order zero and one, $\epsilon_z(r < a') = \epsilon_1$, $\epsilon_z(r > a', r < b) = \epsilon_2$, $\epsilon_z(r > b) = \epsilon_3$ and $p_m^2 = \frac{\omega^2}{c^2}(n_{eff}^2(\theta) - \epsilon_m)$ with $m = 1, 2, 3$.

Equations (3.2-3.5) are solved for varying inner diameter, a', of concentric coaxial cylindrical structures to determine the radius-dependent effective index, $n_{eff}(\theta)$. The radius-dependent effective index found in each case is used to solve the angular dependence of electric field in the eccentric structure, and the propagation constant along the axial direction, β, of the mode using:

$$\frac{1}{r^2}\frac{\partial^2 E_z}{\partial \theta^2} - \beta^2 E_z + \frac{\omega^2}{c^2} n_{eff}(\theta) E_z = 0 \tag{3.6}$$

where we set $r = b$ to solve the field at the rotationally invariant outer radius. It should be noted that $n_{eff}(\theta)$ is the effective index in the "effective index method". It is only a function of θ and not the same as ϵ_z, which is a function of both r and θ. The parameters d, a, b are contained within the calculation for $(n_{eff}(\theta))$, so they do not appear explicitly in equation (3.6).

While equation (3.6) is valid for concentric structures only, it is used here to approximate the behavior of the eccentric structure within the approximation of the effective index method. In Cartesian co-ordinates, the effective index method takes a similar approximation by replacing the real problem of non-matching boundaries by one with a uniform effective index. In cylindrical co-ordinates, similar approach has been used. For the radial electric field component, this can be pictured as a thin slice surrounded by a PEC boundary Figure 3.2.

Approximate approaches to solve for the propagation constant may be used, such as the Wentzel-Kramers-Brillouin method [39]; however, due to the simplicity of this one-

dimensional differential equation, I have solved it numerically using discretization in 1 degree angular steps and using the "eig" function in Matlab to find largest eigenvalue to give β and the corresponding eigenvector for $E_z(\theta)$ of the lowest order mode, where the radial dependence considered previously is assumed constant in the effective index method. The lowest order mode is the one that has phase change in the radial electric field in the gap region. The Matlab code used for computation of effective index has been provided in Appendix A.

3.3 Effective index increase and field localization for eccentric coaxial structure

3.3.1 Infrared example comparable to recent experiments and FDMS calculation

A coaxial structure with inner island radius of 224 nm and outer radius of 286 nm, in gold for the free-space wavelength of 4 μm has been considered. These values were chosen to be similar with experiments on structures created by interference lithography [50]. At this mid-infrared wavelength the relative permittivity of gold is $-350 + 57i$.

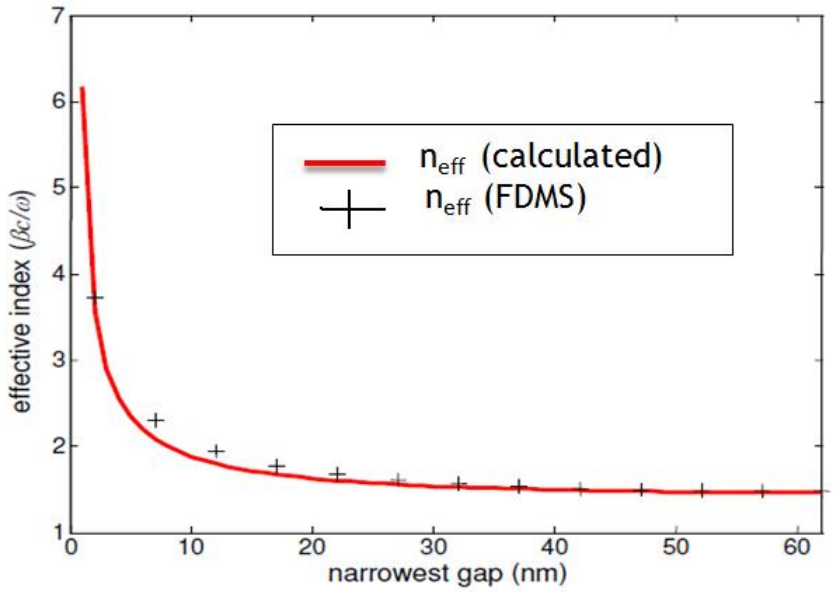

Figure 3.2: Comparison of lowest order mode effective index (β/k_0) calculated by the effective index method (line) and calculated by a comprehensive vectorial FDMS (crosses). The structure chosen is gold, with an air gap, an outer cylinder radius of 286 nm, and an inner island radius of 224 nm. The inner island is offset to produce different narrowest gap values [34].

Figure 3.2 shows the comparison between effective index (using the common definition (β/k_0), not $n_{eff}(\theta)$ as above) of the eccentric coaxial structure as calculated by the effective index method, as outlined in the previous section, and by a commercially available **finite difference mode solver (FDMS)**. The name of the commercial software is Lumerical FDTD Solutions. A good agreement has been noticed between my computed value in Matlab and that provided by commercial FDMS software. The commercial FDMS incorporates the loss of the material from an imaginary part of the relative permittivity (not shown). In principle, this can be incorporated in the effective index method; however, since the loss is small for this example, and it complicates the analysis by adding complex roots, the imaginary part of the relative permittivity is ignored.

Figure 3.3 shows the intensity of the lowest order mode of the eccentric structure computed by effective index method. The value of E_z was computed from the eigenvectors of equation (3.6). For a 60 nm shift in the center island, the field is strongly localized to a FWHM of 56° in a 2 nm gap. As shown in Figure 3.4, a similar local-

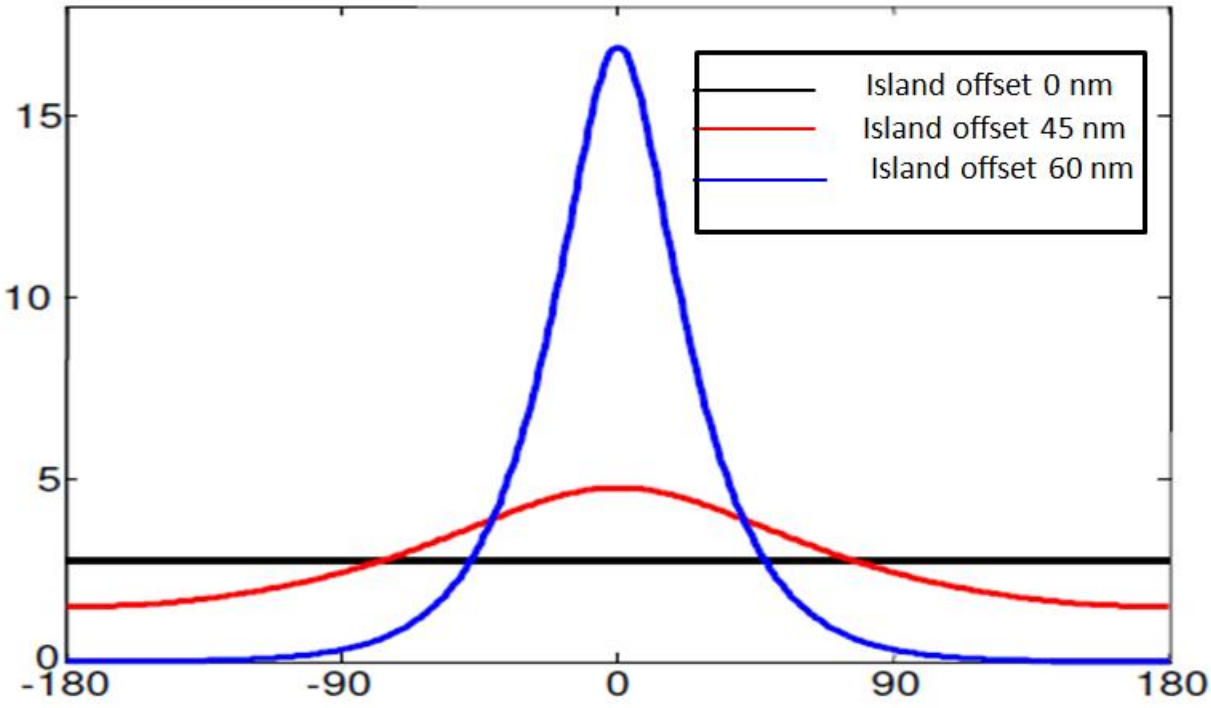

Figure 3.3: Amplitude squared of electric field of lowest order mode calculated by the effective index method for eccentric coaxial structure, described in Figure 3.2, with offset of 0 nm, 45 nm, and 60 nm (black, red, blue). The 60 nm offset has a 2 nm narrowest gap, which leads to strong field localization.

ization is seen for the comprehensive FDMS calculations ($\sim 60°$), which also contain a radial dependence.

This example shows that the effective index method provides a reasonable approximation for the field localization and effective index increase of the lowest order waveguide mode in an eccentric-coaxial structure of a plasmonic metal. In the next section the same experiment has been conducted in the visible and near-IR regime of EM spectrum.

3.3.2 Extension to visible to near-IR region and comparison with FEM calculations

These results have been investigated in the visible and near-IR region of the optical spectrum and using another metal (silver). Though the same structure has been used, wavelength and relative permittivity have been changed appropriately [41]. In this

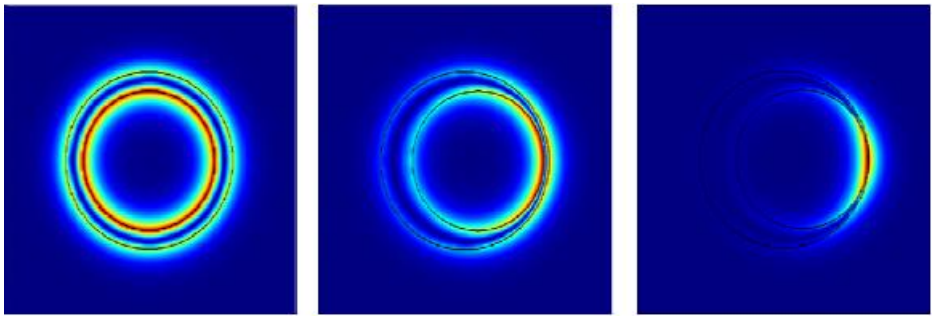

Figure 3.4: Axial component of the electric field intensity for the same structures as in Figure 3.3, with offsets of $d = 0$ nm, 45 nm and 60 nm (left to right). Normalized color scale: red-1, blue-0.

region, there is significant penetration of the electric field into the metal, which is not well-captured by the FDMS for $d > 40$ nm; even for grid sizes on 0.2 nm, beyond which the calculation did not converge. I attribute the discrepancy to the poor representation of the curved geometry using a Cartesian grid and linear interpolation of the FDMS solver.

Better agreement has been found for the effective index model calculations with a commercially available finite element method (FEM) solver. The commercial FEM solver is COMSOL Multiphysics. As shown in Figure 3.5, a comparison has been made between my computed value of effective index and that obtained from commercially avialable FEM solver for $d = 55$ nm and 60 nm, and good agreement was found between them. That figure also shows the calculated FDMS values. It is noteworthy that the FDMS calculated index actually reduces when the gap is reduced from 7 nm to 2 nm, which is contrary to the usual behavior of gap modes and is believed to be a spurious result.

3.4 Discussion

The calculation of effective index using FDMS and FEM solver are numerical techniques only and does not shed much light on the physics behind. From the discussion above, it can inferred that the localization is physically the result of the gap mode having an increase in the local index. Furthermore, since the behavior of the gap mode can be well-approximated by a simple parametric expression, the effective index method has the possibility of providing fully-analytical information about the behavior of the eccentric structure (and other cylindrical geometry structures). This

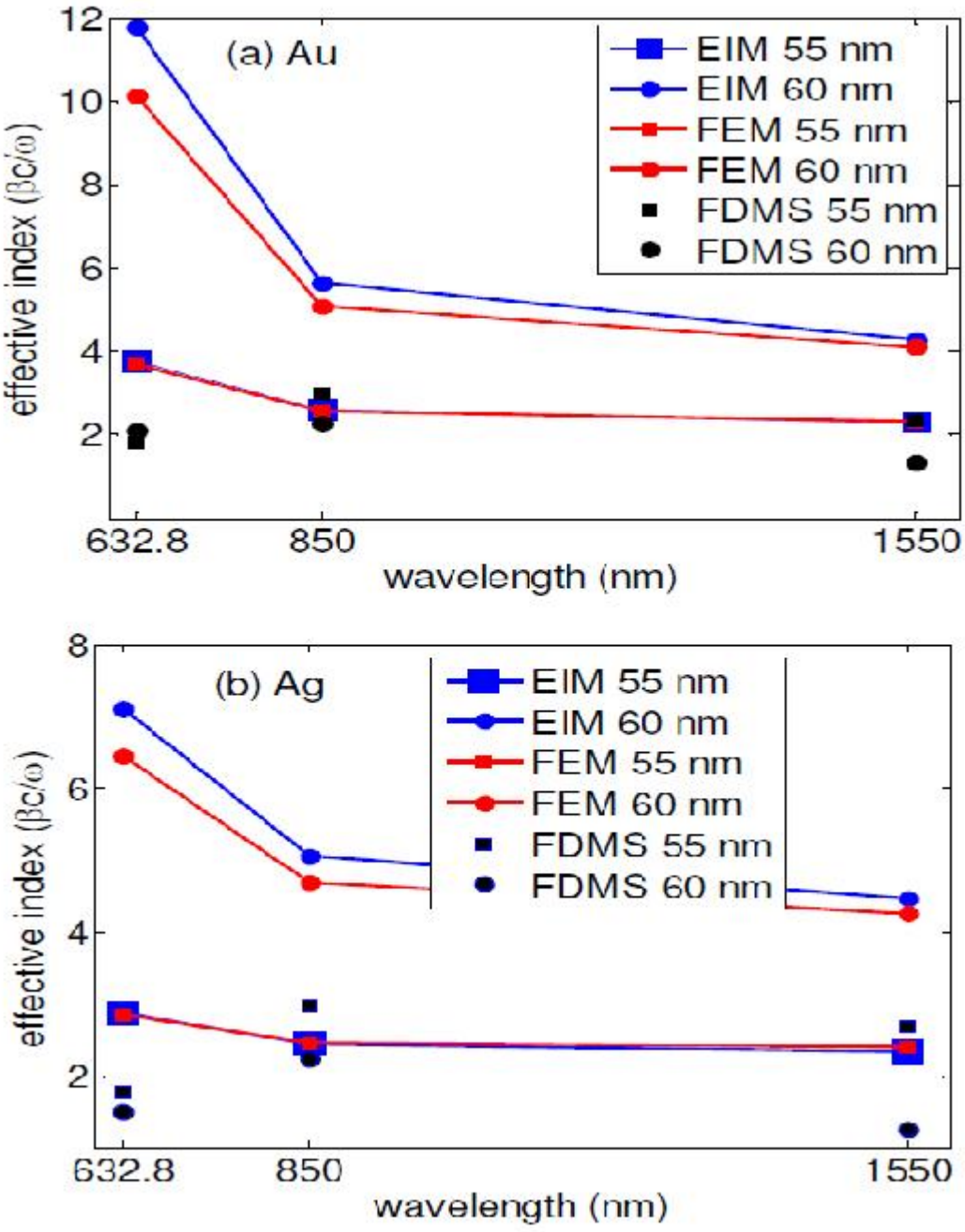

Figure 3.5: Effective index calculations for (a) gold and (b) silver in the visible and near-IR region. EIM: effective index method; FEM: finite element method; FDMS: finite difference mode solver.

will allow for rapid design and optimization of such structures. For example, all of the effective index method calculations in this chapter can be completed in less than a minute using Matlab, whereas the FDMS and FEM methods take several minutes for each case.

As could be seen from the last section, the eccentric coaxial structure allows for strong field localization in the region of the narrowest gap. This provides even greater field localization than the concentric coaxial waveguide, which has already attracted great interest from the plasmonics community. An additional benefit from the eccentric coaxial structure comes from symmetry-breaking, which introduces linear polarization to the lowest order mode. The lowest order mode of the corresponding concentric structure is radially polarized. As a result, linearly polarized light can be used to excite the lowest order mode of the eccentric structure, but not the concentric structure. This is important to practical application, when it comes to actually exciting these modes in real structures.

3.5 Summary

In this chapter I have analyzed gap plasmon mode in the eccentric coaxial structure using effective index approximation. Previously, the eccentric structure has been studied using conformal mapping technique. It has been shown analytically that the localized field enhancement in the smallest gap can be attributed to the increase in effective index of the lowest order waveguide mode. My computed values of effective index have been compared with that from a commercially available FDMS solver. The two values agreed well when the island offset was less than 40nm; beyond that they did not converge. This discrepancy has been attributed to the poor representation of the curved geometry using Cartesian grid and linear interpolation of FDMS solver. The calculation has been conducted using gold and a wavelength of 4 μm. To resolve the issue my calculated values have been compared with the values found from a commercially available FEM solver in the visible and near-IR region (also for different metal, silver) and a good agreement was found between them.

My investigation in this chapter in eccentric structure focuses on the role of gap plasmon. Practically, the structure has been fabricated using FIB and number of transmission measurements have been conducted which showed strong polarization dependence of the structure. These test results appear on a separate chapter (Chapter 6) in this work.

Chapter 4

Fabrication of nanohole arrays

4.1 Introduction

This chapter deals with the fabrication method of arrays of subwavelength holes. Nanofabrication technique can be broadly categorized into two groups: bottom-up and top-down methods. Focused ion beam (FIB) milling, which falls into the category of top-down nanofabrication technique, has been employed to create array of nanohole arrays. Since FIB is inherently destructive to the sample, scanning electron microscope (SEM) has been employed for the imaging of nanohole arrays.

The equipment used for fabrication was an FEI dual-beam Strata 235 FIB which incorporated an SEM and an EDAX X-ray analyzer. Figure 4.1 shows the work station. FIB not only permitted user to mill custom patterns, various apertures (10 pA, 30 pA, 50 pA, 100 pA, 300 pA etc.) allowed for realizing higher precision ion milling as well as using different materials as the sample. Hexalens^{TM}elctron column, part of the facility allows ultrahigh resolution imaging (upto 500K$\times$ in the normal search mode and 250K$\times$ in the UHR mode). The SEM column is vertical and the ion column is tilted 52° with the vertical. EDAX X-ray analyzer provided automated quantitative elemental analysis, live spectral collection, spectral manipulation, intensity and concentration calculations. The X-ray analyzer became particularly important during the fabrication of flow-through membranes; to ensure the membrane has been milled all the way through.

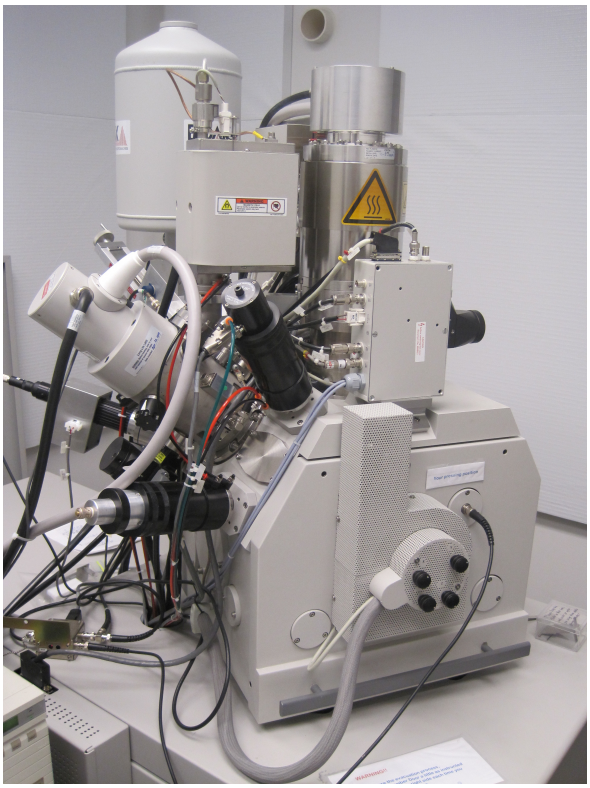

Figure 4.1: Image of FEI Strata DB 235 FIB/SEM/EDX at Simon Fraser University.

4.2 Working principle

4.2.1 Scanning electron microscope (SEM)

The scanning electron microscope (SEM) is a type of electron microscope that images the sample surface by scanning it with a high-energy beam of electrons in a raster scan pattern. The electrons interact with the atoms that make up the sample producing signals that contain information about the sample's surface topography, composition and other properties such as electrical conductivity. The types of signals produced by an SEM include secondary electrons, back-scattered electrons (BSE), characteristic X-rays, light (cathodoluminescence), specimen current and transmitted electrons.

The electron beam, which typically has an energy ranging from 0.5 keV to 40 keV, is focused by one or two condenser lenses to a spot about 0.4-5 nm in diameter. The beam passes through pairs of scanning coils or pairs of deflector plates in the electron column, typically in the final lens, which deflect the beam in the 'x' and 'y' axes so that it scans in a raster fashion over a rectangular area of the sample surface. When the

primary electron beam interacts with the sample, the electrons lose energy by repeated random scattering and absorption within a teardrop-shaped volume of the specimen known as the interaction volume. The size of the interaction volume depends on the electron's landing energy, the atomic number of the specimen and the specimen's density. The energy exchange between the electron beam and the sample results in the reflection of high-energy electrons by elastic scattering, emission of secondary electrons by inelastic scattering and the emission of electromagnetic radiation, each of which can be detected by specialized detectors. For example, secondary electrons, produced from inelastic scattering by primary electrons are captured by scintillator-photomultiplier detector which turns it into electrical signal to produce image of the surface.

4.2.2 Focused ion beam (FIB)

Focused ion beam (FIB) system operate in a similar fashion to an SEM, except, rather than a beam of electrons and as the name implies, FIB system use a finely focused beam of ions (usually gallium) that can be operated at low beam currents for imaging or high beam currents for site specific sputtering or milling. Applying an electric field to the liquid gallium source results in the emission of ions. The use of a liquid metal ion source results in high intensity of of emission over a small area. The stream of ions is focused using electrostatic lenses and the aperture size is controlled by varying the ion beam current. Beam deflection coil in the setup controls the movement of beam-spot on the sample. When the high-energy gallium ions strike the sample, they sputter atoms from the surface. Re-deposition of sputtered materials can cause problems and must be taken into consideration when using FIB.

In these methods resolution depend on the spot size of the beam meaning removal of the astigmatism during focusing is essential for proper imaging. Astigmatism is a type of optical aberration where rays that propagate in two perpendicular planes have different foci resulting in blurred image. In SEM or FIB, astigmatism prevent the formation of perfectly symmetrical beam spot. Hence for desired milling or imaging, removal of astigmatism is precondition. The instability of beam has a delirious effect on milling process. Preparation of sample in proper way and ultrahigh vacuum inside the chamber also have an important effect on the yield. Ultrahigh vacuum is created inside the chamber to remove gases of any kind to increase the mean free path of the electron and ions which in turn, increases the probability of particles to land with

appropriate energy at the intended location on the sample without being deflected on the way. The system used here had a high degree of resolution and capable of efficiently imaging 5 nm features. With stable beam condition, a 3 nm electron beam and 7 nm ion beam spot size have been used for imaging and fabricating, respectively. The deflection of the beam is computer controlled and the parameters of the patterns like periodicity, diameter or penetration can be controlled via script files.

4.2.3 EDX analysis

EDX Analysis stands for Energy Dispersive X-ray analysis. It is sometimes referred to also as EDS or EDAX analysis. It is a technique used for identifying the elemental composition of the specimen, or an area of interest. The EDX analysis system works as an integrated feature of a scanning electron microscope (SEM) and can not operate on its own without the latter.

During EDX Analysis, the specimen is bombarded with an electron beam inside the scanning electron microscope. The bombarding electrons collide with the specimen atoms' own electrons, knocking some of them off in the process. A position vacated by an ejected inner shell electron is eventually occupied by a higher-energy electron from an outer shell. To be able to do so, however, the transferring outer electron must give up some of its energy by emitting an X-ray. The amount of energy released by the transferring electron depends on which shell it is transferring from, as well as which shell it is transferring to. Furthermore, the atom of every element releases X-rays with unique amounts of energy during the transferring process. Thus, by measuring the amounts of energy present in the X-rays being released by a specimen during electron beam bombardment, the identity of the atom from which the X-ray was emitted can be established.

The output of an EDX analysis is an EDX spectrum. The EDX spectrum is just a plot of how frequently an X-ray is received for each energy level. An EDX spectrum normally displays peaks corresponding to the energy levels for which the most X-rays had been received. Each of these peaks is unique to an atom, and therefore corresponds to a single element. The higher a peak in a spectrum, the more concentrated the element is in the specimen. The EDX analysis facility incorporated with Strata 235 FEI machine was used extensively to verify the flow-through nature of the holes while fabricating nanohole arrays of gold on silicon nitride sample.

4.3 Script file

A script file when properly written and run will generate the stream file with coordinates and beam dwell time for focused ion beam milling (FIB). The stream file, alternately known as a pattern file is simply a collection of x-and y-coordinates to be milled on, with the beam dwell time required for each point.At a magnification of 5000×,the field of view is approximately 30 $\mu m \times 30$ μm generating a matrix of 4096×4096 pixels. Each pixel corresponds to a length of 7.14 nm. When writing a script file, every dimension of the structure needs to be converted into pixels using this conversion factor.

In the script file, a 4096×4096 matrix is the key variable. It may be initiated to be an all-zero matrix. Depending on the structure that is being created, some elements of this matrix can be made to hold values other than zero, for example, either the beam dwell time or 1. For structures which require fixed milling depth, it is fine to have binary values. However, for structures where variable milling depths are involved, it makes sense to fix the matrix values with their respective beam dwell times.

The script file will generate as its output, a stream file. The FIB's interface will not recognize files that do not have the .str extension. The content of a typical stream file can be divided into following parts:

1. The first line of the stream file will hold the letter 's'.

2. The second line holds a number of times the FIB is required to loop the file (a 12 in the loopcount line will make the FIB do the same set of points 12 times over). This number is not fixed and will need to be changed to suit the requirements.

3. The third line is the total number of points in the matrix that have to be milled.

4. Subsequent lines take the form of
   Beam dwell time x coordinate y coordinate

The script file will have a loop to parse the elements of the matrix and feed the coordinates of the nonzero values and their corresponding dwell time values into the stream file.

The script files were written in Matlab due to its rich function library. When the Matlab file was run it created stream files. These script file when fed to the Strata 235

FIB work station, controlled the beam spot position along the x- and y- coordinate of the ion beam. An example of a script file that generates array of nanohole array has been provided in the Appendix B.

4.4 Milling parameters

To obtain pattern with desired shape, size and depth, setting right parameters before fabrication is imperative. Some of the parameters can be controlled by FIB software interface while few of them can be controlled by changing parameters in the script file. The selection of the parameters are also influenced by the material type and thickness of the sample. The software provided preset values for silicon and germanium but since the sample used was gold, suitable values had to be picked after multiple calibration runs. The different milling parameters are:

- Accelerating voltage of the source
- Ion beam current
- Magnification
- Dwell time of the beam at each co-ordinate
- Number of times ion beam would revisit one co-ordinate; looping

The first three parameters can be selected from FIB software interface while the remaining parameters are to be incorporated into the stream files.

The amount of material sputtered from the sample directly depends on accelerating voltage and ion beam current. A higher accelerating voltage and beam current will mill a deeper hole but at the expense of broadening its desired dimension.The dwell time affects the milling in a similar manner. Hence optimum values have to be found for these parameters after making acceptable trade-offs in terms of resolution (dimension) of the structure and time taken to mill an array.

Alternatively, the ion beam can be made to revisit a co-ordinate any number of times by setting the looping parameters accordingly in the stream file. Thus by choosing a low beam current and making the beam revisit every co-ordinate repeatedly a specific number of times, can give a better shape resolution.

The machine imposed two constraints in the fabrication process. The first one emerges from the limitation of equipment's data acquisition system that forced an

upper limit to the number of dwell points which is one million. This prevents milling of large arrays which have high hole density. The other one is, the milling has to be done at a maximum magnification of 5000×. One way to resolve the issue is to interleave the co-ordinates when writing into the matrix and using an increased beam current or dwell time to accommodate for the skipped co-ordinates.

There are two types of samples that have been used. One sample is a 100 nm thick gold film on a glass slide with a 5 nm thick chromium adhesion layer. This type of sample has been obtained commercially (EMF, Ithaca, NY). The other type of sample used is a multi-window array with 9 evenly-spaced 0.1×0.1 mm square windows (a 3×3 array) centered on a 200 μm thick octagon shaped silicon frame that fits inside a 3 mm diameter circle. The multi-window permits several experiments to carry out on one sample. The spacing between window is 0.35 mm. Silicon nitride membrane is fabricated on silicon support frame and 100nm gold layer is deposited on the entire surface area of the sample. These multi-window samples are supplied commercially (Norcada Inc., Edmonton, AB). The gold-on-glass are used to fabricate arrays of dead-end holes, suitable for flowover application whereas gold-on-silicon-nitride membranes are used to mill through holes suitable for flow-through application.

4.5 Fabrication of subwavelength arrays

4.5.1 Flowover nanohole arrays

Flowover nanohole arrays are comprised of sub-wavelength holes which are dead-ended. They are used for flowover sensing application and fabricated on gold-on-glass sample. Figure 4.2 shows such an array. The array dimension is around 13×13 μm to 25×25 μm . The typical values of FIB set from the machine are: gallium ion column voltage 30 keV, ion column aperture 50 pA, ion beam current 115 pA, ion emission current 2.2 μm, beam spot size of 7. Electron column voltage is usually set to 10 to 25 keV depending on the details and clarity of the image intended. In script file the loop number is set to 10 with a dwell time of 1000 ns. From experience it has been seen that shorter dwell time and increased looping yields holes with desired diameter and depth than longer dwell time and less looping which usually yields broader feature size than intended. Chapter 5 describes in detail the use of flowover nanohole arrays as the chief sensing element in 2-color LED-based sensor.

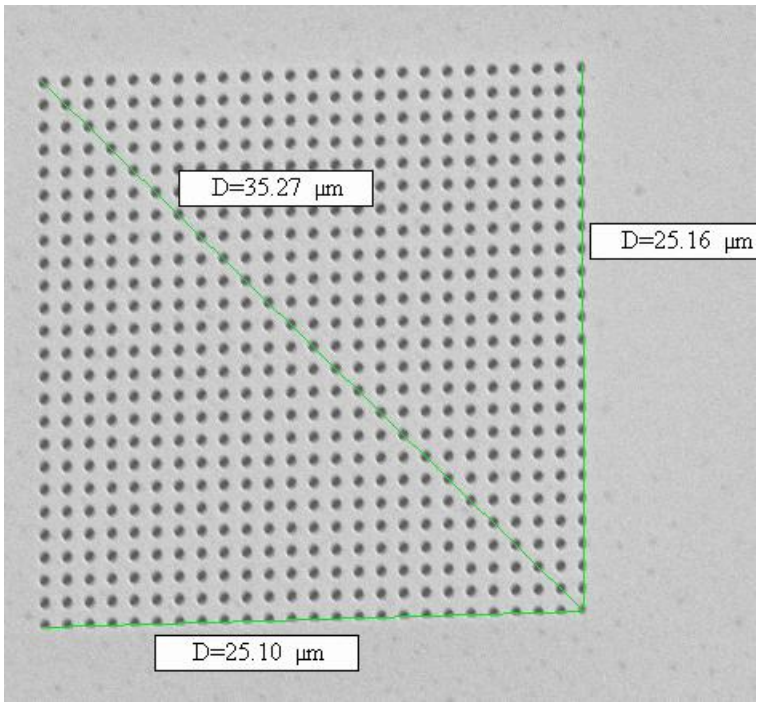

Figure 4.2: A flowover nanohole array

4.5.2 Flow-through nanohole arrays

Array of flow-through holes as sensing element can harness the benefit of nanofluidic transport along with SPR sensing which is not possible with dead-ended holes. The fabrication of flow-through arrays require different parameters to set for FIB than the flowover array. The general milling parameters are: gallium ion column voltage 30 keV, ion column aperture 100 pA, ion beam current 115 pA, ion emission current 2.2 μm, typical beam spot size of 10. In script file, the loop number is set to 50 with a dwell time of 1000 ns. Figure 4.3 is an SEM image which shows such an array in the silicon nitride window and Figure 4.4 is the cross-sectional view of the holes in the array which underscores its through nature. At normal operating voltage (5 keV), the membrane area appears indistinguishable from the frame. Only after increasing accelerating voltage over 15 keV, membrane in the window appears darker than the frame, since, at such a higher voltage the interaction volume of scanning electrons that land on the frame is higher than those that land on the membrane region. For example, the SEM image of Figure 4.3 has been taken at an accelerating voltage 25 keV. This adjustment is important to mill array inside the window. Figure 4.4, is an SEM image taken by tilting the stage 45° to show the cross-section of the

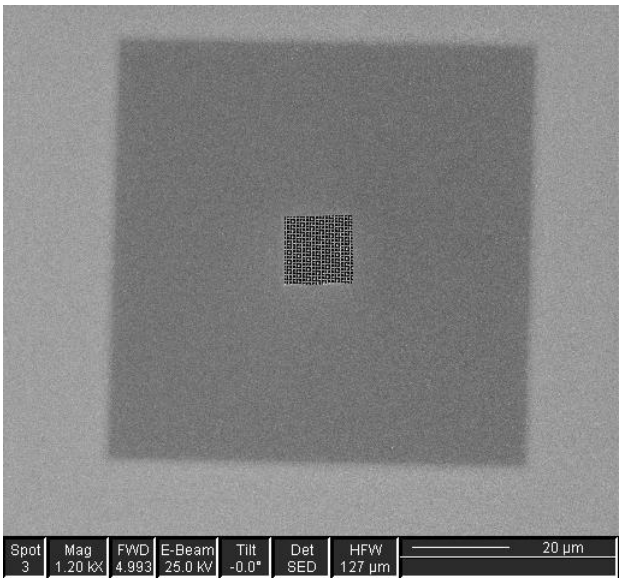

Figure 4.3: A flow-through nanohole array in the multi-window membrane.

cylindrical shaped hole. The image is demonstrating how the ion beam has penetrated the entire length of the hole.

4.6 Issues with FIB

Number of issues arose while working with FIB. They have been discussed below with a way to resolve each of them:

- Astigmatism and beam instability degrade the ability of proper focus which adversely affects the shape and size of the fabricated structure. Astigmatism causes the shape of a beam spot to change from a normal circle to an ellipse, meaning the apertures will be elliptical in shape rather than circular. Removing astigmatism or restoring the perfect circularity of the beam spot requires primarily to focus the ion beam properly. To start focusing the ion beam one should select a feature on the sample surface as an object. After setting the aperture size and beam current to be used for milling one should start focusing from a low magnification. After each incremental increase in magnification one has to focus first and secondly adjust the stigmator by turning the two knobs in x- and y-direction. It has to be continued till a magnification of ten times higher than the final magnification has been reached. Since the machine used for FIB only allows milling at 5000×, one has to go up to 50000× for desired

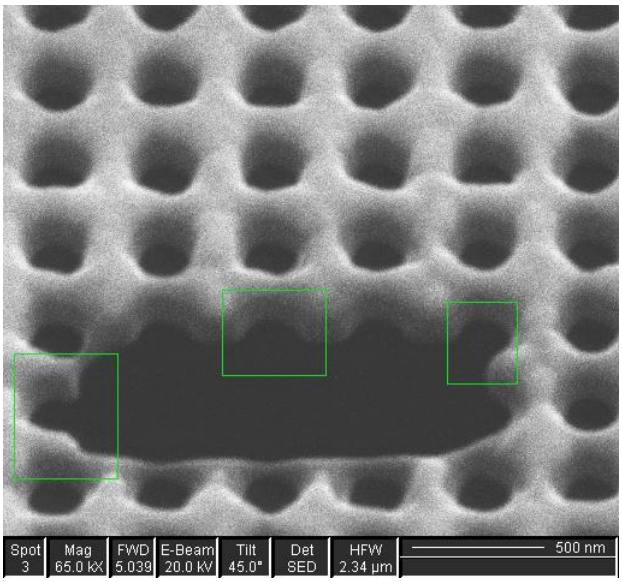

Figure 4.4: A cross-sectional view of the flow-through array.

result. At every step of magnification one should punch a hole to check its circularity. If the punched hole seems to be slightly elliptical the focusing is not going in the right direction. Figure 4.5 shows a flow chart depicting corrective measures of astigmatism. Beam instability may arise due to insufficient heating of the source or lack of proper beam alignment.

- In many cases, after the stream file is loaded, the screen might display co-ordinates are out of the filed of view, the software then displays an error message -"Not all patterns are within the field of view". This can be overcome by using a program called "runscript.exe" to run a secondary script file called "millstream.psc". This software overrides the software and force the FIB to continue milling even if the co-ordinates being out of the filed of view.

- The door of the vacuum chamber needs a manual push for a minute right after being closed.

- During the performance of a single scan of an image the scan button has to be pressed only once. In case of double click the software session expires.

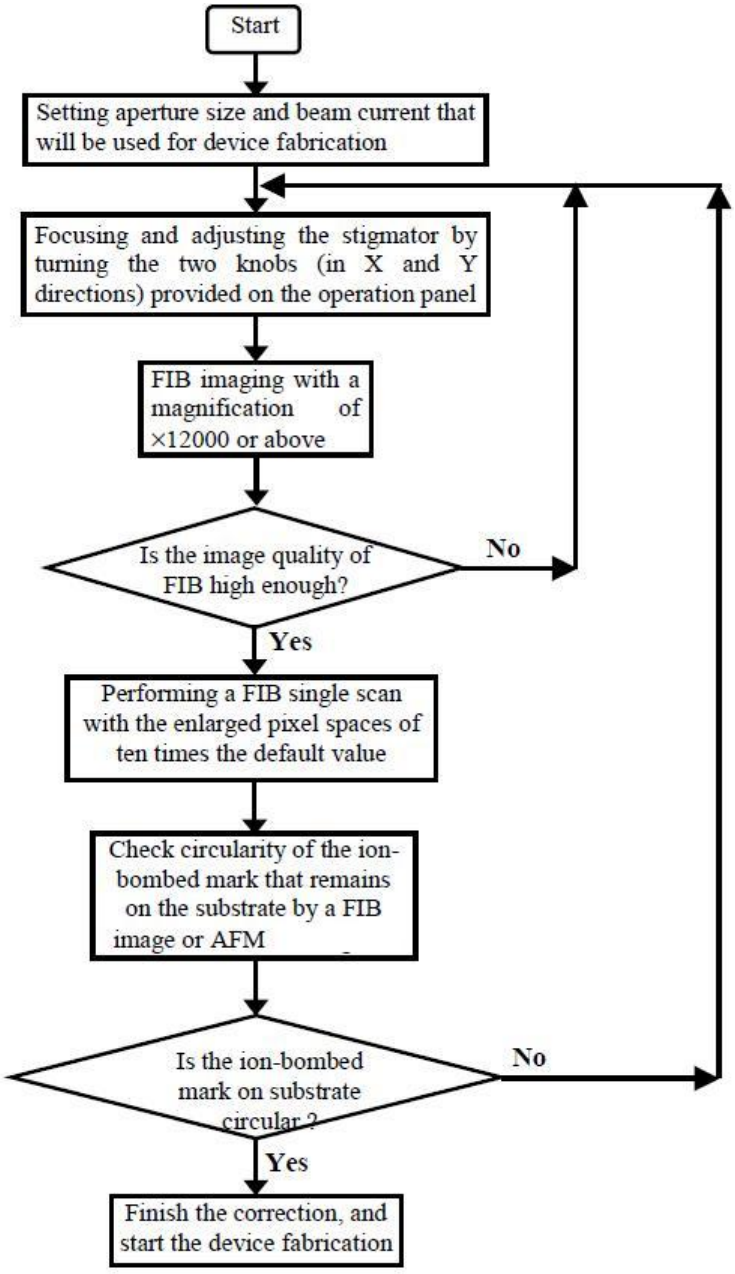

Figure 4.5: Flow chart of correction procedures of the astigmatism [26].

4.7 Summary

The chapter starts with a general discussion on the working principle of SEM, FIB and EDX analysis. It also introduced various features FEI Strata DB 235 SEM/FIB machine at Simon Fraser University that has been used for fabrication.

The following section provided a section-wise analysis of a typical stream file generated from script file. Matlab has been used for writing script file. Different milling parameters that can be adjusted from software interface and script file with their potential implication have been presented. The next section gave SEM images of flowover and flow-through nanohole arrays with a description of the milling parameters that have been used to create them. Issues like astigmatism and beam instability have been discussed at the last section with ways to resolve them.

Chapter 5

2-Color LED-based flowover nanohole sensor to detect change in refractive index

5.1 Introduction

In recent years an increase in the research activity in the understanding and potential application of enhanced optical transmission(EOT) has been noticed. One of the potential application of the phenomenon of EOT envisaged, is sensing change in refractive index. In this chapter, a novel method of detecting change in refractive index has been described based on resonant peak shift of the transmitted spectrum due to the change in the dielectric medium of the metal-dielectric interface. Array of metallic nanoholes have been used as the chief sensing element. After the introduction of a new dielectric substance in the metal-dielectric interface, mutually opposite intensity change in the transmitted light emitted from a dual wavelength LED, has been at the heart of the sensing method.

The project has been undertaken as a part of ongoing research of Lab-on-Chip (LOC) group of University of Victoria with an objective to build an integrated diagnostic tool for early cancer detection and my objective was to develop a sensing system involving commercially available 2-color LED and nanohole array. In this chapter different components of the sensing setup has been described followed by number of test results. From device integration perspective it followed the footstep of previous works [9, 11] with a major change in the way the dual color wavelength

has been driven. The test result showed for the first time the proof-of-concept that the intensity of transmitted signal from 2-color LED would go in the opposite ways whenever there is a change in dielectric material in the metal-dielectric interface. The intensity of transmitted signal was captured by charge-coupled device which in turn got projected real-time in the computer monitor.

5.2 Background information

Surface plasmon resonance (SPR) and extraordinary optical transmission (EOT) through nanohole arrays on metal films have attracted a growing research interest over the past few years. Researchers are now considering how our understanding of this phenomenon can be applied to the development of new sensing technologies. A number of previous works demonstrated the use of EOT through nanohole arrays on a thin metallic film mediated by SPR to sense the change in refractive index of the surface. Common commercial SPR-based detection, operating in reflection mode (Kretschmann configuration), suffers from the limitations of poor multiplexing, miniaturization and integration in a microfluidics system. Those limitations can be overcome by using SPR-based detection in the transmission mode which employs EOT through metallic nanohole arrays.

The challenge was to develop a sensor which would integrate EOT as the chief sensing technique with microfluidics in an on-chip format. Beside combining the interesting features of SP-mediated transmission with microfluidics architecture , the sensor should also be compact, cost effective and suitable to be used as a hand held diagnostic tool. A number of implementations have been suggested, using components such as lasers and spectrometers, but those designs are often bulky, expensive and unacceptably noisy. In this chapter an approach has been described which is simple, inexpensive and reliable: an integrated SPR imaging sensing platform using the nanohole array as the sensing element, a two-color LED source for spectral diversity and a CCD module for multiplexed detection. A polydimethylsiloxane (PDMS) microfluidic chip made by conventional photolithographic techniques has been assembled with the nanohole arrays and incorporated into the integrated module in order to transport the testing solutions, which offers the flexibility for future multiplexing.

Figure 5.1 is the conceptual diagram intended to elucidate the reason of using 2-color LED as the light source. Experimental results show that with the increase of refractive index of the dielectric medium of the metal-dielectric interface, the trans-

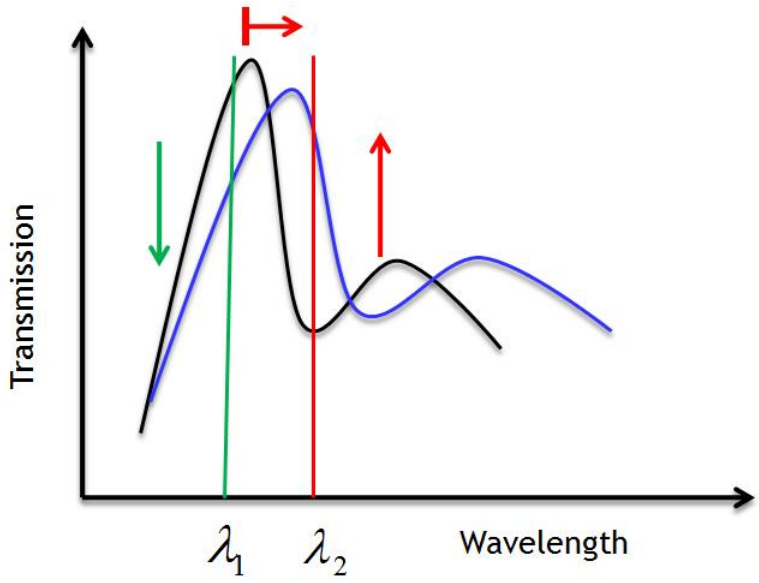

Figure 5.1: Conceptual diagram of the sensing technique.

mission spectrum from a nanohole array undergoes redshift. In the Figure 5.1, the black curve represents transmission spectrum from a nanohole array when the dielectric medium was water. When the dielectric medium was changed to sugar solution, with the increase of refractive index, the spectral characteristics underwent a redshift (blue curve). Now if the wavelengths of a dual-color LED are chosen in such a manner that, the two wavelengths fall on two opposite slopes and in proximity of a selected resonance peak, then the intensity of the light transmitted from one wavelength of the LED will increase while that from the other will decrease. By observing this mutually opposite intensity change in the transmitted light, an increase in the refractive index of the dielectric medium can be ascertained. This concept lies at the heart of sensing technique depicted in this chapter.

5.3 System description

This section will provide a detailed account of various components of the setup and the way they have been integrated to perform in the intended way which is instrumental to understand the test results.

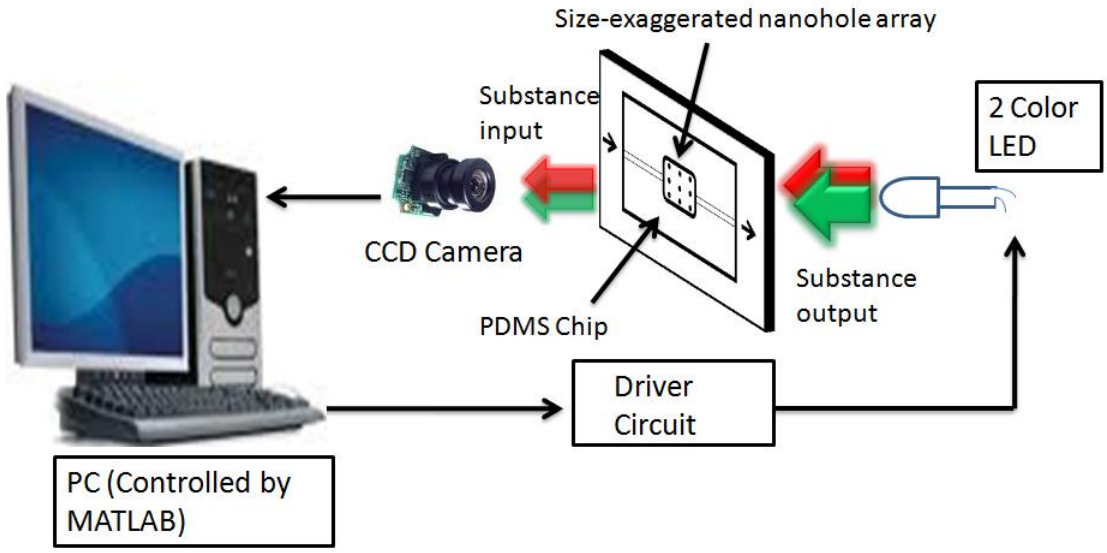

Figure 5.2: Block diagram of the sensing setup.

5.3.1 Overview

Figure 5.2 is a basic block diagram of the setup. The LED sources are controlled by a driver circuit which in turn is controlled by a Matlab program. Light transmitted from the LEDs through the nanohole arrays is captured by a CCD camera whose output is read and processed by the same Matlab program which controls the LED drivers. The array module contains both the nanohole array and a microfluidics chip which is responsible for interfacing the gold surface with selected test solutions. The output of the system is a graphical representation of the transmitted LED intensities plotted against time in Matlab. The CCD is connected to the PC via USB connection. The +5V power supply for the LEDs is fed to the driver circuit from a separate USB connector, while the control signals are passed to the driver from Matlab via two RS-232 pins.

5.3.2 Light Sources

Initially lasers and LEDs were both considered as light sources, but alignment issues are more critical in a laser implementation, and the LEDs gave a more stable output intensity, so lasers were discarded in favor of LEDs. Emitted light from LED undergoes absorption (hence attenuation) while passing through the material before reaching the CCD. Two different wavelengths will undergo unequal amount of absorption in the transmission process. For this reason, it is more reliable to use a 2-color

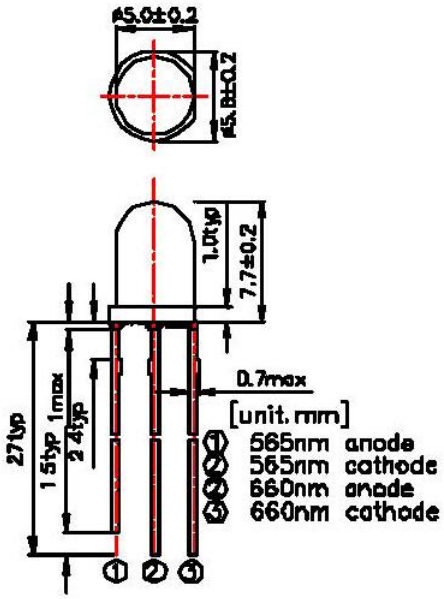

Figure 5.3: Pin-out diagram of 565/660nm bi-color LED.Outer dimensions are in mm[85].

LED than a single wavelength as the light source. The LED used were commercially available dual wavelength LED (Roithner Laser Technik,Vienna,Austria) with peak nameplate wavelength of 565/660 nm. Figure 5.3 shows the pin configuration of the LED. The maximum rated values of power dissipation by 565 nm and 660 nm wavelength are 80 mW and 75 mW while the maximum value of forward current for both the wavelength is 30 mA.

5.3.3 Driver circuit

The driver circuit has been constructed on a bread board. It has two parts, each controlling the current through a bipolar junction transistor(BJT) and one of the LEDs. The current through, hence the emitted intensity from each of the LED is controlled by potentiometer connected in series with either the collector (565nm) or emitter(660nm). The input signals to the base circuits are provided by the Matlab through RS-232 pins 7 and 4. External DC sources have been used for biasing the circuit. Figure 5.4 shows the biasing circuit.

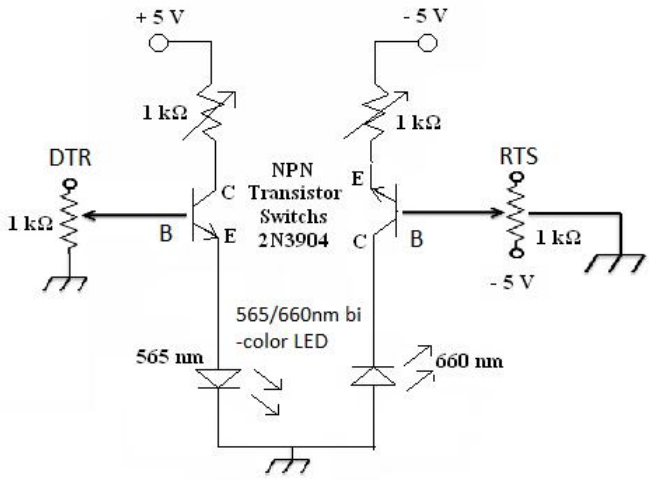

Figure 5.4: Driver circuit.

5.3.4 Nanohole arrays and microfluidics

The circular nanohole array works as the chief sensing element (shown in Figure 5.5). The dead-ended nanohole arrays, intended for flow-over sensing, were milled using a focused-ion-beam (FIB) on a 100 nm thick gold film. The gold was deposited by thermal evaporation on a 5 nm thick adhesive layer of chromium over glass slides. These samples were obtained commercially (EMF, Ithaca, NY). In the middle of the gold sample an array of 3×3 circular nanohole arrays was fabricated by FEI 235 dual-beam focused ion beam machine and imaged by a scanning electron microscope. The periodicity of all the arrays was 420 nm and the diameter was varied from 100 nm to 300 nm in a step of 25 nm. Each nanohole array has dimensions of 25×25 μm. Rows were 108 μm and columns were 79 μm apart. The milling parameters of these arrays can be found in the section 4.4.1.

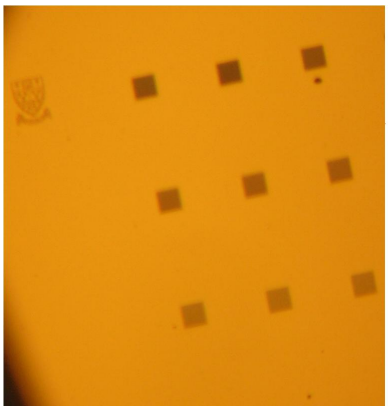

Figure 5.5: Magnified (100×) view of a 3×3 nanohole array.

In order to analyze solutions with this system, they must be placed in contact with the arrays under controlled conditions. This is accomplished with a microfluidics chip that is attached to the gold surface, over the nanohole arrays. The chip is made of polydimethylsiloxane (PDMS), which is clear and flexible, so that it does not interfere with the light transmission and is capable of making a good fluid seal at the interface. Fluids are injected into the chip from a pump or syringe while microchannels within the PDMS chip allow fluids to be transported to the arrays at the required pressures and depths. An outlet tube carries the used fluids back out of the microchannels.

The PDMS chip was fabricated using a replica molding technique. A mask with a 100 μm wide straight microchannel was drawn using computer assisted design (CAD) software. The design also included a circular inlet and circular outlet with a 1.5 mm radius intended for tubing access. Next, a master was fabricated by spin-coating a 70 μm thick layer of SU-8 50 photoresist (MicroChem Corp., Newton, MA) onto a clean 3 inch silicon wafer (Silicon Quest International Inc, Santa Clara, CA), and placing the mask over the coated wafer and exposing it to UV light for 95 seconds. The exposed wafer was post-baked for 5 minutes at 95°C and subsequently developed using SU-8 developer (MicroChem Corp., Newton, MA). After development, the master was hard baked at 65°C for 1 minute and at 95°C for 10 minutes. A degassed mixture of Sylgard 184 elastomer (Dow Corning, Midland, MI) and its curing agent at a 14:1 ratio was molded on the master. After baking at 85°C for 20 minutes, the replica was removed from the mold. Two 1 mm holes for tubing connections were then punched for fluidic access at the inlet and outlet.

The microfluidic PDMS chip was placed over the plasmonic chip with the microchannel aligned with the nanohole arrays, and then clamped together using an

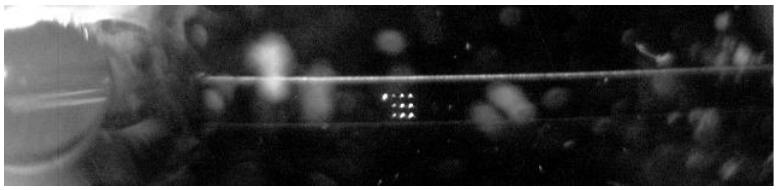

Figure 5.6: Array of 3 × 3 nanohole arrays in the microchannel.

external metallic frame. After the assembly was integrated into the rest of the sensing device, the inlet of the microfluidic chip was connected to a syringe pump (Harvard Apparatus, Holliston, MA) via 1/16" OD Fluorinated Ethylene Propylene tubing (Upchurch Scientific). Similar tubing was attached to the outlet of the microfluidic chip, leaving the distant end of the tubing at room conditions.

5.3.5 CCD

Figure 5.6 shows the light transmission as sensed by the CCD and displayed by a viewer program installed on the PC. The light intensities were quantized as pixel intensities and a number was attributed from 0 to 255 that corresponded to a particular pixel intensity; a pixel intensity of 0 corresponded to minimum intensity and 255 to maximum intensity. They were powered up by a separate USB port of the computer.

5.3.6 Matlab code

Matlab code had twofold functionalities in the setup; it sent control signal alternatively through two pins (pin 4 and 7) of computer's serial port which in turn illuminated the LEDs through driver circuit. The second thing the code did was to process the CCD images and display real-time intensity profile of transmitted light by CCD.

The basic system algorithm is as follows. Program issued two RS-232 signals, DataTerminalReady (DTR) and RequestToSend (RTS). Each of these signals controlled one of the LED sources. At the start of the program DTR gets issued and illuminated the array. The CCD was triggered, and the image was stored in Matlab as an array. The program then stepped through this array, starting at the top left hand corner of the image, looking for the first pixel element registering intensity above a certain threshold value and thereby locates the first array. The program then

divides the image into the appropriate number of array spaces by successively adding predetermined values to the row and column indices of the first array's coordinates until all of the CCD pixels had been assigned.

The program then toggled between both light sources, storing the pixel values for each image and for each array space. At each iteration, the average pixel value for each array and each source were also calculated and stored. The duration of the test can be specified by the operator. One of the arrays must be specified at the start of the test, so that the data sets for that array can be plotted in real time as the system output. The Matlab code governing the entire process has been provided in the Appendix C.

5.4 Operating procedure

1. A rectangular metallic enclosure has been used to house the sample containing nanohole arrays and PDMS chip. The enclosure had two separate parts which were connected together with four screws each at four diagonal points. First the gold sample has been placed on the rear part of the enclosure and the PDMS chip has been placed in contact with gold surface using a microscope in such a way that the array region and SFU logo falls well within the microchannel. The arrays had been fibbed approximately in the middle of the gold sample. Care should be taken to place array region halfway between inlet and outlet to ensure laminar flow of fluids over the arrays . The last step was to place front cover of the metallic enclosure on PDMS and secure it rear part using four hand-tightened screws, thus the gold sample and PDMS chip were sandwiched between two parts of metallic enclosure. The last step was to insert polymer tubing into the inlet and outlet of the PDMS chip.

2. In this step the objective was to align transmitted light from nanohole arrays with CCD. It starts by powering up the driver circuit and CCD from external DC sources and host computer, respectively. A Matlab session and software interface accompanying CCD (Videology driver version 20K135USB-SFT_07019revB) both installed in the host computer had been opened. A Matlab program for driving LEDs during alignment called test.m had been initiated. The program was basically a Matlab function which took a user defined number as its argument and toggled LEDs that many times. From the Videology

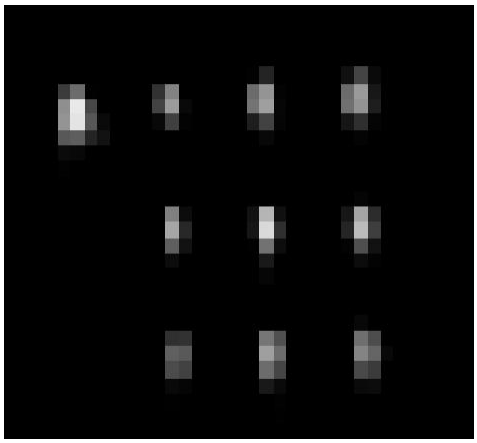

Figure 5.7: Image of 3×3 array as seen by 565 nm during alignment.

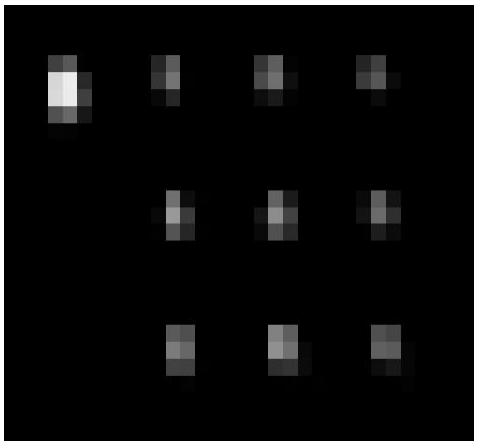

Figure 5.8: Image of 3×3 array as seen by 660 nm during alignment.

driver the shutter mode could be adjusted. Two snapshots of the array had to be taken illuminated by two LEDs at identical shutter mode for reference during alignment. Figure 5.7 and 5.8 shows such snapshots. Though the CCD had 720×480 pixels, Matlab code reduced the image size to 512×480 pixels; hence care had to be taken to align the arrays in such a manner that they fall in that region. The metallic enclosure was placed in a sample holder between LED and CCD. The sample holder allowed movement in the x- and y-direction for alignment.

3. Deionized water (refractive index, RI=1.3331) and sugar solution (RI=1.3875) had been used to flow through microchannel alternatively during experiment. There were two disposable syringes (BD syringe 1ml) that contained the fluids;

each of the syringes was driven by a syringe pump whose flow rate could be programmed. From experience it has been found that flow rate over 10 $\mu l/min$ creates excessive pressure in the tubings which often causes leak in the junctions. The experiments were conducted at 6 $\mu l/min$ flow rate. The polymer tubing from each of the syringe entered in a T-junction, which was connected to a flow-controlling on/off valve. The on/off valve and T-junction were introduced in the circuit for better isolation and noise immunity of microfluidics circuitry. The output of the on/off valve was connected to the inlet of the microchannel by another polymer tubing. The fluids flown through the microchannel were collected in the plastic container placed close to the setup.

4. At the beginning of the test both the syringe pumps were activated alternatively with the syringes filled with the fluids on them and by keeping the outlet polymer tubing of the on/off valve detached. As soon as the the liquid appeared on the outlet side of the on/off switch the pumps were stopped. The objective of this step was to fill the tubes with liquids and repel any air bubble inside the microfluidics setup. After this cautionary step the outlet of the on/off switch was reconnected with polymer tube attached to the inlet of PDMS chip.

5. The main operating Matlab code was MAM_COC_28_Arrays.m which is an acronym for multi-purpose array module core operating code. The code was written for an array of 28 nanohole arrays having 4 rows and 7 columns. The code with relevant comments appear in the Appendix C. The first step before running the code is to copy it in an empty folder, preferably within Matlab's work folder. Raw image files and output data files for arrays can be saved here.

   When the code runs first, it prompts a series of questions to user designed to help optimize the manner in which the program works. The user may hit the return key without inputting any data to accept the default settings. The questions are as follows:

   ```
   Input the filename to save raw data to (Input nothing for default:
   Rawdata)
   ```

   It is recommended to use the default name if it is later desired to graph arrays besides the one monitored live. The post-test filter program calls on files with the name Rawdata.mc, however, this is easy enough to modify.

```
Input the array number you want to monitor live (Input nothing for
default:  1)
```

The code has been designed to SFU logo at the top left corner of the viewing area. Arrays are numbered along the rows. By choosing one particular array and providing its number, its possible to monitor it live.

```
Input the desired test duration in minutes (Input nothing for default:
90 min.)
```

In most of the cases a test duration of 90 to 120 minutes is sufficient.

```
Input the amount of time in seconds each laser or LED should be active
before acquiring data (Input nothing for default:  10 s)
```

This controls how quickly the two wavelength optical sources switch–the shorter the time, the less time for the source to reach stability, however, more data points will be acquired. This step is analogous to provide sampling rate for collected data.

```
Input the desired filtering threshold as a percent above/below the
intensity average (Input nothing for default:  15)
```

Once data is acquired live and the test has completed, the data will be filtered for all arrays. This is necessary to remove any incidences of sharp intensity spikes/pits induced by the occasional presence of bubbles in the microfluidic circuitry. If the plots are very noisy and shows random behavior, it might be beneficial to increase this value, however the default of 15% is already conservative.

```
Would you like your data normalized when the test is complete?  Input
1 for YES, or 0 for NO (Input nothing for default:  1, YES)
```

If the user opt for yes, data will be normalized to unity once the test is complete. The normalized graphs will still be filtered. If the answer is no, the secondary plots will not be normalized, but still filtered.

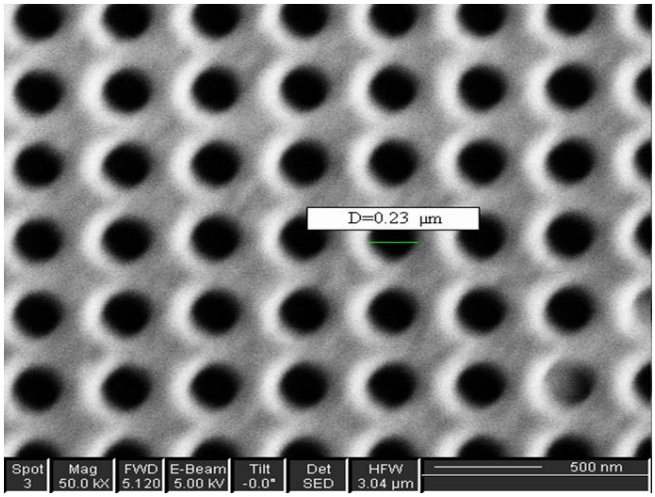

Figure 5.9: SEM image of the array used for sensing experiments.The periodicity is 420nm and hole diameter is 230nm.

5.5 Test results

A nanohole array of periodicity 420 nm and hole diameter 230 nm has been used for all the tests conducted. Figure 5.9 is the SEM image of the array.This nanohole array was chosen from an array of 3 × 3 nanohole arrays (Figure 5.5) since after collecting transmission spectrum from all the arrays in water and sugar solution, the two wavelengths of the chosen LED were found to be nearest and on two opposite slopes of the selected resonance peak for this particular array. The (1,1) resonance peak from the transmission spectrum of the nanohole array has been used for choosing wavelengths of bi-color LED since the peak is the most prominent among all the resonance peaks. Also wavelength combinations of commercially available LEDs can be found around this resonant peak wavelength. The (1,1) resonance peak can be identified from Bragg condition of resonance for rectangular nanohole array depicted in equation 2.9.

Figures 5.10, 5.11, 5.12 shows the result of three tests which is a real-time plot of average intensity of transmitted light from the selected array. Each time the dielectric medium changed from water to sugar solution or vice versa, the transmitted intensity changed, as recorded by CCD, in two opposite directions. To understand the rationale behind the intensity change, it is important to inspect Figure 5.13 carefully. Though the nameplate value of the peak wavelengths of the LED pair was 565/660 nm, practically the peak wavelengths had been noticed at 570 nm and 653 nm.

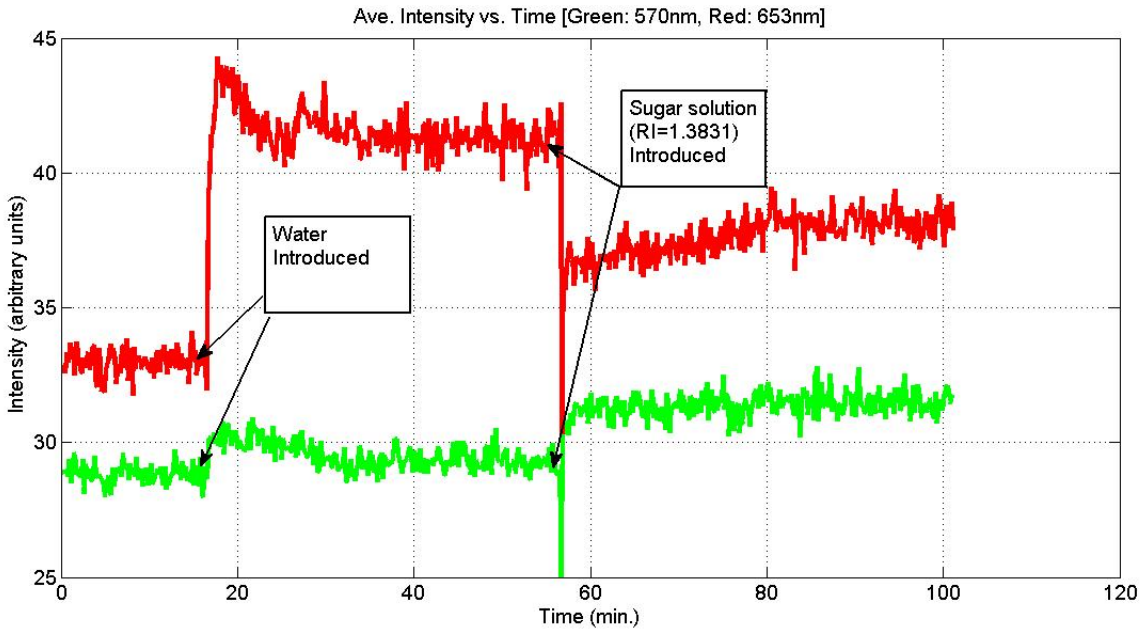

Figure 5.10: Average intensity profile for the first test.

Figure 5.13 is the transmission spectrum of the selected array in water and sugar solution. When the dielectric medium was changed from water to sugar solution, that is when the refractive index of the dielectric medium of metal-dielectric interface underwent an increment, the intensity of the transmitted light at 570 nm increased. On the opposite hand, the intensity of the transmitted light at 653 nm decreased with the increment of the refractive index of dielectric medium. In the real-time average intensity versus time plot, this phenomenon gets recorded as two opposite and simultaneous intensity change. These two wavelengths have been chosen from available wavelength combinations of commercial bi-color LED in such a manner that they fall on two opposite slopes and in close proximity of the (1,1) resonance peak of the transmitted spectrum. Also from Figure 5.13, the sensitivity of the 570 nm and 653 nm wavelengths can be computed as 200/RIU and 110/RIU, respectively.

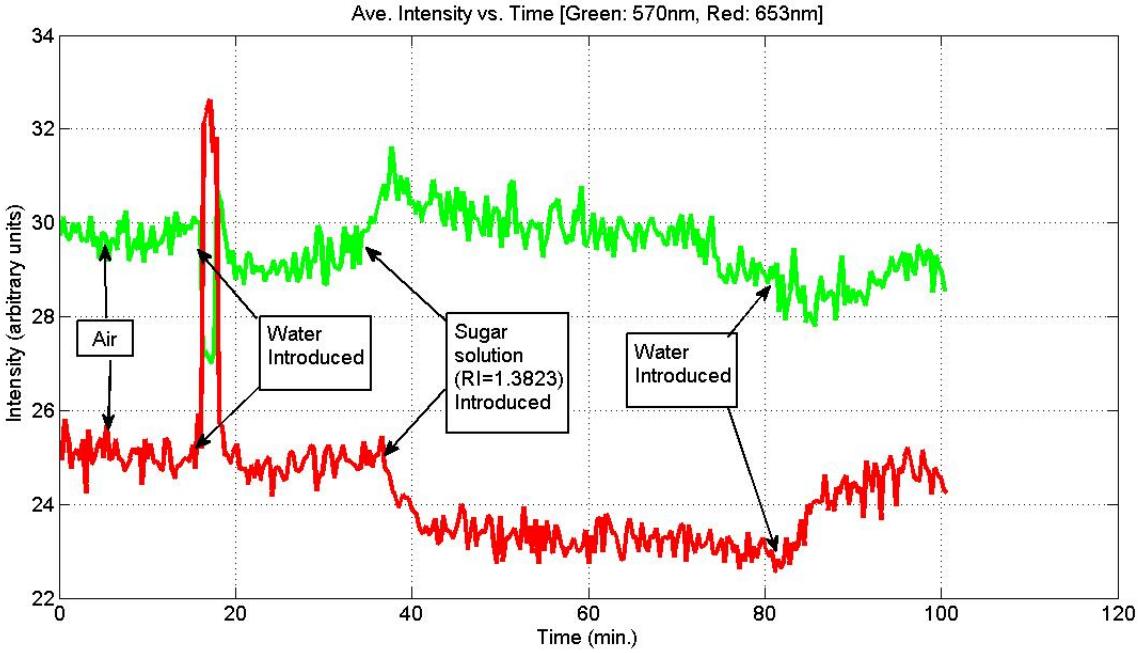

Figure 5.11: Average intensity profile for the second test.

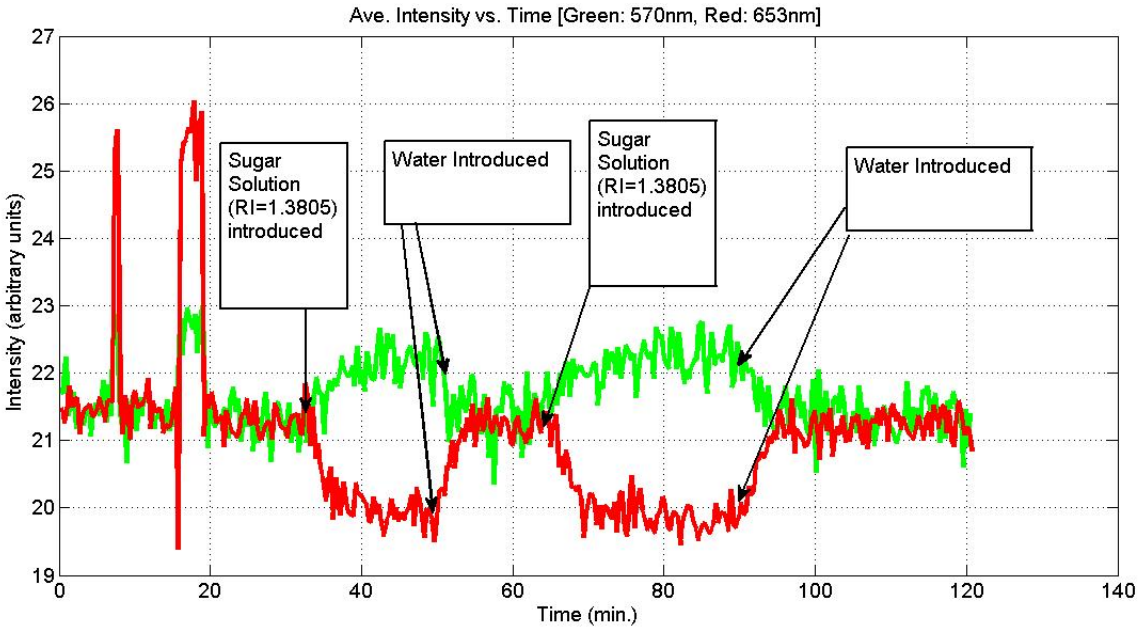

Figure 5.12: Average intensity profile for the third test.

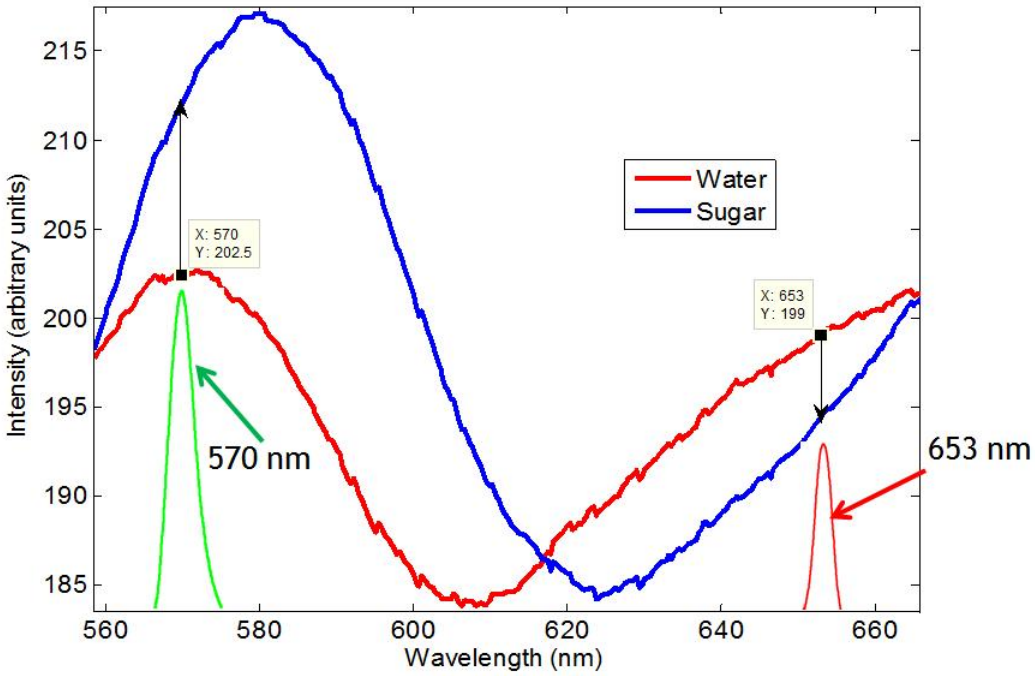

Figure 5.13: Mutually opposite intensity change of the transmitted light with an increase of refractive index of dielectric medium of the metal-dielectric interface.

5.6 Surface sensing

I have conducted three surface sensing tests which involve different concentrations of glucose solutions and water with 2-color LED sensor. First two of them were conducted in collaboration with John Campbell [11]. The driver circuit and LED pair was different (635/760 nm).

Figure 5.14 shows the result of the first test. After starting the experiment, first 15 minutes were given as a settling period during which the only dielectric in the microchannel was air. At approximately minute 15, deionized water was introduced into the microchannels and a strong response was observed in both outputs. The spike seen in the 635 nm output at around minute 18 occurred when adjustment of the fluidics tubes caused some movement in the PDMS chip, and so should be disregarded. A dilute glucose solution (refractive index 1.3352) was then used to flush the microchannels at approximately minute 28, but the response is not distinguishable from the prototype's characteristic noise, although some turbulence in the output at that time may be due to mechanical stresses on the PDMS chip caused by the flushing.

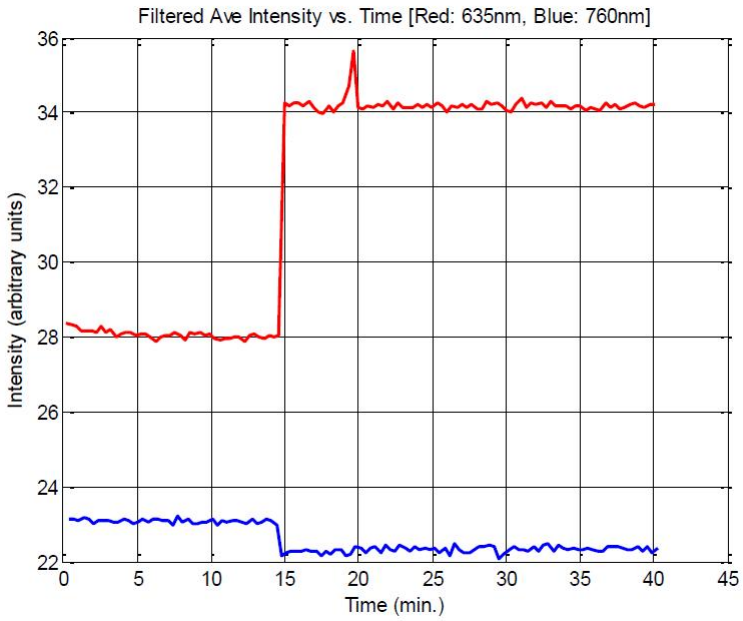

Figure 5.14: Surface sensing with air, water and glucose.

After forty minutes, the test was halted and then re-started a few minutes later as a second test.

This second test began with the same dilute glucose solution in the channels with which the first test had begun. Results are shown in Figure 5.15. At approximately minute 5, the solution was flushed out with a more concentrated glucose solution (refractive index 1.3459), and a clear response was observed in both LED outputs. At about minute 14, the microchannels were flushed with ethanol (refractive index 1.361), and a small response was visible in the 635 nm output (the initial spike can again be attributed to movements caused by the fluidics tubes), but was not clearly distinguishable in the 760 nm output. Some small intensity change in that output may actually be due to turbulence caused by mechanical stresses at the chip during flushing. More flushing with ethanol took place at around minute 25.

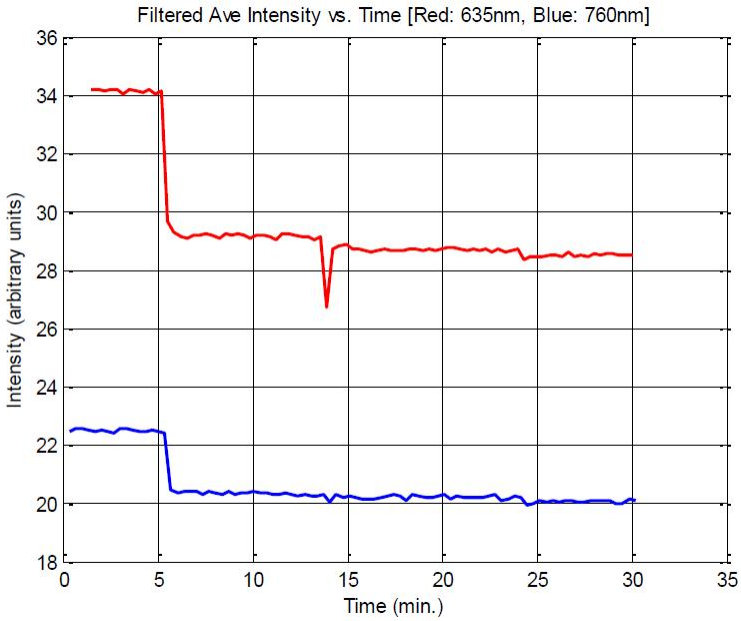

Figure 5.15: Surface sensing with glucose (two concentrations) and ethanol.

The third test was a binding test with my setup and previous LED pair (565/660 nm). Figure 5.16 shows the result from the binding test. Before the test started the gold sample was soaked with cysteamine for 24 hours. The test had a 15 minutes of settling period. At approximately minute 15, phosphate buffer saline (PBS) was introduced in the channel which triggered a strong response. Transmitted light from both the LEDs went opposite directions. After minute 15, the response of 660 nm wavelength was noise-ridden while that of the 565 nm was relatively stable. This difference can be attributed to the newly introduced zener diode in the driver circuit of 565 nm. Biotin in dimethyl sulfoxide (DMSO) was introduced at approximately 30 minute. The concentration of biotin was 2.680 mg/ml. At the moment of introducing biotin and streptavidin at minute 50, two spikes were noticed which possibly came from bubbles in the microfluidics channel. The concentration of streptavidin was 10 $\mu g/ml$. After introducing the streptavidin, biotin-streptavidin binding was noticed from minute 50 to 65. When the binding was complete, both the wavelengths showed stable response. During the binding event, the concentration of fluids inside the microchannel and hence the refractive index was changing, which in turn caused change in transmitted light.

The test had number of shortcomings like the random fluctuation of 660 nm wavelength, unwanted spikes and linear ramp of binding curve. Leaks in the microfluidics

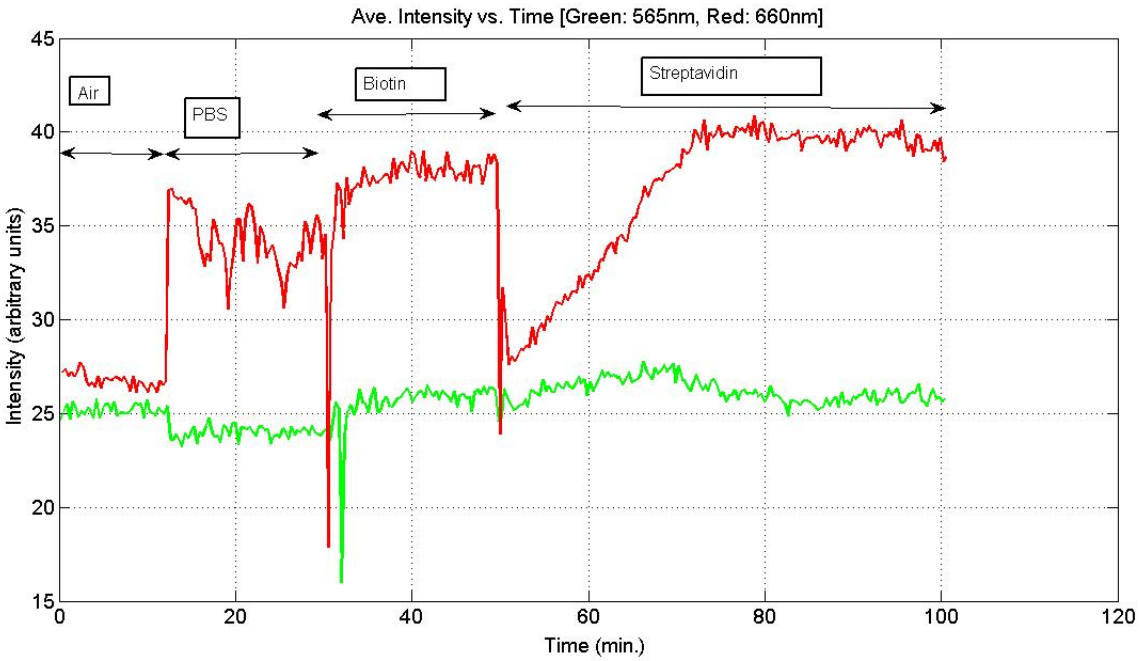

Figure 5.16: The binding experiment.

circuits was also partly responsible for spurious results. In addition, to fully understand the binding curve, the array also needs to be characterized in the organic compounds that were used in the experiment.

5.7 Evaluation of test result

Ideally the aforementioned sensing platform should be capable to register the smallest change in the transmitted light the CCD captures. The output from the CCD is analog, but is converted to a digital signal by an ADC before being sent to the viewing program as a pixel intensity value. The pixel intensities for the viewer program are on a scale of 0 to 255. The 8-bit resolution limit of the ADC restricts the obtainable sensitivity of the prototype: change in the light intensity under a certain threshold value may not be adequate to generate a pixel to a higher intensity level. In addition to this, Matlab code's behavior also dictates the degree of sensitivity achieved to some extent. After choosing a particular array to observe, the code averages the pixel intensity over a region (by default it is 8×7 pixels) around the array; how many pixels are near the top of the range of the intensities for a given quantized level contributes to determine the sensitivity when it comes to register a small change in the intensity of the transmitted light. Besides, the magnitude of change in the refractive index should not be used as the sole determining factor for the system response unless the array spectrum is fully known and hence the wavelengths of the bi-color LED are chosen accordingly.

From all the tests conducted with water and sugar solution with different refractive indices, the system appears to respond to changes in refractive index of at least 0.03 (between water and sugar solutions of various concentrations), and has an unreliable or nonexistent response to changes in refractive index that are smaller than 0.03. Test results shown in Figures 5.11 and 5.12 can be employed to compute signal to noise ratio of the output. As an example, for the test result shown in Figure 5.12 and considering the output of 570 nm LED, the maximum deviation with respect to average value is 4.2% while the maximum noise amplitude has been observed to be less than 1.8%, then an approximate lower bound to the signal to noise ratio is,

$$S/N = 4.2\%/1.8\% = 2.33$$

5.8 Summary

This chapter described the application of EOT for detecting refractive index change. A sensing platform has been demonstrated using commercially available 2-color LED which detected the change in dielectric medium of the metal-dielectric interface. The

choice of the wavelength combination has been made judiciously in such a way that they fell on two opposite sides and in close proximity of (1,1) resonance peak of the transmitted spectrum. With the change in refractive index of dielectric medium of metal-dielectric interface, the transmission spectrum underwent a red-shift which in turn caused transmitted light from one wavelength to increase while that of the other to decrease. This mutually opposite change in the intensity of captured light by CCD got manifested real-time during the test. Three test results were provided as a proof-of-concept.

Description of various parts of the sensor has been provided which include different analog circuit components, microfluidics assemblies and Matlab code. A flowover nanohole array worked as the chief sensing element. The Matlab code controlled the LEDs as well as processed images captured by CCD. The sensitivity and signal to noise ratio of the sensor has been shown.

The goal of the development of such a sensor was primarily to provide a proof-of-concept of using dual-wavelength LED for detection purpose. Hence there are number of issues that can be addressed in the present design to improve overall performance. Since the driver circuit has been built on breadboard and number of potentiometers have been used, it induced noise in the system. This can be significantly improved if a printed circuit board and fixed value discrete resistors are used instead. A CCD with higher sensitivity should effectively detect smaller refractive index change than reported. An improved alignment system should also lessen overall preparation time. The operating code is particularly vulnerable to error during the acquisition and initialization of the arrays and these system functions must be closely monitored by the operator when tests are being conducted. Undetected errors during the array selection process can lead crosstalk between arrays which contribute to the further enhancement of noise. Operating codes, whether written in Matlab or any other language should be overhauled and made more robust in terms of array selection functionalities. A better method of repelling air bubble from the microfluidics circuit would certainly eliminate unwanted spikes during experiment. The use of parallel microfluidics channels and multiple arrays will also allow future prototypes to run an arbitrary number of tests to detect change in refractive index simultaneously. Overcoming the current shortcomings in the design, as outlined here, would certainly render a reliable and robust hand held diagnostic tool for professional use.

Chapter 6

Early experimental work on eccentric structure

6.1 Introduction

In comparison to concentric structure, the eccentric geometry has number of benefits like stronger subwavelength field localiztion around the narrowest gap, improved optical coupling to the lowest order mode due to linear polarization and an increase in effective index due to gap plasmon mode. Yet, there have been no report on any experiments conducted with this structure.

In this chapter, I will present some results from transmission measurement using array of eccentric coaxial structure. Various geometric parameters have been varied like the island size, island offset and array period to observe the behavior of SPR.

6.2 Transmission experiment with eccentric structure

The array has been fabricated using FIB on a gold-on-glass sample. One of my colleague in the group, Fatemeh Eftekhari fabricated the structure in the facility at SFU and transmission measurements were conducted in the chemistry lab of Dr. Alexandre Brolo of University of Victoria. The gold layer was 100 nm thick evaporated on a float glass substrate with a 5 nm chromium adhesive layer sandwiched between them. The sample was obtained commercially (EMF, Ithaca, NY). It is well known that the x-polarization of the electric field excites a SP that propagates in the x-

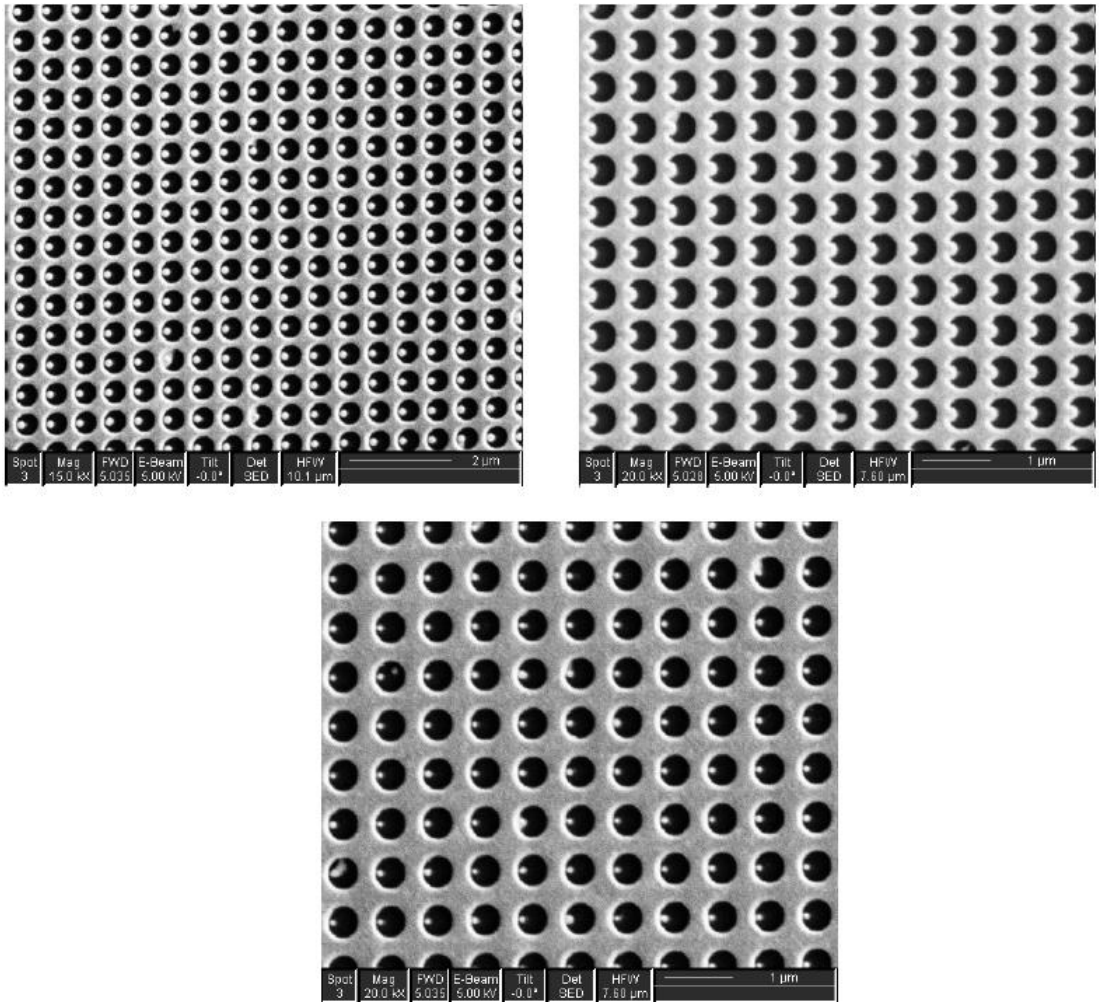

Figure 6.1: SEM pictures of eccentric coaxial structure.

direction when scattering off the holes and y-polarization excites a y-directed SP. Since the structure is asymmetric, incident x- and y- polarized light get manifested differently after the transmission. SPR from any particular incident polarization has been tuned by changing various parameters like island size, island offset and periodicity of the array.

6.2.1 Change in SPR due to island shift

The fabricated array of eccentric coaxial structure have three periodicities (550 nm, 660 nm, 650 nm). The radii of outer conductor and inner island are 200 nm and 50 nm, respectively. The change in the position of SPR for both x- and y-polarized light has been investigated as a function of center-to-center distance (d). The value of d has

been varied from 0 nm to 150 nm in a step of 25 nm. Figure 6.2 and 6.3 show the results. Halogen lamp has been used as the light source and intended polarization of the incident light has been obtained using polarizing filter. It can seen form these transmission measurement that the position of SPR is more sensitive to x-polarized light than y-polarized light and at higher periodicities of the array SPR become less sensitive to island shift for both polarizations.

6.2.2 Change in SPR due to island size

For identical period and shift from the center (550 nm and 100 nm, respectively) it can be noticed that bigger island creates more separation between SPR peaks from x- and y-polarized wave. The distance between SPR peaks from two orthogonally polarized incident waves is 40 nm when the island size is 100 nm while it is only 8 nm for an island diameter of 75 nm (Figure 6.4).

6.2.3 Change in SPR due to periodicity

Figure 6.5 and 6.6 shows the influence of array periods and island offset on SPR peak for both x- and y-polarized incident wave. For four different periodicities (500 nm, 550 nm, 600 nm and 650 nm) and for each periodicity four different island offsets ($d = 0$ (coaxial case), 50, 100 and 125 nm) have been investigated. The radii of island (R_i)and outer conductor (R_o) are 50 nm and 200 nm, respectively. It can noticed that, for both the polarization of incident light, SPR peak undergoes redshift with increasing array periodicity and island offset. This observation is in accordance with the notion of tuning SPR peak by varying periodicity.

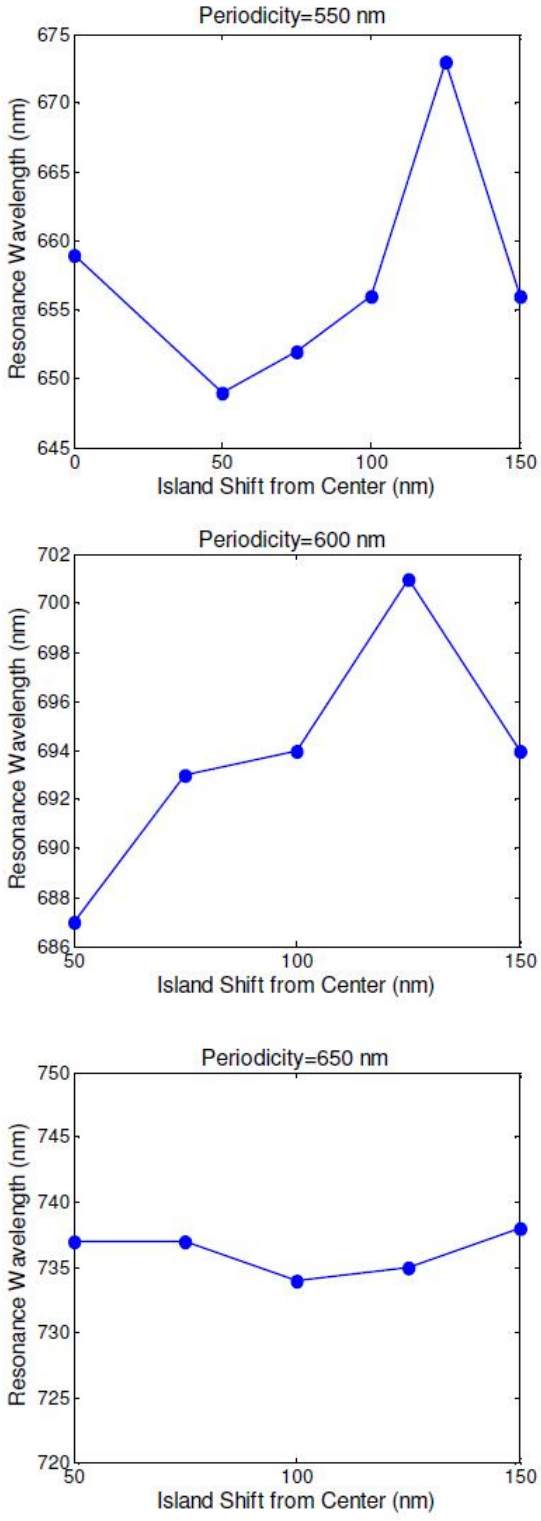

Figure 6.2: Change in SPR with island shift (X-polarized incident light); island radius $R_i = 50$ nm and radius of the outer conductor $R_o = 200$ nm.

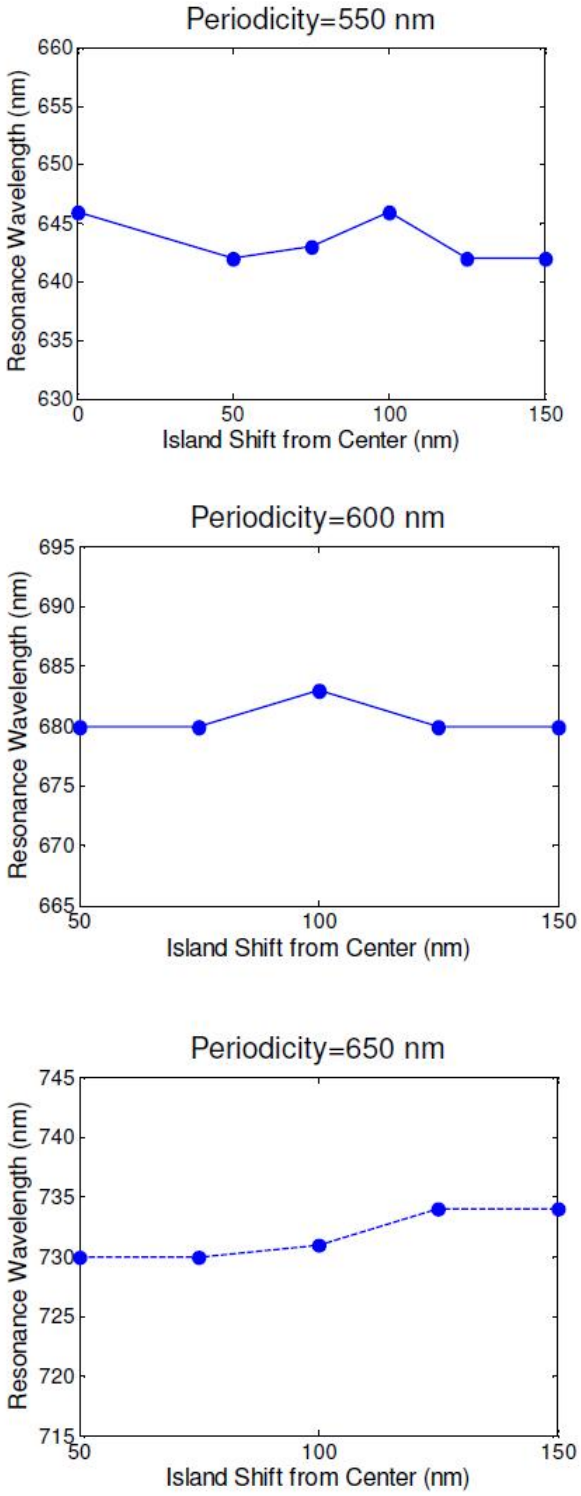

Figure 6.3: Change in SPR with island shift (Y-polarized incident light); $R_i = 50$ nm, $R_o = 200$ nm.

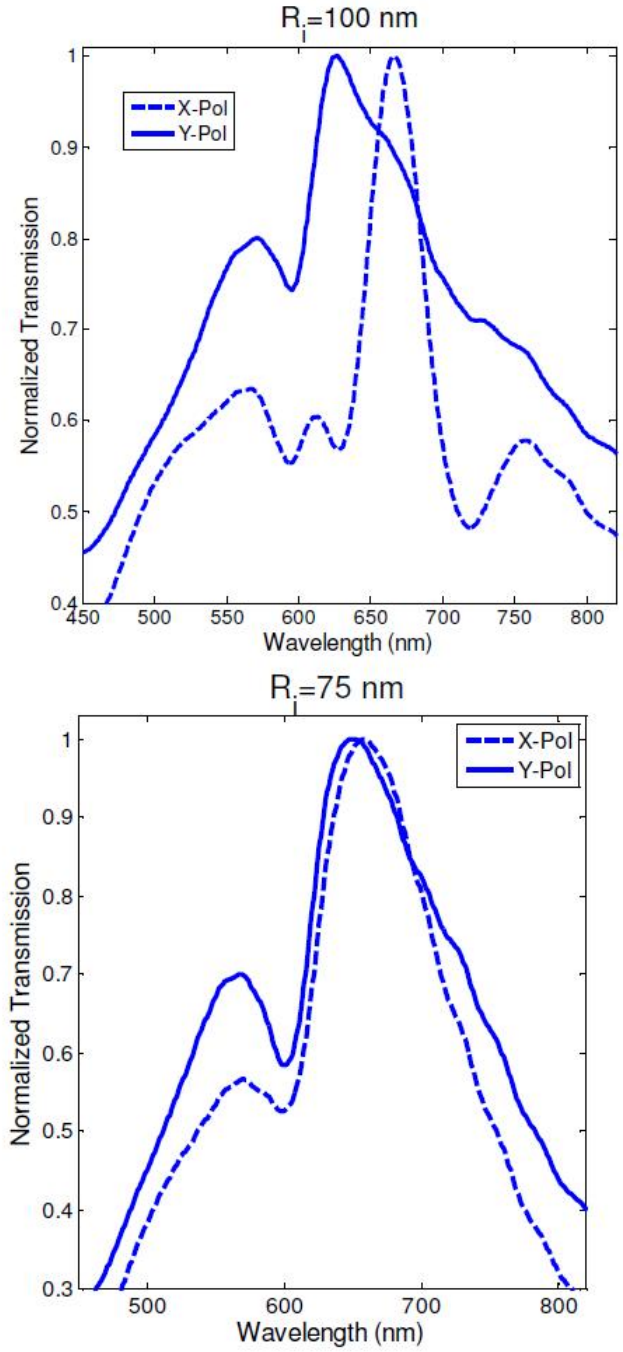

Figure 6.4: Change in SPR with island size; periodicity=550 nm, shift from center=100 nm, $R_o = 200$ nm.

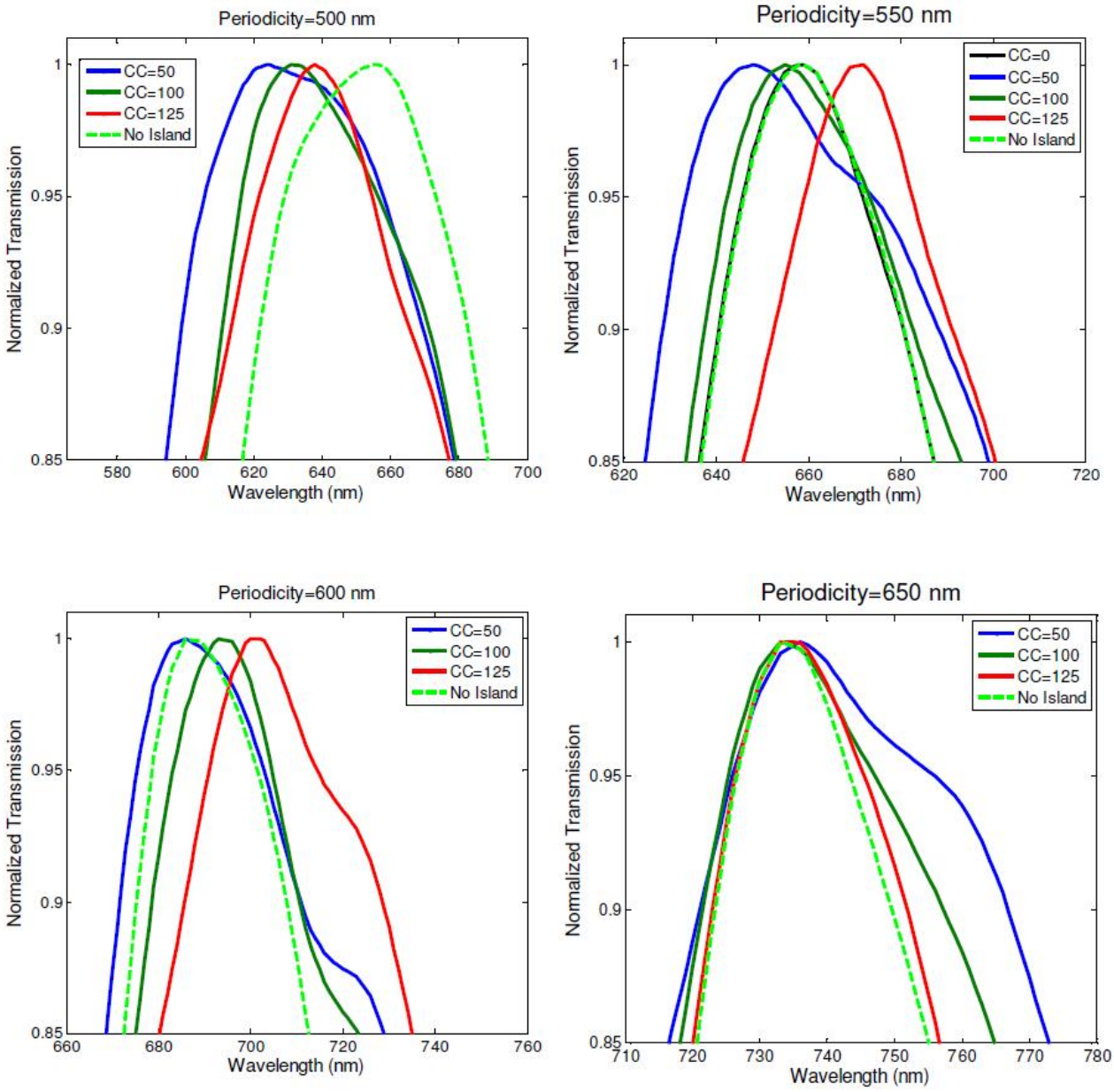

Figure 6.5: Change in SPR due to variation of center-to-center distance (d) and comparison with no-island structure (X-polarized incident wave); $R_i = 50$ nm, $R_o = 200$ nm.

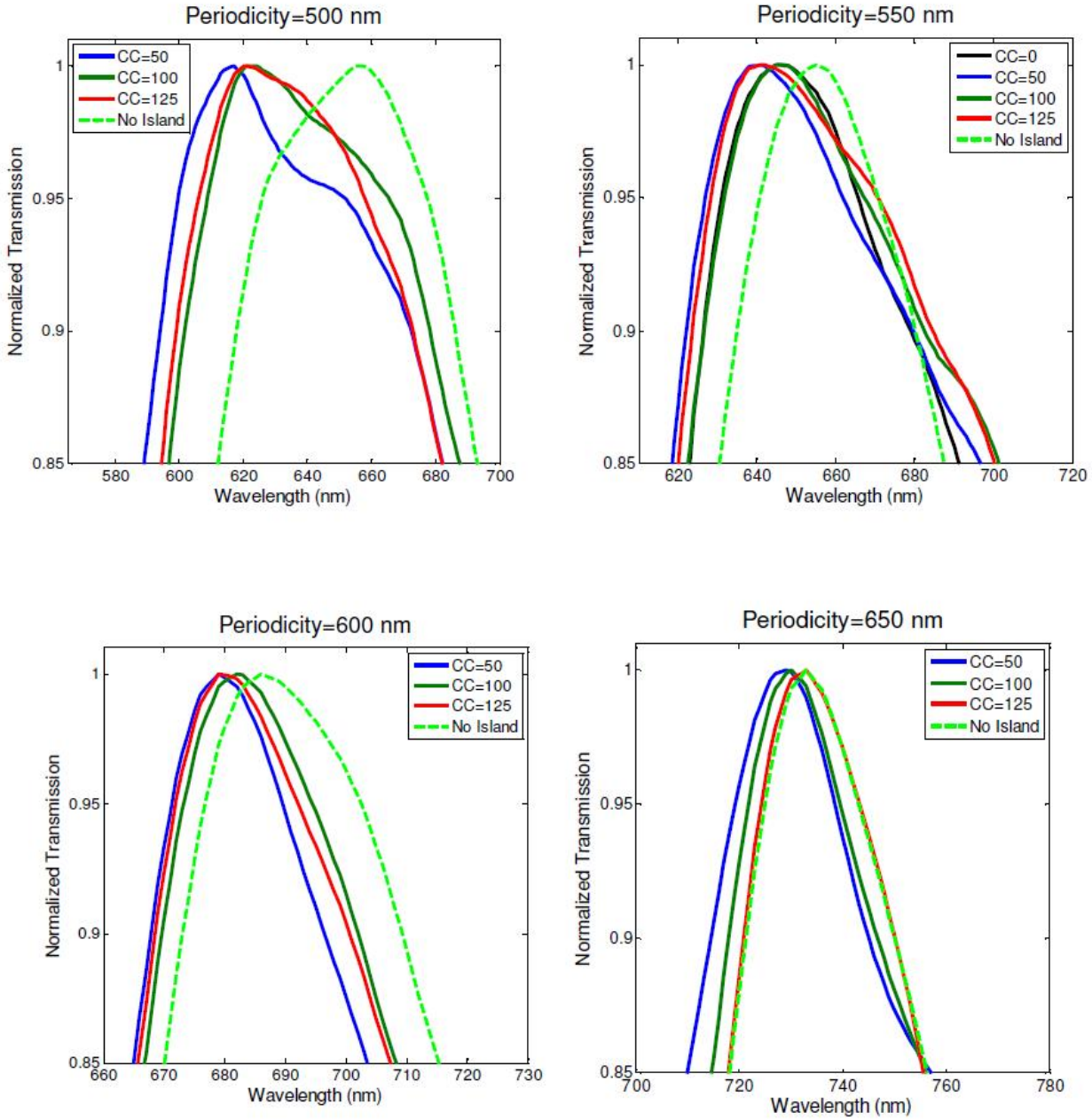

Figure 6.6: Change in SPR due to variation of center-to-center distance(d) and comparison with no-island structure(Y-polarized incident wave); $R_i = 50$ nm, $R_o = 200$ nm.

6.3 Summary

In this chapter, results from number of transmission measurements have been reported using array of eccentric coaxial structure. During fabrication, number of geometric parameters like array periodicity, island size and island offset from the center have been varied. Due to the inherent asymmetry of the structure strong polarization dependence has been noticed in the experiments. Transmission measurements from these arrays shows the prospect of tuning SPR peak by changing aforementioned parameters.

From the perspective of fabrication, the array can be milled using angled-evaporation, a method which has not been tried. Again, effort can also be made to measure the localized field intensity around the smallest gap. Therefore, the study is incomplete in terms of fabrication and measurement and hence, leaves room for future development.

Chapter 7

Conclusions

In this thesis, I have investigated gap plasmon mode of eccentric coaxial structure by using effective index approximation. In multilayer structure, each single interface can sustain SP and interactions between them creates coupled mode. The effective index of this coupled mode in the gap or gap plasmon mode depends on the separation between adjacent layers. The non-uniform gap width between inner and outer conductor in the eccentric structure increases effective index of the lowest-order waveguide mode, for example to 3.7 in the structure discussed with a 2 nm minimum gap.

The effective index method allows separation of variables which enabled me to approximate Helmholtz equation in cylindrical coordinates to a one dimensional differential equation which I have solved numerically using Matlab. The computed results found good agreement with that of the commercially available FDMS and FEM solver. Since the behavior of gap plasmon mode is well-approximated by a simple parametric equation using effective index method, it can facilitate rapid design and optimization of such structure.

In this thesis, I have also demonstrated the development of a sensor based on EOT. The sensor made use of nanohole array as the chief sensing element and a dual-wavelength LED as the light source. I have shown that if the wavelength combination of the bi-color LED is chosen judiciously so that they fall on two opposite slopes and preferably in close proximity of a selected resonant peak, a mutually opposite intensity change in the transmitted light of LEDS can be observed when the dielectric medium of metal-dielectric interface of the nanohole array undergoes a change.

I have provided a detailed discussion on the fabrication of flowover and flow-through nanohole arrays using FIB. An elaborate account of various components of

the sensing setup and number of test results to verify the proof-of-concept have been furnished in the relevant chapters. Early experimental works on eccentric structure shed light on ways to tune SPR peak by changing geometrical parameters of the array of eccentric structure. Transmission measurements showed strong polarization dependence of the structure due its inherent asymmetry.

Future work in context of eccentric structure would involve other method of fabricating such structure like angled-evaporation and determination of its field enhancement capability. Sensor performance can be improved by reducing noise in the driver circuit, overhauling the operating code and using a CCD with higher sensitivity. If the shortcomings from the microfluidics part like air bubble or leakage can be eliminated, it will certainly enhance the reliability of the sensor.

If the strong localized field of the eccentric structure can be harnessed, it will find applications in optical trapping, nonlinear optics and surface-enhanced Raman scattering (SERS). The 2-color LED-based sensor, with proper modifications, would eventually be able to be used as an integrated diagnostic tool in clinical setup.

Bibliography

[1] E. Abaka and W. Baier. Te and tm modes in transmission lines with circular outer conductor and eccentric circular innder conductor. *Electron. Lett.*, 5:251, 1969.

[2] M. Airola, Y. Liu, and S. Blair. Second-harmonic generation from an array of sub-wavelength metal apertures. *J. Opt. A-Pure Appl. Opt.*, 7:S118–S123, 2005.

[3] Fatemeh Eftekhari and Carlos Escobedo and Jacqueline Ferreira, Xiaobo Duan, Emerson M. Girotto, Alexandre G. Brolo, Reuven Gordon, and David Sinton. Nanoholes as nanochannels: Flow-through plasmonic sensing. *Analytical Chemistry*, 81(11):4308–4311, 2009.

[4] F. I. Baida, A. Belkhir, D. Van Labeke, and O. Lamrous. Subwavelength metallic coaxial waveguides in the optical range: Role of the plasmonic modes. *Physical Review B*, 74:205419, 2006.

[5] F. I. Baida and D. Van Labeke. Light transmission by subwavelength annular aperture arrays in metallic films. *Optics Communication*, 209:17–22, 2002.

[6] F. I. Baida and D. Van Labeke. Three-dimensional structures for enhanced transmission through a metallic film: Annular aperture arrays. *Physical Review B*, 67:155314, 2003.

[7] William L. Barnes, Alain Dereux, and Thomas W. Ebbesen. Surface plasmon subwavelength optics. *Nature*, 424:824–830, 2003.

[8] H. A. Bethe. Theory of diffraction by small holes. *Physical Review*, 66:163–182, 1944.

[9] J. Thomas Blakely. Flowover array sensor for substance identification, June 2009.

[10] A. G. Brolo, R. Gordon, B. Leathem, and K. L. Kavanagh. Surface plasmon sensor based on the enhanced light transmission through arrays of nanoholes in gold films. *Langmuir*, 20(12):4813–4815, 2004.

[11] John Campbell. Evaluation and management of the signal to noise ratio in the lab-on-chip (loc) prototype. Engr 446 Report, January 2010.

[12] H. Cao and A. Nahata. Influence of aperture shape on the transmission properties of a periodic array of subwavelength apertures. *Optics Express*, 12:3664–3672, 2004.

[13] C. C. Chen. Diffraction of electromagnetic waves by a conducting screen perforated periodically with holes. *IEEE Transactions on Microwave Theory and Techniques*, 19:475–481, 1971.

[14] C. Y. Chen, M. W. Tsai, T. H. Chuang, Y. T. Chang, and S. C. Lee. Extraordinary transmission through a silver film perforated with cross shaped hole arrays in a square lattice. *Applied Physics Letters*, 91:063108, 2007.

[15] J. Y. Chu, T. J. Wang, J. T. Yeh, M. W. Lin, Y. C. Chang, and J. K. Wang. Near-field observation of plasmon excitation and propagation on ordered elliptical hole arrays. *Appl. Phys. A-Mat. Scie. Proc.*, 89:387–390, 2007.

[16] R. C. Compton, R. C. McPhedran, G. H. Derrick, and L. C. Botten. Diffraction properties of a bandpass grid. *Infrared Phys.*, 23:239–245, 1983.

[17] B. N. Das and S. B. Chakrabarty. Evaluation of cut-off frequencies of higher order modes in eccentric coaxial line. *IEEE Proc. Microwaves Ant. Propag.*, 142:350–356, 1995.

[18] B. N. Das and S. B. Chakrabarty. Electromagnetic analysis of eccentric coaxial cylinders of finite length. *J. Inst. Electron. Telecom. Engin.*, 42:63–68, 1996.

[19] A. Degiron and T. W. Ebbesen. The role of localized surface plasmon modes in the enhanced transmission of periodic subwavelength apertures. *J. Opt. A-Pure Appl. Opt.*, 7:90–96, 2005.

[20] A. Degiron, H. J. Lezec, W. L. Barnes, and T.W. Ebbesen. Effects of hole depth on enhanced light transmission through subwavelength hole arrays. *Applied Physics Letter*, 81:4327, 2002.

[21] A. Degiron, H. J. Lezec, N. Yamamoto, and T. W. Ebbesen. Optical transmission properties of a single subwavelength aperture in a real metal. *Optics Communication*, 239:61–66, 2004.

[22] Thomas W. Ebbesen, H. J. Lezec, H. F. Ghaemi, T. Thio, and P. A. Wolff. Extraordinary optical transmission through sub-wavelength hole arrays. *Nature*, 391:667–669, February 1998.

[23] F. Eftekhari, R. Gordon, J. Ferreira, A.G. Brolo, and D. Sinton. Polarization-dependent sensing of a self-assembled monolayer using biaxial nanohole arrays. *Applied Physics Letters*, 92:253103, 2008.

[24] W. J. Fan, S. Zhang, K. J. Malloy, and S. R. J. Brueck. Enhanced mid-infrared transmission through nanoscale metallic coaxial-aperture arrays. *Optics Express*, 13(12):4406–4413, May 2005.

[25] W. J. Fan, S. Zhang, B. Minhas, K. J. Malloy, and S. R. J. Brueck. Enhanced infrared transmission through subwavelength coaxial metallic arrays. *Physical Review Letter*, 94:033902, 2005.

[26] Yongki Fu and Ngoi Bryan. Influence of astigmatism on the fabrication of diffractive structures by use of focused ion-beam milling. *Optics Express*, 12(17):3954–3966, 2004.

[27] F. J. Garcia-Vidal, L. Martin-Moreno, E. Moreno, L. K. S. Kumar, and R. Gordon. Transmission of light through a single rectangular hole in a real metal. *Physical Review B*, 74:153411, 2006.

[28] F. J. Garcia-Vidal, E. Moreno, J. A. Porto, and L. Martin-Moreno. Transmission of light through a single rectangular hole. *Physical Review Letters*, 95:103901, 2005.

[29] C. Genet and T.W. Ebbesen. Light in tiny holes. *Nature*, 445:39–46, 2007.

[30] H. F. Ghaemi, T. Thio, D. E. Grupp, Thomas W. Ebbesen, and J. H. Lezec. Surface plasmons enhance optical transmission through subwavelength holes. *Physical Review B*, 58:6779–6782, 1998.

[31] R. Gordon and A. G. Brolo. Increased cut-off wavelength for a subwavelength hole in a real metal. *Optics Express*, 13:1933–1938, 2005.

[32] R. Gordon, A. G. Brolo, A. McKinnon, A. Rajora, B. Leathem, and K. L. Kavanagh. Strong polarization in the optical transmission through elliptical nanohole arrays. *Physical Review Letters*, 92(3):037401, 2004.

[33] R. Gordon, A. G. Brolo, D. Sinton, and K. L. Kavanagh. Resonant optical transmission through hole-arrays in metal films: Physics and applications. *Laser and Photonics Reviews*, 4(2):311–335, 2010.

[34] R. Gordon, Asif I. K. Choudhury, and T. Lu. Gap plasmon mode of eccentric coaxial metal waveguide. *Optics Express*, 17(7):5311–5320, 2009.

[35] R. Gordon, M. Hughes, B. Leathem, K. L. Kavanagh, and A. G. Brolo. Basis and lattice polarization mechanisms for light transmission through nanohole arrays in a metal film. *Nano Lett.*, 5:1243–1246, 2005.

[36] R. Gordon, L. K. S. Kumar, and A. G. Brolo. Resonant light transmission through a nanohole in a metal film. *IEEE Trans. Nanotech.*, 5:291–294, 2006.

[37] Reuven Gordon. Surface plasmon nanophotonics:a tutorial. *IEEE Nanotechnology Magazine*, 2(3):12–18, 2008.

[38] M. I. Haftel, C. Schlockermann, and G. Blumberg. Enhanced transmission with coaxial nanoapertures: Role of cylindrical surface plasmons. *Physical Review B*, 74:235405, 2006.

[39] J. D. Jackson. *Classical Electrodynamics*. Wiley, 1998.

[40] E. Jin and X. Xu. Radiation transfer through nanoscale apertures. *J. Quant. Spectrosc. Radiat. Transfer*, 93:163–173, 2005.

[41] P. B. Johnson and R. W. Christy. Optical constants of the noble metals. *Physical Review B*, 6:4370, 1972.

[42] L. S. Jung, C. T. Campbell, T. M. Chinowsky, M. N. Mar, and S. S. Yee. Quantitative interpretation of the response of surface plasmon resonance sensors to adsorbed films. *Langmuir*, 14(19):5636–5648, 1998.

[43] J. H. Kim and P. J. Moyer. Transmission characteristics of metallic equilateral triangular nanohole arrays. *Applied Physics Letters*, 89(121106), 2006.

[44] Koerkamp, K. J. Klein, Enoch S., Segerink F. B., van Hulst N. F., and Kuipers L. Strong influence of hole shape on extraordinary transmission through periodic arrays of subwavelength holes. *Physical Review Letter*, 92(18):183901.

[45] E. Kretschmann and H. Raether. Radiative decay of non radiative surface plasmons excited by light (surface plasma waves excitation by light and decay into photons applied to nonradiative modes). *Zeitschrift Fuer Naturforschung*, 23A:2135–2136, 1968.

[46] A. Krishnan, T. Thio, T. J. Kima, H. J. Lezec, T.W. Ebbesen, P. A. Wolff, L. Martin-Moreno J. Pendry, and F. J. Garcia-Vidal. Evanescently coupled resonance in surface plasmon enhanced transmission. *Optics Communications*, 200:1–7, 2001.

[47] L. K. S. Kumar, A. Lesuffleur, M. C. Hughes, and R. Gordon. Double nanohole apex-enhanced transmission in metal films. *Applied Physics–B Laser Optics*, 84:25–28, 2006.

[48] L. K. S. Kumar, A. Lesuffleur, M. C. Hughes, and R. Gordon. Overlapping double-hole nanostructure in a metal film for localized field enhancement. *IEEE J. Sel. Top. Quantum Electron.*, 12:1228–1232, 2006.

[49] J. W. Lee, M. A. Seo, D. J. Park, D. S. Kim, S. C. Jeoung, C. Lienau, Q. H. Park, and P. C. M. Planken. Shape resonance omni-directional terahertz filters with near-unity transmittance. *Optics Express*, 14:1253–1259, 2006.

[50] A. Lesuffleur, H. Im, N. C. Lindquist, K. S. Lim, and S. H. Oh. Laser-illuminated nanohole arrays for multiplex plasmonic microarray sensing. *Optics Express*, 16(1):219–224, 2008.

[51] K. Li, M.I. Stockman, and D.J. Bergman. Self-similar chain of metal nanospheres as an efficient nanolens. *Physical Review Letters*, 91:22.

[52] Stefan A. Maier. *Plasmonics:Fundamentals and Applications*. Springer US, 2007.

[53] A. Mary, S. G. Rodrigo, L. Martin-Moreno, and F. J. Garcia-Vidal. Theory of light transmission through an array of rectangular holes. *Physical Review B*, 76:195414, 2007.

[54] J. B. Masson and G. Gallot. Coupling between surface plasmons in subwavelength hole arrays. *Physical Review B*, 73:121401, 2006.

[55] A. Moreau, G. Granet, F. I. Baida, and D. Van Labeke. Light transmission by subwavelength square coaxial aperture arrays in metallic films. *Optics Express*, 11:1131–1136, 2003.

[56] S. M. Orbons, A. Roberts, D. N. Jamieson, M. I. Haftel, C. Schlockermann, D. Freeman, and B. Luther-Davies. Extraordinary optical transmission with coaxial apertures. *Applied Physics Letter*, 90:251107, 2007.

[57] E. Popov, M. Neviere, S. Enoch, and R. Reinisch. Theory of light transmission through subwavelength periodic hole arrays. *Physical Review B*, 62:16100–16108, 2000.

[58] Y. Poujet, M. Roussey, J. Salvi, F. I. Baida, D. Van Labeke, A. Perentes, C. Santschi, and P. Hoffmann. Super-transmission of light through subwavelength annular aperture arrays in metallic films: Spectral analysis and near-field optical images in the visible range. *Photon. Nanostruct. Fundam. Appl.*, 4:47–53, 2006.

[59] X. F. Ren, P. Zhang, G. P. Guo, Y. F. Huang, Z.W. Wang, and G. C. Guo. Polarization properties of subwavelength hole arrays consisting of rectangular holes. *Applied Physics B, Lasers and Optics*, 91:601–604, 2008.

[60] A. Roberts and R. C. McPhedran. Bandpass grids with annular apertures. *IEEE Transactions on Antenna and Propagation*, 36(607–611), 1988.

[61] R. M. Roth, N. C. Panoiu, M. M. Adams, J. I. Dadap, and R. M. Osgood. Polarization-tunable plasmon enhanced extraordinary transmission through metallic films using asymmetric cruciform apertures. *Optics Letters*, 32:3414–3416, 2007.

[62] J. Salvi, M. Roussey, F. I. Baida, M. P. Bernal, A. Mussot, T. Sylvestre, H. Maillotte, D. Van Labeke, A. Perentes, I. Utke, C. Sandu, P. Hoffmann, and B. Dwir. Annular aperture arrays: study in the visible region of the electromagnetic spectrum. *Optics Letters*, 30(13):1611–1613, 2005.

[63] M. Sarrazin and J. P. Vigneron. Polarization effects in metallic films perforated with a bidimensional array of subwavelength rectangular holes. *Optics Communications*, 240:89–97, 2004.

[64] D. Sinton, R. Gordon, and A. G. Brolo. Nanohole arrays in metal films as optofluidic elements: progress and potential. *Microfluidics and Nanofluidics*, 4(1–2):107–116, 2008.

[65] Y. M. Strelniker. Theory of optical transmission through elliptical nanohole arrays. *Physical Review B*, 76:085409, 2007.

[66] M. Sun, R. J. Liu, Z. Y. Li, B. Y. Cheng, D. Z. Zhang, H. F. Yang, and A. Z. Jin. Enhanced near-infrared transmission through periodic h-shaped arrays. *Physics Letters*, 365:510–513, 2007.

[67] K. L. van der Molen, F. B. Segerink, N. F. van Hulst, and L. Kuipers. Influence of hole size on the extraordinary transmission through subwavelength hole arrays. *Applied Physics Letters*, 85:4316–4318, 2004.

[68] van der Molen K. L., K. J. Klein Koerkamp, S. Enoch, F. B. Segerink, N. F. van Hulst, and L. Kuipers. Role of shape and localized resonances in extraordinary transmission through periodic arrays of subwavelength holes: Experiment and theory. *Phys. Rev. B*, 72(4):045421.

[69] S. Wu, Q. J. Wang, X. G. Yin, J. Q. Li, D. Zhu, S. Q. Liu, and Y. Y. Zhu. Enhanced optical transmission:role of the localized surface plasmon. *Applied Physics Letters*, 93:3, 2008.

[70] T. Xu, X. Jiao, G. P. Zhang, and S. Blair. Second-harmonic emission from sub-wavelength apertures:effects of aperture symmetry and lattice arrangement. *Optics Express*, 15:13894–13906, 2007.

[71] Y. H. Ye, Z. B. Wang, D. S. Yan, and J. Y. Zhang. Role of shape in middle-infrared transmission enhancement through periodically perforated metal films. *Optics Letters*, 32:3140–3142, 2007.

[72] H. Y. Yee and N. F. Audeh. Cutoff frequencies of eccentirc waveguides. *IEEE Transactions on Microwave Theory and Technique*, 14:487, 1966.

[73] C. Yeh and F. I. Shimabukuro. *The Essence of Dielectric Waveguides*. Springer New York, 2008.

[74] S. C. Zhang. Eigenfrequency shift of higher-order modes in a coaxial cavity with eccentric inner rod. *Int. J. Infrared Millim. Waves*, 22:577–583, 2001.

[75] W. Zhang. Resonant terahertz transmission in plasmonic arrays of subwavelength holes. *European Physical Journal-Applied Physics*, 43:1–18, 2008.

Appendix A

Matlab code for computing effective index in eccentric structure

```
% clear;
clear F
a=linspace(150,285.9,100);

for counter1=1:length(a);
wl = 4000;
idx=1;

neff=1:.01:20;

for counter=1:length(neff);

    beta(counter)=2*(pi/wl)*neff(counter);

    b=286;  %radius of outer circle,286 nm

    eps1=-350;
    eps2=1;
    eps3=-350;
```

```
k1=2*(pi/wl)*sqrt(eps1);
k2=2*(pi/wl)*sqrt(eps2);
k3=2*(pi/wl)*sqrt(eps3);

p1(counter)=sqrt(beta(counter)^2-k1^2);
p2(counter)=sqrt(beta(counter)^2-k2^2);
p3(counter)=sqrt(beta(counter)^2-k3^2);

w(counter)=p2(counter)*a(counter1);
x(counter)=p1(counter)*a(counter1);
y(counter)=p3(counter)*b;
z(counter)=p2(counter)*b;


I1(counter)=besseli(0,w(counter));
I2(counter)=besseli(1,w(counter));
I11(counter)=besseli(0,x(counter));
I21(counter)=besseli(1,x(counter));

A(counter)=(I1(counter)/I11(counter))-((eps2*p1(counter))/(eps1*p2(counter)))
           *(I2(counter)/I21(counter));

K1(counter)=besselk(0,z(counter));
K2(counter)=besselk(1,z(counter));
K11(counter)=besselk(0,y(counter));
K21(counter)=besselk(1,y(counter));

B(counter)=((eps2*p3(counter))/(eps3*p2(counter)))*((-K2(counter))/
            (-K21(counter)))-(K1(counter)/K11(counter));

K3(counter)=besselk(0,w(counter));
K31(counter)=besselk(1,w(counter));
I3(counter)=besseli(0,x(counter));
I31(counter)=besseli(1,x(counter));
```

```
    C(counter)=(K3(counter)/I3(counter))-((eps2*p1(counter))/(eps1*p2(counter)))
              *((-K31(counter))/(I31(counter)));

    I4(counter)=besseli(0,z(counter));
    I41(counter)=besseli(1,z(counter));
    K4(counter)=besselk(0,y(counter));
    K41(counter)=besselk(1,y(counter));

    D(counter)=((eps2*p3(counter))/(eps3*p2(counter)))*((I41(counter))/
               (-K41(counter)))-(I4(counter)/K4(counter));

    E(idx)=abs((A(counter)*B(counter))-(C(counter)*D(counter)));

    idx=idx+1;
end

F(counter1)=neff(find(E == min(E)));

end

nem = 360;

t=linspace(0,2*pi,nem);
bob = 1;
s = 0:1:61;

for counter3=1:length(s)

ai=224;

for counter2=1:length(t);
y(counter2)=cos(t(counter2));
```

```
r(counter2)=s(counter3)*y(counter2)+sqrt((
(s(counter3)*y(counter2))^2)-(s(counter3)^2-(ai^2)));
end

h=interp1(a,F,r);

delx=2*(pi/nem)*b;
k0=2*(pi/4000);


for m=1:nem
    for n=1:nem
        if m==n
            g(m,n)=((k0^2)*(h(m)^2)+(-2)/((delx)^2));
        elseif n==m+1
            g(m,n)=(+1)/((delx)^2);
        elseif n==m-1
            g(m,n)=(+1)/((delx)^2);
        elseif abs(m-n)==(nem-1)
            g(m,n)=(+1)/((delx)^2);
        else g(m,n)=0;
        end
    end
end
[V,D]=eig(g);

neff1(bob) = sqrt(D(360,360))/k0;
bob = bob + 1;

end
```

Appendix B

Matlab code for generating stream file to mill nanohole array using FIB

```
%%%%%%%%%%%%%%%%%%%%%%%%%%%%%%%%%%%%%%%%%%%%%%%%%%%%%%%%%%%%%%%%%%%%%%%%%%%%
% Filename: Circularholes.m
% Date Created: 10th May 2009
% Decsription: Generates stream file with pixel co-ordinates to mill a
%              square array of nano-holes using FIB.
% Basis shape: Hole
%%%%%%%%%%%%%%%%%%%%%%%%%%%%%%%%%%%%%%%%%%%%%%%%%%%%%%%%%%%%%%%%%%%%%%%%%%%%
clear all;
close all;
xMin=10;
yMin=10;
%SArray=2100+xMin;
%Defining the nanometer to pixel conversion factor
NPixCon=7.14;

% Pixel Matrix
PixMat = zeros(2000);

% Opening the file input.txt and reading dimensional parameters
```

```
num = textread('noislandflowover.txt','%u%*[^\n]');

% Extracting dimensional parameters
% Height of structure
C1Rad=num(1);

% Width of structure
CPer= num(2);

% Burn Time
BTime= num(3);

% Pixel Skip factor
PSkip= num(4);

% Convert lengths from nanometers to pixels
C1RadPix=C1Rad/NPixCon;
CPerPix=CPer/NPixCon;

RP=rem(2000,CPerPix);
MaxNum=2000/CPerPix;
MaxPix=2000-10-RP;
% Defining the minimum values of x and y coordinates

BCX=xMin+C1RadPix;
BCY=yMin+C1RadPix;

for XPix=BCX:PSkip:(BCX+C1RadPix)
    for YPix=BCY:PSkip:(BCY+C1RadPix)
        a=XPix-BCX;
        b=YPix-BCY;
        if(((XPix-BCX)^2 + (YPix-BCY)^2)<=(C1RadPix^2))
           PixMat(uint16(XPix),uint16(YPix))=1;
           PixMat(uint16(BCX-a),uint16(YPix))=1;
           PixMat(uint16(XPix),uint16(BCY-b))=1;
```

```
            PixMat(uint16(BCX-a),uint16(BCY-b))=1;
             end
        end

    end

for X=xMin:2000
    for Y=yMin:2000
        if (PixMat(uint16(X),uint16(Y))==1)
            CX=X+CPerPix;
            if (CX<=2000)
                PixMat(uint16(CX),uint16(Y))=1;
            end
            CY=Y+CPerPix;
            if (CY<=2000)
                PixMat(uint16(X),uint16(CY))=1;

            end
        end
    end
end

PixCount=0;
for x=10:2000
    for y=10:2000
        if PixMat(uint16(x),uint16(y))==1
            PixCount=PixCount+1;
        end
    end
end


OutFile=strcat('./','Circle',int2str(C1Rad),'P',
int2str(CPer),'.str');
fid=fopen(OutFile,'w+');
```

```
fprintf(fid,'%c\n%u\n','s',1);
fprintf(fid,'%u\n',PixCount);
for x=10:2000
   for y=10:2000
       if PixMat(uint16(x),uint16(y)) == 1
           fprintf(fid,'%u     %u      %u\n',BTime,x,y);
       end
   end
end
fclose(fid);
```

Appendix C

Matlab code for sensor application (MAM_COC_28_Arrays.m)

```
%Copy the MATLAB core program file into an empty folder and execute the
%program from within this folder.  When MATLAB requests to change the path
%to this new folder, accept.  Raw image files and the output data file for
%the arrays will be saved here.

%Before running the program, set the exposure time (shutter speed) on the
%CCD camera using the Videology Viewer program.  Ensure that no arrays are
%saturated for both source wavelengths.


filename = input('Input the filename to save raw data to (Input
nothing for default: Rawdata): \n', 's');
if isempty(filename) == 1     %true
    filename = sprintf('%s','RawData');
end

ArrayString = input('Input the array number you want to monitor live (Input
nothing for default: 1): \n', 's');
if isempty(ArrayString) == 1
    ArrayString = sprintf('%s', '1');
end
```

```
Array = sscanf(ArrayString,'%d');
clear ArrayString

DurationString = input('Input the desired test duration in minutes (Input
nothing for default: 90 min.): \n', 's');
if isempty(DurationString) == 1
    DurationString = sprintf('%s','90');
end
Duration = sscanf(DurationString,'%d');
clear DurationString

HoldingString = input('Input the amount of time in seconds each laser or
LED should be active before acquiring data (Input nothing for default: 10 s):
\n', 's');
if isempty(HoldingString) == 1
    HoldingString = sprintf('%s','10');
end
Holding = sscanf(HoldingString,'%d');
clear HoldingString

ThresholdString = input('Input the desired filtering threshold as a percent
above/below the intensity average (Input nothing for default: 15): \n', 's');
if isempty(ThresholdString) == 1
    ThresholdString = sprintf('%s','15');
end
Threshold = sscanf(ThresholdString,'%f');
clear ThresholdString

NormalizeQString = input('Would you like your data normalized when the test
is complete? Input 1 for YES, or 0 for NO (Input nothing for default: 1, YES):
 \n', 's');
if isempty(NormalizeQString) == 1
    NormalizeQString = sprintf('%s','1');
end
NormalizeQ = sscanf(NormalizeQString,'%d');
```

```
clear NormalizeQString

fprintf('Raw data for all arrays will be written to Rawdata.mc (if default
filename inputted) \n');
fprintf('Filtered data for all arrays will be written to Rawdata-Filtered.ft \n');
fprintf('Two graphs, max. and ave. intensity, will pop-up to monitor
live the arrayselected (a single array). \n');
fprintf('When the test is concluded, two additional filtered graphs
will appear. \n');
fprintf('Introduce your test substance 20 minutes later (allows for
source settling). \n');

%Initialize CCD camera
CCD=videoinput('winvideo',1);
triggerconfig(CCD,'Manual');
set(CCD, 'FramesPerTrigger',1);
set(CCD,'ReturnedColorSpace' , 'grayscale');
set(CCD,'TriggerRepeat',Inf);
set(CCD,'ROIPosition',[0,0,512,480]); %[x,y,width,height] --
%top, left corner is the origin, down/right is positive.
%MATLAB will reduce the CCD image size to 512x480, regardless of if you try
%to use the max CCD size of 720x480.

start(CCD);
pause(Holding);
%Initialize lasers/LEDs
SerialPort=serial('COM1');
%Plug the serial, RS-232 cable into Com2
fopen(SerialPort);
%565nm source, set to off
set(SerialPort,'DataTerminalReady','off');
%660nm source, set to off
set(SerialPort,'RequestToSend','off');
%These ports must be set to 'off' in this order for proper operation
```

```
%Initialize auto selection of arrays
set(SerialPort,'DataTerminalReady','on'); %Activate 565nm source
pause(Holding); %Program waits for time specified above for source
                %holding time
trigger(CCD); %Take picture

TestImage=getdata(CCD); %Picture saved to variable, TestImage
intmin(class(TestImage))
intmax(class(TestImage))
set(SerialPort,'DataTerminalReady','off');
%Deactivate 565nm source

%Find the row (R) and column (C) for which a light intensity value greater
%than 20 is spotted. Intensity of 16 is black (zero intensity). This auto
%selection script
%assumes that the SFU logo is at the top left of the image. Auto-selection
%of arrays will not properly function if there are scratches on the array
%for which light is being transmitted into the CCD, however scratches are
%not typically an issue for sufficiently short CCD exposure times when
%using columinated laser sources.
[R C] = find(TestImage >= 20); %Find all pixels greater than intensity 20
aa=TestImage(199,434);
aaa=TestImage(201,434);
bb=TestImage(199,433);
cc=TestImage(201,457);
ColumnStartSearch = C(1)+8; %SFU logo found at C(1). Add 6 pixel columns
%and search for the 1st column pixel of the 1st array
ColumnIndex = find(C > ColumnStartSearch);
%1st array index found from the list, R C
FirstColumnArray = C(ColumnIndex(1))  %1st array pixel column location
%(not index)
FirstRowArray = min(R);
%1st array pixel row location should be the same as the logo
% StartHereC  = FirstColumnArray-4+4+4 %subtract 2 pixel columns
%to account for array illumination differences with the other light source
```

```
% StartHereR = FirstRowArray-2 %subtract 2 row columns
StartHereR=293;
StartHereC=459;
%result=zeros(3000);
iteration = (60*Duration)/(2*Holding);
for i=1:iteration

%505nm source ON
set(SerialPort,'DataTerminalReady','on');
pause(Holding);

%The below crops can probably placed into a sub-loop to reduce coding lines.
trigger(CCD);
[data time] = getdata(CCD); %Full CCD image data and time, in seconds
datacropA01 = imcrop(data,[StartHereC,StartHereR,8,7]); %crops image data
datacropA02 = imcrop(data,[StartHereC+(1*8),StartHereR,8,7]);
datacropA03 = imcrop(data,[StartHereC+(8+7),StartHereR,8,7]);
datacropA04 = imcrop(data,[StartHereC+(8+7+7),StartHereR,8,7]);
datacropA05 = imcrop(data,[StartHereC+(8+7+7+8),StartHereR,8,7]);
datacropA06 = imcrop(data,[StartHereC+(8+7+7+8+8),StartHereR,8,7]);
datacropA07 = imcrop(data,[StartHereC+(8+7+7+8+7),StartHereR,8,7]);
datacropA08 = imcrop(data,[StartHereC,StartHereR+7,8,7]);
datacropA09 = imcrop(data,[StartHereC+(1*8),StartHereR+7,8,7]);
datacropA10 = imcrop(data,[StartHereC+(8+7),StartHereR+7,8,7]);
datacropA11 = imcrop(data,[StartHereC+(8+7+7),StartHereR+7,8,7]);
datacropA12 = imcrop(data,[StartHereC+(8+7+7+8),StartHereR+7,8,7]);
datacropA13 = imcrop(data,[StartHereC+(8+7+7+8+8),StartHereR+7,8,7]);
datacropA14 = imcrop(data,[StartHereC+(8+7+7+8+8+7),StartHereR+7,8,7]);
datacropA15 = imcrop(data,[StartHereC,StartHereR+7+6,8,7]);
datacropA16 = imcrop(data,[StartHereC+(1*8),StartHereR+7+6,8,7]);
datacropA17 = imcrop(data,[StartHereC+(8+7),StartHereR+7+6,8,7]);
datacropA18 = imcrop(data,[StartHereC+(8+7+7),StartHereR+7+6,8,7]);
datacropA19 = imcrop(data,[StartHereC+(8+7+7+8),StartHereR+7+6,8,7]);
datacropA20 = imcrop(data,[StartHereC+(8+7+7+8+8),StartHereR+7+6,8,7]);
datacropA21 = imcrop(data,[StartHereC+(8+7+7+8+8+7),StartHereR+7+6,8,7]);
```

```
datacropA22 = imcrop(data,[StartHereC,StartHereR+7+6+7,8,7]);
datacropA23 = imcrop(data,[StartHereC+(1*8),StartHereR+7+6+7,8,7]);
datacropA24 = imcrop(data,[StartHereC+(8+7),StartHereR+7+6+7,8,7]);
datacropA25 = imcrop(data,[StartHereC+(8+7+7),StartHereR+7+6+7,8,7]);
datacropA26 = imcrop(data,[StartHereC+(8+7+7+8),StartHereR+7+6+7,8,7]);
datacropA27 = imcrop(data,[StartHereC+(8+7+7+8+8),StartHereR+7+6+7,8,7]);
datacropA28 = imcrop(data,[StartHereC+(8+7+7+8+8+7),StartHereR+7+6+7,8,7]);
%Cropping assumes 4 rows, 7 columns.  Alter cropping code if different.
%The data cropping for all 28 arrays assumes particular sizes and spacings
%between arrays.  More advanced auto-selection methods can be used here at
%a later time, such as one that uniquely identifies each non-zero pixel,
%and draws an array box based on these locations.  For the current code, as
%long as the CCD distance with respect to the array is not heavily altered,
%this cropping method will work.  In a final device, this distance will
%not be alterable, so altering this part of the code may not be necessary.

%result(ith row, then column) for 565nm source
result(i,1) = time/60; %convert time from seconds to minutes
result(i,2) = max (datacropA01(:)); %finds max value for 1st array and
result(i,3) = max(datacropA02(:)); %places this value into 'result' column
result(i,4) = max(datacropA03(:));
result(i,5) = max(datacropA04(:));
result(i,6) = max(datacropA05(:));
result(i,7) = max(datacropA06(:));
result(i,8) = max(datacropA07(:));
result(i,9) = max(datacropA08(:));
result(i,10) = max(datacropA09(:));
result(i,11) = max(datacropA10(:));
result(i,12) = max(datacropA11(:));
result(i,13) = max(datacropA12(:));
result(i,14) = max(datacropA13(:));
result(i,15) = max(datacropA14(:));
result(i,16) = max(datacropA15(:));
result(i,17) = max(datacropA16(:));
result(i,18) = max(datacropA17(:));
```

```
result(i,19) = max(datacropA18(:));
result(i,20) = max(datacropA19(:));
result(i,21) = max(datacropA20(:));
result(i,22) = max(datacropA21(:));
result(i,23) = max(datacropA22(:));
result(i,24) = max(datacropA23(:));
result(i,25) = max(datacropA24(:));
result(i,26) = max(datacropA25(:));
result(i,27) = max(datacropA26(:));
result(i,28) = max(datacropA27(:));
result(i,29) = max(datacropA28(:));
result(i,30) = mean2(datacropA01(:)); %finds the average array intensity
result(i,31) = mean2(datacropA02(:));
result(i,32) = mean2(datacropA03(:));
result(i,33) = mean2(datacropA04(:));
result(i,34) = mean2(datacropA05(:));
result(i,35) = mean2(datacropA06(:));
result(i,36) = mean2(datacropA07(:));
result(i,37) = mean2(datacropA08(:));
result(i,38) = mean2(datacropA09(:));
result(i,39) = mean2(datacropA10(:));
result(i,40) = mean2(datacropA11(:));
result(i,41) = mean2(datacropA12(:));
result(i,42) = mean2(datacropA13(:));
result(i,43) = mean2(datacropA14(:));
result(i,44) = mean2(datacropA15(:));
result(i,45) = mean2(datacropA16(:));
result(i,46) = mean2(datacropA17(:));
result(i,47) = mean2(datacropA18(:));
result(i,48) = mean2(datacropA19(:));
result(i,49) = mean2(datacropA20(:));
result(i,50) = mean2(datacropA21(:));
result(i,51) = mean2(datacropA22(:));
result(i,52) = mean2(datacropA23(:));
result(i,53) = mean2(datacropA24(:));
```

```
result(i,54) = mean2(datacropA25(:));
result(i,55) = mean2(datacropA26(:));
result(i,56) = mean2(datacropA27(:));
result(i,57) = mean2(datacropA28(:));

set(SerialPort,'DataTerminalReady','off'); %turn off 565nm source

%Save the full raw image
imname=strcat(strcat('635image-FULL-',sprintf('%f',time/60)),'.tif');
imwrite(data,imname,'tif');

%Save cropped images of the 1st 4 arrays to later check for proper
%cropping of arrays
imnameA01=strcat(strcat('635cropped-A01-',sprintf('%f',time/60)),'.tif');
imwrite(datacropA01,imnameA01,'tif');
imnameA02=strcat(strcat('635cropped-A02-',sprintf('%f',time/60)),'.tif');
imwrite(datacropA02,imnameA02,'tif');
imnameA03=strcat(strcat('635cropped-A03-',sprintf('%f',time/60)),'.tif');
imwrite(datacropA03,imnameA03,'tif');
imnameA04=strcat(strcat('635cropped-A04-',sprintf('%f',time/60)),'.tif');
imwrite(datacropA04,imnameA04,'tif');

clear imname imnameA01 imnameA02 imnameA03 imnameA04

%660nm source ON
set(SerialPort,'RequestToSend','on');
pause(Holding);

trigger(CCD);
[data time] = getdata(CCD);
datacropA01 = imcrop(data,[StartHereC,StartHereR,8,7]);
datacropA02 = imcrop(data,[StartHereC+(1*8),StartHereR,8,7]);
datacropA03 = imcrop(data,[StartHereC+(8+7),StartHereR,8,7]);
datacropA04 = imcrop(data,[StartHereC+(8+7+7),StartHereR,8,7]);
datacropA05 = imcrop(data,[StartHereC+(8+7+7+8),StartHereR,8,7]);
```

```
datacropA06 = imcrop(data,[StartHereC+(8+7+7+8+8),StartHereR,8,7]);
datacropA07 = imcrop(data,[StartHereC+(8+7+7+8+7),StartHereR,8,7]);
datacropA08 = imcrop(data,[StartHereC,StartHereR+7,8,7]);
datacropA09 = imcrop(data,[StartHereC+(1*8),StartHereR+7,8,7]);
datacropA10 = imcrop(data,[StartHereC+(8+7),StartHereR+7,8,7]);
datacropA11 = imcrop(data,[StartHereC+(8+7+7),StartHereR+7,8,7]);
datacropA12 = imcrop(data,[StartHereC+(8+7+7+8),StartHereR+7,8,7]);
datacropA13 = imcrop(data,[StartHereC+(8+7+7+8+8),StartHereR+7,8,7]);
datacropA14 = imcrop(data,[StartHereC+(8+7+7+8+8+7),StartHereR+7,8,7]);
datacropA15 = imcrop(data,[StartHereC,StartHereR+7+6,8,7]);
datacropA16 = imcrop(data,[StartHereC+(1*8),StartHereR+7+6,8,7]);
datacropA17 = imcrop(data,[StartHereC+(8+7),StartHereR+7+6,8,7]);
datacropA18 = imcrop(data,[StartHereC+(8+7+7),StartHereR+7+6,8,7]);
datacropA19 = imcrop(data,[StartHereC+(8+7+7+8),StartHereR+7+6,8,7]);
datacropA20 = imcrop(data,[StartHereC+(8+7+7+8+8),StartHereR+7+6,8,7]);
datacropA21 = imcrop(data,[StartHereC+(8+7+7+8+8+7),StartHereR+7+6,8,7]);
datacropA22 = imcrop(data,[StartHereC,StartHereR+7+6+7,8,7]);
datacropA23 = imcrop(data,[StartHereC+(1*8),StartHereR+7+6+7,8,7]);
datacropA24 = imcrop(data,[StartHereC+(8+7),StartHereR+7+6+7,8,7]);
datacropA25 = imcrop(data,[StartHereC+(8+7+7),StartHereR+7+6+7,8,7]);
datacropA26 = imcrop(data,[StartHereC+(8+7+7+8),StartHereR+7+6+7,8,7]);
datacropA27 = imcrop(data,[StartHereC+(8+7+7+8+8),StartHereR+7+6+7,8,7]);
datacropA28 = imcrop(data,[StartHereC+(8+7+7+8+8+7),StartHereR+7+6+7,8,7]);

result(i,58) = time/60;
result(i,59) = max(datacropA01(:));
result(i,60) = max(datacropA02(:));
result(i,61) = max(datacropA03(:));
result(i,62) = max(datacropA04(:));
result(i,63) = max(datacropA05(:));
result(i,64) = max(datacropA06(:));
result(i,65) = max(datacropA07(:));
result(i,66) = max(datacropA08(:));
result(i,67) = max(datacropA09(:));
result(i,68) = max(datacropA10(:));
```

```
result(i,69) = max(datacropA11(:));
result(i,70) = max(datacropA12(:));
result(i,71) = max(datacropA13(:));
result(i,72) = max(datacropA14(:));
result(i,73) = max(datacropA15(:));
result(i,74) = max(datacropA16(:));
result(i,75) = max(datacropA17(:));
result(i,76) = max(datacropA18(:));
result(i,77) = max(datacropA19(:));
result(i,78) = max(datacropA20(:));
result(i,79) = max(datacropA21(:));
result(i,80) = max(datacropA22(:));
result(i,81) = max(datacropA23(:));
result(i,82) = max(datacropA24(:));
result(i,83) = max(datacropA25(:));
result(i,84) = max(datacropA26(:));
result(i,85) = max(datacropA27(:));
result(i,86) = max(datacropA28(:));
result(i,87) = mean2(datacropA01(:));
result(i,88) = mean2(datacropA02(:));
result(i,89) = mean2(datacropA03(:));
result(i,90) = mean2(datacropA04(:));
result(i,91) = mean2(datacropA05(:));
result(i,92) = mean2(datacropA06(:));
result(i,93) = mean2(datacropA07(:));
result(i,94) = mean2(datacropA08(:));
result(i,95) = mean2(datacropA09(:));
result(i,96) = mean2(datacropA10(:));
result(i,97) = mean2(datacropA11(:));
result(i,98) = mean2(datacropA12(:));
result(i,99) = mean2(datacropA13(:));
result(i,100) = mean2(datacropA14(:));
result(i,101) = mean2(datacropA15(:));
result(i,102) = mean2(datacropA16(:));
result(i,103) = mean2(datacropA17(:));
```

```
result(i,104) = mean2(datacropA18(:));
result(i,105) = mean2(datacropA19(:));
result(i,106) = mean2(datacropA20(:));
result(i,107) = mean2(datacropA21(:));
result(i,108) = mean2(datacropA22(:));
result(i,109) = mean2(datacropA23(:));
result(i,110) = mean2(datacropA24(:));
result(i,111) = mean2(datacropA25(:));
result(i,112) = mean2(datacropA26(:));
result(i,113) = mean2(datacropA27(:));
result(i,114) = mean2(datacropA28(:));

set(SerialPort,'RequestToSend','off');

imname=strcat(strcat('760image-FULL-',sprintf('%f',time/60)),'.tif');
imwrite(data,imname,'tif');

imnameA01=strcat(strcat('760cropped-A01-',sprintf('%f',time/60)),'.tif');
imwrite(datacropA01,imnameA01,'tif');
imnameA02=strcat(strcat('760cropped-A02-',sprintf('%f',time/60)),'.tif');
imwrite(datacropA02,imnameA02,'tif');
imnameA03=strcat(strcat('760cropped-A03-',sprintf('%f',time/60)),'.tif');
imwrite(datacropA03,imnameA03,'tif');
imnameA04=strcat(strcat('760cropped-A04-',sprintf('%f',time/60)),'.tif');
imwrite(datacropA04,imnameA04,'tif');

clear imname imnameA01 imnameA02 imnameA03 imnameA04


figure(1);
plot(result(:,1), result(:,Array+29), 'LineWidth',1,'Color',[0 1 0]);
%Green 565nm ave intensity
hold on;
plot(result(:,58), result(:,Array+86), 'LineWidth',1,'Color',[1 0 0]);
%Red 660nm ave intensity
```

```
hold off;
grid on;
xlabel('Time (min.)');
ylabel('Intensity (arbitrary units)');
title('Ave. Intensity vs. Time [Green: 565nm, Red: 660nm]');

end

clear R C ColumnStartSearch ColumnIndex FirstColumnArray FirstRowArray
clear time data i
fclose(SerialPort);
clear SerialPort;
stop(CCD);
clear CCD;

%Data filtering
%Data filtering is necessary to remove spikes and pits from data. This
%often occurs as a result of the temporary presence of bubbles.
FilteredResult = result;

%565nm source
for i=2:57

Average = mean2(FilteredResult(:,i)); %Finds average of all data
%in time for each array

DelMax=find(FilteredResult(:,i) > Average+Threshold/100*Average);
%Finds average intensity plus threshold percent
FilteredResult(DelMax,i) = NaN;
%and removes this data by inserting NaN in its place.
%NaN is the empty set
DelMin=find(FilteredResult(:,i) < Average-Threshold/100*Average);
%Finds average intensity minus threshold percent
FilteredResult(DelMin,i) = NaN; %and removes this data
```

```
clear DelMax
clear DelMin
clear Average
end

%660nm source
for i=59:114

Average = mean2(FilteredResult(:,i));

DelMax=find(FilteredResult(:,i) > Average+Threshold/100*Average);
FilteredResult(DelMax,i) = NaN;

DelMin=find(FilteredResult(:,i) < Average-Threshold/100*Average);
FilteredResult(DelMin,i) = NaN;

clear DelMax
clear DelMin
clear Average
end

filteredtextname = strcat(filename,'-Filtered.ft');
dlmwrite(filteredtextname,sprintf('%s\t','565nm Time (min)',
'565nm Max. Intensity A01','A02','A03','A04','A05','A06','A07',
'A08','A09','A10','A11','A12','A13','A14','A15','A16','A17','A18',
'A19','A20','A21','A22','A23','A24','A25','A26','A27','A28',
'565nm Ave. Intensity A01','A02','A03','A04','A05','A06','A07','A08',
'A09','A10','A11','A12','A13','A14','A15','A16','A17',
'A18','A19','A20','A21','A22','A23','A24','A25','A26','A27','A28',
'660nm Time (min)','660nm Max. Intensity A01','A02','A03','A04','A05',
'A06','A07','A08','A09','A10','A11','A12','A13','A14','A15','A16','A17',
'A18','A19','A20','A21','A22','A23','A24','A25','A26',
'A27','A28','660nm Ave. Intensity A01','A02','A03','A04','A05','A06',
'A07','A08','A09','A10','A11','A12','A13','A14','A15','A16','A17','A18',
'A19','A20','A21','A22','A23','A24','A25',
```

```
'A26','A27','A28'),'');
dlmwrite(filteredtextname,FilteredResult,'-append','delimiter','\t','precision',6)

clear filteredtextname


%Calculate normilzation values

First5i=(60*(Duration/3))/(2*Holding);
%converts from time to interation for the first, say 30 min.
for x=1:First5i %rows for the first 30 min. of data (if Duration = 90 min.)
First5min(x,:) = FilteredResult(x,:); %saves 1st 30 min. for all arrays to
end                                        %a new file, First5min


%Max intensity
Begin635max = First5min(:,Array+1); %selects data for array number of interest.
                                    %There is now only 1 column,
                                    %the array data column of interest
RemoveNaN = find(isnan(Begin635max(:,1)) == 1); %finds row indices where
                                                %there is a NaN entry
Begin635max(RemoveNaN,:)=[]; %removes rows with NaN in the data.

Begin760max = First5min(:,Array+58);
RemoveNaN = find(isnan(Begin760max(:,1)) == 1);
Begin760max(RemoveNaN,:)=[];

%Ave intensity
Begin635ave = First5min(:,Array+29);
RemoveNaN = find(isnan(Begin635ave(:,1)) == 1);
Begin635ave(RemoveNaN,:)=[];

Begin760ave = First5min(:,Array+86);
RemoveNaN = find(isnan(Begin760ave(:,1)) == 1);
Begin760ave(RemoveNaN,:)=[];
```

```
%Average of 1st 30 min. of intensity data
BeginningAverageValue635max = mean2(Begin635max);
BeginningAverageValue760max = mean2(Begin760max);
BeginningAverageValue635ave = mean2(Begin635ave);
BeginningAverageValue760ave = mean2(Begin760ave);


%Last30min is used only for automated calculation in intensity change. The
%following code finds the average of the last 20 minutes of data.
Last30min = FilteredResult;
Last30i = (60*(Duration-(Duration/4.5)))/(2*Holding);
for y=1:Last30i
Last30min(1,:)=[]; %converts from time to iteration
end  %this removes the first, say 70min. of data for all arrays and
     %saves the last 20min of data with the new name, Last30min.


End635max = Last30min(:,Array+1);
RemoveNaN = find(isnan(End635max(:,1)) == 1);
End635max(RemoveNaN,:)=[];

End760max = Last30min(:,Array+58);
RemoveNaN = find(isnan(End760max(:,1)) == 1);
End760max(RemoveNaN,:)=[];

End635ave = Last30min(:,Array+29);
RemoveNaN = find(isnan(End635ave(:,1)) == 1);
End635ave(RemoveNaN,:)=[];

End760ave = Last30min(:,Array+86);
RemoveNaN = find(isnan(End760ave(:,1)) == 1);
End760ave(RemoveNaN,:)=[];

SaturationAverageValue635max = mean2(End635max);
```

```
SaturationAverageValue760max = mean2(End760max);
SaturationAverageValue635ave = mean2(End635ave);
SaturationAverageValue760ave = mean2(End760ave);

%FilteredResult is the original data with NaN in place of select
%omitted data, or filtered data.  It is desirable to plot the final data
%results without the NaN in the data table since the presence of NaN
%leaves empty space
%in the plot.  Below is code to eliminate NaN entries for the
%selected arrays.

FilteredMax635time = FilteredResult(:,1);
FilteredMax635intensity = FilteredResult(:,Array+1);
FilteredMax635(:,1) = FilteredMax635time;
FilteredMax635(:,2) = FilteredMax635intensity;
RemoveNaN = find(isnan(FilteredMax635(:,2)) == 1);
FilteredMax635(RemoveNaN,:)=[];
clear FilteredMax635time FilteredMax635intensity

FilteredMax760time = FilteredResult(:,58);
FilteredMax760intensity = FilteredResult(:,Array+58);
FilteredMax760(:,1) = FilteredMax760time;
FilteredMax760(:,2) = FilteredMax760intensity;
RemoveNaN = find(isnan(FilteredMax760(:,2)) == 1);
FilteredMax760(RemoveNaN,:)=[];
clear FilteredMax760time FilteredMax760intensity

FilteredAve635time = FilteredResult(:,1);
FilteredAve635intensity = FilteredResult(:,Array+29);
FilteredAve635(:,1) = FilteredAve635time;
FilteredAve635(:,2) = FilteredAve635intensity;
RemoveNaN = find(isnan(FilteredAve635(:,2)) == 1);
FilteredAve635(RemoveNaN,:)=[];
clear FilteredAve635time FilteredAve635intensity
```

```
FilteredAve760time = FilteredResult(:,58);
FilteredAve760intensity = FilteredResult(:,Array+86);
FilteredAve760(:,1) = FilteredAve760time;
FilteredAve760(:,2) = FilteredAve760intensity;
RemoveNaN = find(isnan(FilteredAve760(:,2)) == 1);
FilteredAve760(RemoveNaN,:)=[];
clear FilteredAve760time FilteredAve760intensity RemoveNaN

if NormalizeQ == 1


figure(2);
plot(FilteredAve635(:,1), FilteredAve635(:,2)/BeginningAverageValue635ave,
'LineWidth',2,'Color',[0 1 0]); %green 565nm ave intensity
hold on;
plot(FilteredAve660(:,1), FilteredAve660(:,2)/BeginningAverageValue660ave,
'LineWidth',2,'Color',[1 0 0]); %red 660nm ave intensity
hold off;
grid on;
xlabel('Time (min.)');
ylabel('Intensity (arbitrary units)');
title('Normalized Ave Intensity vs. Time [Green: 565nm, Red: 660nm]');
else

clear x y removeNaN

Change565max = SaturationAverageValue565max - BeginningAverageValue565max;
Change660max = SaturationAverageValue660max - BeginningAverageValue660max;
Change565ave = SaturationAverageValue565ave - BeginningAverageValue565ave;
Change660ave = SaturationAverageValue660ave - BeginningAverageValue660ave;

Percent565max = Change565max * 100 / BeginningAverageValue565max;
Percent660max = Change660max * 100 / BeginningAverageValue660max;
Percent565ave = Change565ave * 100 / BeginningAverageValue565ave;
Percent660ave = Change660ave * 100 / BeginningAverageValue660ave;
```

```
fprintf('For the 565nm Ave Intensity plot, the %%intensity change was %0.2f\n',Per
fprintf('For the 660nm Ave Intensity plot, the %%intensity change was %0.2f\n',Per

%calculates standard deviation of each signal
std(result(:,Array+29))
std(result(:,Array+86))
%save average intensity of both wavelength in mat file
%for future analysis
save('averageint.mat','result(:,Array+29)','result(:,Array+86)');
```